Azimuthal Asymmetries and the Cahn Effect at COMPASS

Inga Ludwig

Fakultät für Physik
Albert-Ludwigs-Universität Freiburg

Azimuthal Asymmetries and the Cahn Effect at COMPASS

Diplomarbeit
vorgelegt
von
Inga Ludwig

Fakultät für Physik
Albert-Ludwigs-Universität
Freiburg im Breisgau

Juli 2004

Contents

List of Figures

List of Tables

Chapter 1

Introduction

One of the fundamental goals of physics is to understand the structure of matter. This implies to identify the elementary constituents of which matter is built and to investigate their properties and ways of interaction. The matter that surrounds us in everyday life is entirely made up of protons, neutrons and electrons. While the latter is considered as an elementary particle which up to now revealed no internal sub-structure, the two nucleons are known to be compound objects since the late fifties [HM55, Hof57]. The *partons*, as the constituents of the nucleon were historically called, were identified to be three fermionic *valence quarks* which are bound by exchanged bosons called *gluons*. These bosons can split up into virtual quark anti-quark pairs which are known as *sea quarks*.

Since the late fifties *deep inelastic scattering (DIS)* reactions in which structure-less leptons are scattered off nucleons, are exploited to access the internal structure of the nucleon. Great progress in understanding the dynamics of the partons has been made. In contrast, only little is known about the spin properties of the nucleon. One of the most up-to-date topics in DIS is the measurement of the contribution of the gluons to the nucleon spin, which is composed according to the *helicity sum rule* [JM90]

$$\frac{1}{2} = \frac{s_N}{\hbar} = \frac{1}{2}\Delta\Sigma + \Delta G + L_q + L_g \tag{1.1}$$

from contributions of the spins of the quarks ($\Delta\Sigma$) and gluons (ΔG) and their orbital angular momenta L_q and L_g. Measurements at the HERMES experiment have revealed the value of $\Delta\Sigma$ to be $0.30 \pm 0.04 \pm 0.09$ [Ack99]. Up to now it is not clear whether it is possible to access the contributions from the angular momenta. The determination of the gluon contribution will be possible from studies of *photon gluon fusion* events. ΔG will be extracted from cross section asymmetries of these events, in which a virtual photon interacts with one of the gluons in the nucleon via the creation of a quark pair.

One of the most recent experiments for the study of DIS is the COMPASS[1] [Bau96] experiment at CERN[2]. In the COMPASS muon programme a polarised 160 GeV/c muon

[1]**CO**mmon **M**uon and **P**roton **A**pparatus for **S**tructure and **S**pectroscopy
[2]**C**onseil **E**uropèen pour la **R**echerche **N**ucléaire

beam is scattered off a polarised fixed ^{6}LiD target. The products of the scattering reaction are recorded using a two stage spectrometer, which allows to measure a wide momentum range and provides a high momentum resolution. A short description of the design of the spectrometer will be given in Chapter 2 of this thesis. With this experimental setup COMPASS will be able to make contributions to the investigation of numerous topics of interest in DIS. Among these the main goals of the muon programme are:

- Determination of ΔG through open charm and high-p_T hadron pairs.
- Precision measurements and flavour decomposition of the *longitudinal helicity distribution functions*.
- Investigation of *transverse spin distribution functions*.

In addition to the muon programme, measurements with a hadron beam are planned.

Except for the transversity measurement, the goals of the muon programme aim at investigating the longitudinal spin properties of the quarks and gluons. For a complete description of the structure of the nucleon also the transverse degrees of freedom play an important role. Up to now the transverse spin properties, but also unpolarised aspects of these transverse degrees of freedom, are poorly understood. One of the latter is the subject of this diploma thesis: Azimuthal asymmetries in the hadron production in *semi-inclusive DIS (SIDIS)*, which are caused by the intrinsic transverse momentum k_T that is carried by the quarks the nucleon consists of (*Cahn asymmetry*). This quantity is an important input parameter for models describing the intrinsic motion of the quarks and the relativistic nature of the nucleon. A profound understanding of nucleon dynamics is essential for the interpretation of any spin-dependent measurement. For example the extraction of the gluon polarisation ΔG from high-p_T spin asymmetries requires corrections for the contributions of background processes. These have to be estimated from Monte Carlo studies which are based on a good knowledge of the nuclear structure and nuclear interactions. Furthermore the knowledge of the Cahn effect may help to disentangle the product of transversity and Collins fragmentation function from the transverse target spin asymmetries. Chapter 3 will be dedicated to the theoretical concepts of deep inelastic scattering with the main focus of course being the Cahn effect and other processes which influence the azimuthal angular distributions of the hadrons produced in SIDIS.

Measurements of the Cahn effect in a comparable kinematic region have been performed before by EMC at CERN who published their results in 1983 and 1987 [Aub83, Arn87] as well as by E665 at Fermilab in 1993 [Ada93]. However, COMPASS can revert to a much larger data sample than these experiments and therefore has the opportunity to measure the asymmetry and its dependence on the event kinematics with much higher precision.

The main part of this thesis is dedicated to the the analysis of the azimuthal angular distributions of the hadrons produced in SIDIS, which is described in Chapter 4. This section also contains the obtained results. These are discussed in Chapter 5 and compared to the results of the mentioned previous measurements and to the theoretical predictions.

Chapter 2

The COMPASS Experiment

In order to cover all the requirements of the wide COMPASS physics programme, a multifunctional and flexible detector setup is needed. In this chapter only a brief overview on the design (see Fig. 2.1) of the individual sub-systems (shaded differently in the sketch) will be given. For more detailed descriptions of the COMPASS detector the reader is referred to [Bau96, Grü02, Hod02, Sch02] or the additional references given therein. Since the data analysed in this thesis have been taken during the 2002 run, this description corresponds to the setup which existed then.

2.1 Beam and Target

The Muon Beam

The muon beam is produced in two steps (see Figure 2.2). The SPS (the CERN **S**uper **P**roton **S**ynchroton) provides a proton beam which is focused on a beryllium target. Thus a beam of hadrons is produced which mainly consists of protons, but contains also a fraction of pions and a few kaons. The latter two decay with a short mean lifetime mainly into the desired muons. These are separated from the remaining hadrons by an absorber. Afterwards an arrangement of bending magnets and scrapers serves to select the desired 160 GeV/c muons. The momentum of the beam particles is measured in the *beam momentum station (BMS)*, a set of scintillating fibre detectors which exploits the bending of the beam through the bending magnets.

The SPS is operated in 16.8 s cycles. Hence the particles are extracted from the accelerator in so-called *spills* of 5.1 s. In the remaining 11.7 s there is no beam. The intensity of the beam is about $2 \cdot 10^8$ particles per spill in normal operation mode.

The muons from pion decay are naturally polarised because of the parity violation in this decay. The degree of polarisation which is gained this way depends on the ratio of the momenta of the decaying pion and the produced muon and is -0.76 on average[1]. At COMPASS the spin is preferentially anti-aligned with the muon momentum [Dob94].

[1] In 2004 the beam setup has been optimised, thus the average beam polarisation will be enhanced.

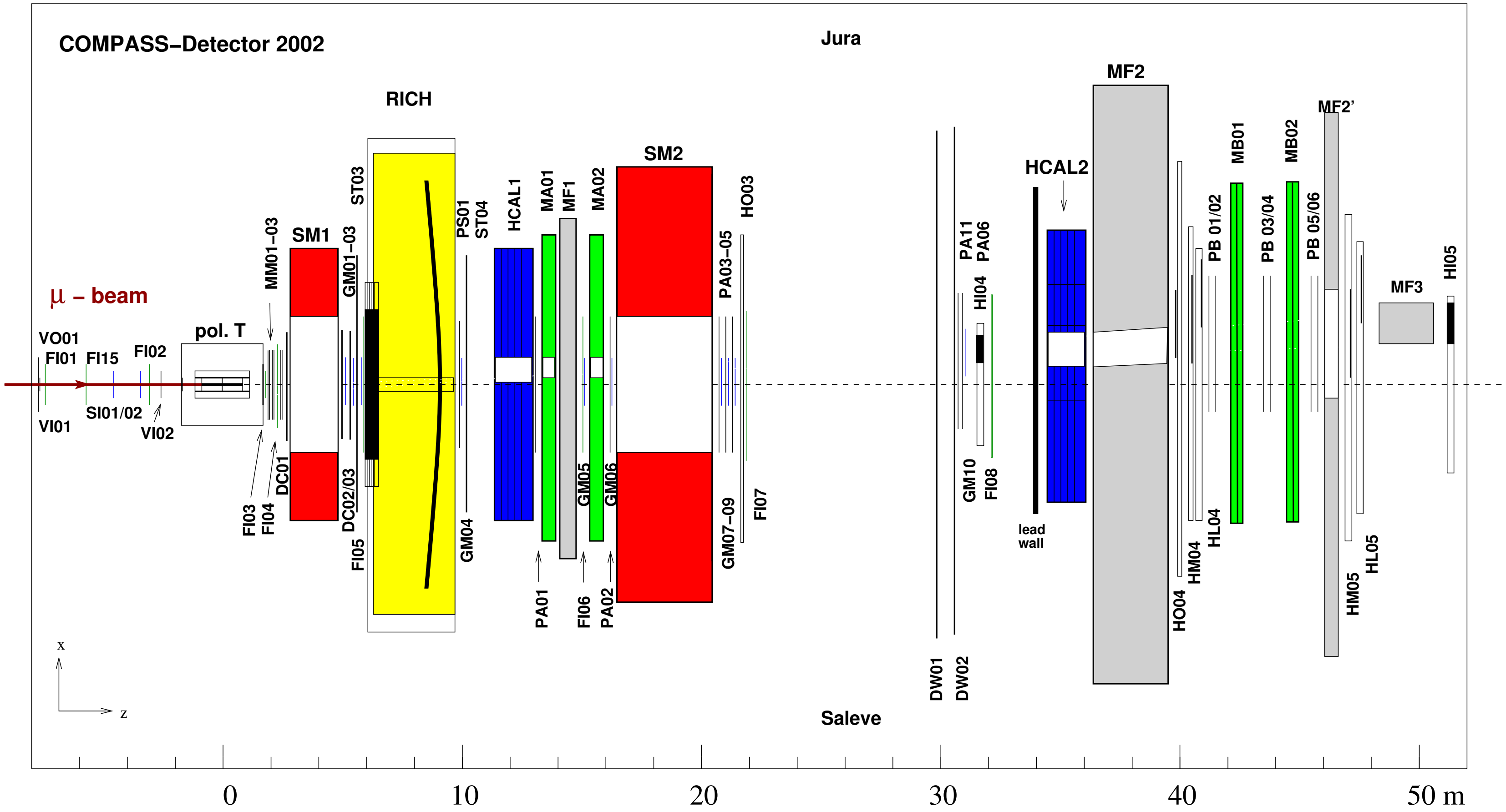

Figure 2.1: Setup of COMPASS in 2002 [Grü02]. The beam enters the setup from the left hand side. In the most upstream part of the apparatus the COMPASS target is shown. The reaction products are detected in one of the two spectrometer stages. The tracking of particles with low momenta is performed in the first stage while in the second stage the particles with higher momenta are tracked. To provide the bend of the tracks which is necessary for the momentum measurement, both stages are equipped with spectrometer magnets (SM1 and SM2).
The tracking system consists of silicons (SI), scintillating fibres (FI), Gems and MicroMeGas (GM, MM) as well as of MWPCs (PS, PA and PB), straw detectors (ST) and drift chambers (DC, W4-5). Muon identification is provided by a setup of absorbers (MF) and Iarocci detectors (MA) or drift tubes (MB). The COMPASS trigger system consists of trigger hodoscopes (HI, HL, HM and HO) and veto hodoscopes (VI and VO) in front of the target. The setup is completed by a RICH detector in the first stage and the two hadronic calorimeters HCAL1 and HCAL2.

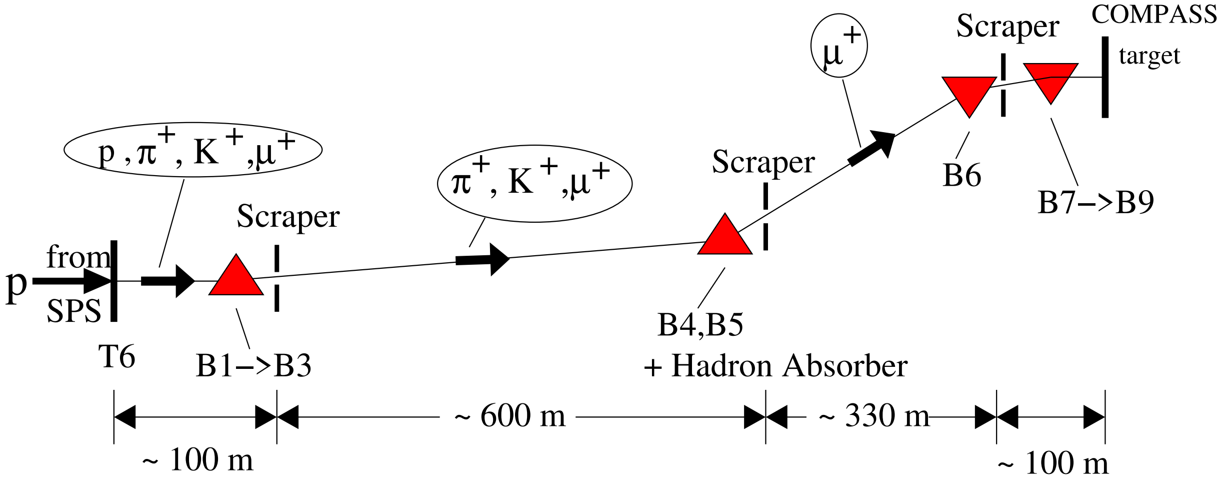

Figure 2.2: The COMPASS beam line [Hod02]. T6 denotes the hadron production target, while B1 to B9 are the bending dipoles.

The Polarised Target

In order to gain high luminosity COMPASS is operated with a solid state target during the runs of the muon programme. Presently the target magnet of the SMC (the **S**pin **M**uon **C**ollaboration) experiment, which was the predecessor of COMPASS, is used [Ada99]. The schematic view of the target setup is shown in Fig. 2.3. To gain a high target polarisation and to conserve it over long periods in time a dilution refrigerator, using a mixture of liquid ^{3}He and ^{4}He as cooling medium, cools down the target material to temperatures of about 50 mK. The polarisation of the target nucleons is achieved by means of *dynamic nuclear polarisation*. The necessary longitudinal magnetic field of about 2.5 T is provided by a superconductive solenoid. Additionally, a dipole field can be superimposed which serves to rotate the target spins and also to hold a transverse polarisation for the transversity data taking.

Up to now the target is filled with solid ^{6}LiD which serves as a deuterium target with relatively high polarisability[2]. The ^{6}LiD can be considered as a system of a ^{4}He nucleus and two deuterons. While the spins of the constituents of the He nucleus add up to zero, the two deuterons have a non vanishing spin and therefore can align their spins in an external magnetic field. Polarisations of about 50% are achieved. The solid target material is placed in two cylindrical cells of 60 cm length and 1.5 cm radius which are mounted in the solenoid in a row along the beam line, with a gap of 10 cm in between. The spins of the nucleons in the two cells are oriented anti-aligned (Fig. 2.4). Thus data samples with both polarisation directions for asymmetry calculations can be recorded at the same time and hence at equal muon fluxes. In this configuration, however, the geometrical acceptance for the downstream cell is higher than for the upstream cell. In order to minimise false

[2]For measurements with a polarised proton target, a NH_3 filling will be used in the future.

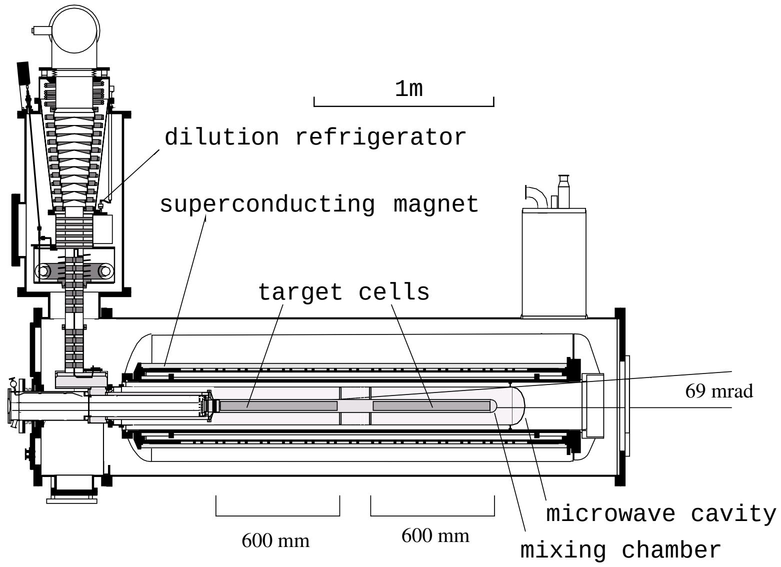

Figure 2.3: The SMC target used at COMPASS.

asymmetries[3] due to acceptance effects, the orientation of the target spins is reversed about every eight hours.

2.2 Spectrometer

The diverse physics programme of COMPASS requires a spectrometer which covers a large acceptance and provides high resolution in the measurement of momenta spread over a wide range. Thus the spectrometer consists of two stages. The first stage, called the *large angle spectrometer (LAS)*, is equipped with the magnet SM1 which has a bending power of about 1 Tm. Low momentum tracks starting from about $1\,\mathrm{GeV}/c$ are reconstructed in this stage. The *small angle spectrometer (SAS)* covers the higher momenta up to $200\,\mathrm{GeV}/c$, thanks to the 4.4 Tm bending power of the magnet SM2. Each spectrometer magnet is surrounded by a setup of tracking detectors and dedicated detectors for the energy measurement and particle identification (PID).

2.2.1 Tracking

Each of the spectrometer stages is equipped with a set of tracking detectors for the momentum measurement. In order to ensure unambiguous track reconstruction with good spatial resolution, most of these detectors are designed as modules consisting of multiple layers with strips or wires inclined with respect to each other. In the beam region the

[3]Target spin asymmetry measurements at COMPASS in principle always mean to calculate an asymmetry A according to $A = \frac{N^u - N^d}{N^u + N^d}$ from the count rates N^u and N^d of events with vertex in upstream and downstream cell.

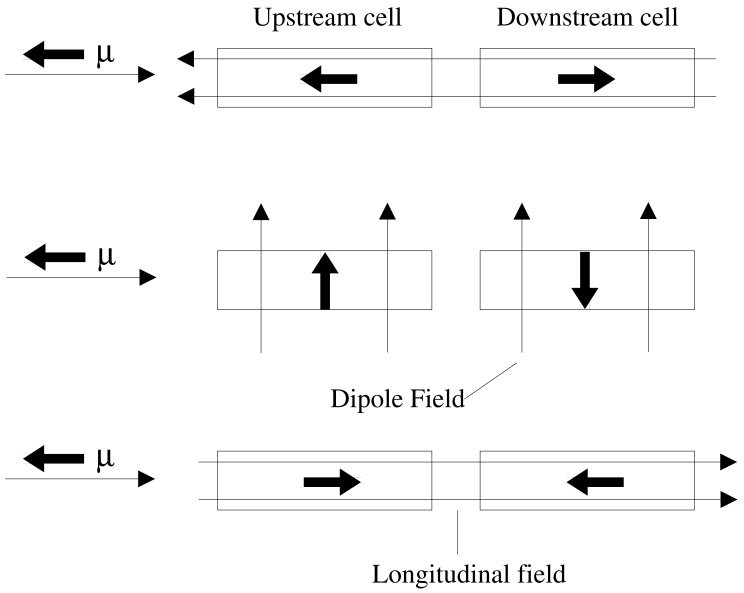

Figure 2.4: Spin configuration and orientation of the magnetic field of the two target cells. The top and bottom figures show the configuration during a measurement with longitudinally polarised target before and after a field rotation. In between the situation during the field rotation and the transversity measurement is sketched. In the present configuration of primary and secondary beam, the spin of the beam muon is always anti-aligned to its momentum. The longitudinal configuration in the upper row is referred to as the *outward configuration* compared to the *inward configuration* shown in the lower row.

track density is high, therefore fast detector types are operated here which are capable of tolerating high particles fluxes and have a high time resolution. At COMPASS silicon detectors and scintillating fibres are used for the beam tracking. Gas detectors with excellent resolution like GEMs (**G**as **E**lectron **M**ultipliers) and MicroMeGas (**Micro Me**sh **Ga**s detectors) are used to detect the reaction products passing the intermediate areas close to the beam region. Coverage of the remaining large area is provided by MWPCs (**M**ulti **W**ire **P**roportional **C**hambers), straw detectors and drift chambers. Except for the beam trackers, the detectors are designed with a hole or dead zones in the central region in order to avoid the overflow of signals from the the region with a high particle flux around the beam.

2.2.2 Particle ID

The COMPASS particle identification is designed for two main purposes, the discrimination between charged hadron types and the identification of the scattered muons.

Calorimetry

The hadron energy is measured in the hadronic calorimeters (HCAL1 and HCAL2). The energy information is important for the discrimination between hadrons from the scattered muons. Since a hadron loses much more energy in matter than the muons do, a large fraction of the hadrons gets absorbed in the calorimeters, while the muons pass the calorimeters losing only a small fraction of their energy. The COMPASS calorimeters are built in a sandwich structure of iron and plastic scintillator layers. A cellular design allows to determine the position of the centre of energy deposits stemming from a certain particle and therefore to attribute the deposit to the reconstructed tracks. In 2002 a layer of lead, installed in front of HCAL2, served to absorb electrons and photons. The calorimeters are designed with holes in the centre of the acceptance. The beam muons, and in case of HCAL1 also the high energetic decay products which are to be reconstructed in the SAS, thus pass the calorimeters.

RICH

For the discrimination of charged hadron types a large RICH (**R**ing **I**maging **Č**erenkov detector) is installed in the first spectrometer stage. It is able to identify charged pions, kaons and protons above a threshold of $3\,\mathrm{GeV}/c$ (for pions) and up to $45\,\mathrm{GeV}/c$. The Čerenkov photons produced in a C_4F_{10} gas filling are focused by spherical mirrors of 6.6 m radius of curvature onto MWPCs equipped with CsI photo cathodes.

Muon Identification

The muon identification exploits the fact that muons, unlike the hadronic products of the reaction, do not produce hadronic showers since they do not obey the strong interaction. This means that they penetrate thick layers of material without being absorbed. On the contrary, the majority of the hadrons are absorbed in the hadronic calorimeters. To also remove the remaining ones, thick walls of concrete or iron, the so called *muon filters*, are placed behind the calorimeters. Particles which pass these filters are detected in both parts of the *muon walls*, which are realised as drift tube or Iarocci detectors installed directly in front and behind the muon filters.

2.3 The Trigger System

COMPASS is operated with high beam intensity and a high density target. Therefore the rates of events are high and it is necessary to pre-select events which are candidates for the desired event type already on the hardware level. This is the task of the trigger system [Leb02].

For most of the analyses of the muon programme the detection of the scattered muon is necessary. Therefore dedicated hodoscopes are installed mainly behind the muon filters. These consist of scintillator paddles which are read out by photomultipliers. These detectors are grouped to the so-called *inner*, *ladder*, *middle* and *outer trigger*. The muons detected in these four trigger detectors correspond to different ranges of the energy they lost in the scattering process. These ranges are determined by the angle under which the muon gets deflected in the field of the spectrometer magnets. The information from the hadron calorimeters is used to select events with hadron candidates. Veto hodoscopes are placed in front of the target to make sure that a scattered muon candidate is not a muon from the beam halo. The information from all these detectors is combined in order to generate different trigger signals, which decide whether the information from a given event is read out or not. Typically, trigger rates of about $2 \cdot 10^4$ interesting events per spill[4] were recorded.

2.4 DAQ

To deal with the high trigger rates, a fast and flexible data acquisition system (DAQ) was developed for COMPASS [Fis02]. The principle of this system is sketched in Figure 2.5. The detector signals are digitised on *front-end cards* directly attached to the detectors. If there is a trigger signal, the information is transferred to a CATCH (**C**OMPASS **A**ccumulate, **T**ransfer and **C**ontrol **H**ardware) or GeSiCa (**GE**M **Si**licon **Ca**rd) module, where it is converted into a standard format. The CATCHes also provide the front-end cards with the trigger signals. These signals are distributed to the CATCHes by the *trigger control system*. Optical fibres transfer the data from the CATCH to a set of *read out buffer* PCs, where they are stored until the information belonging to the same event is combined in the *event builders*. The *raw data*, which is the output of this procedure, is temporary written to disk and then transferred to tape using the CERN central data recording system.

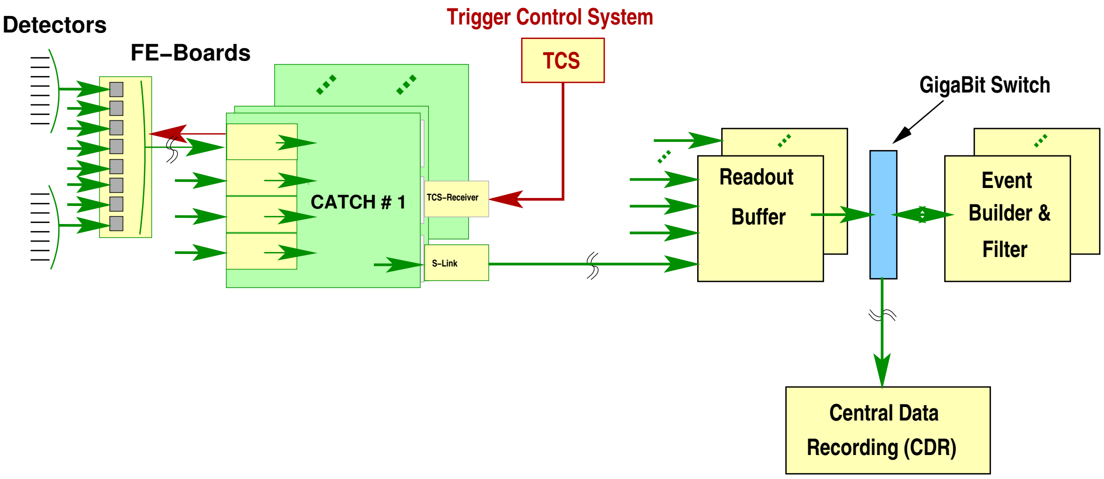

Figure 2.5: Data acquisition at COMPASS: The read-out driver CATCH is the link between the front-end electronics and the real data acquisition as well as the front-end and the trigger control system.

[4]Even higher trigger rates are achieved in the 2003 and 2004 runs.

2.5 Analysis Software

The analysis of the acquired data is performed in several steps. Software tools, which are mainly based on C++ and ROOT[5] [BR], have been developed for the processing of the COMPASS data.

The raw data is prepared for the analysis by a software called *CORAL* (**CO**mpass **R**econstruction and **A**na**L**ysis) [Gob]. On this level track reconstruction and vertexing as well as the analysis of the information from the calorimeters and the RICH are performed. The output of CORAL are *DST* files (**D**ata **S**ummary **T**apes) which can be read again by CORAL for further analysis. In addition, events which contain at least one vertex are stored in *mDST* (**m**ini **DST**) format. These mDST are the basis of the individual analyses. A software environment called PHAST (**PH**ysics **A**nalysis **S**oftware **T**ools) [Ger] has been developed especially for the requirements of COMPASS analyses. The results of this thesis are obtained processing mDST data with the PHAST version 6.009 [Ger04].

For many analyses *Monte Carlo simulations* are essential. Artificial events are produced randomly by so-called *event generators* like *LEPTO* or *PYTHIA* [Sjo03, IER97]. These simulations are based on probability densities known from cross sections which are calculated theoretically or are measured in previous experiments. The interaction of the produced particles in the detector material is also simulated, using a software called *COMGEANT*[6] [Ale]. The output has nearly the same format as the real raw data and can be processed by CORAL and PHAST analogously.

[5] A C++ based framework for analysis of high energy physics data provided by CERN.
[6] The **COM**PASS Monte Carlo simulation programme based on the **Geant** version 3.21.

Chapter 3

Theory

The aim of this chapter is to give a short introduction to the concepts which are necessary for the analysis performed in this thesis. Section 3.1 deals with unpolarised deep inelastic scattering and the corresponding cross sections, structure functions and parton distribution functions. The dependence of the cross section on the azimuthal angle is covered in Section 3.2. This is the theoretical basis of the analysis performed in this thesis. Unless pointed out otherwise, this chapter is based on Refs. [Vet98, Hag02, Rit02].

3.1 Deep Inelastic Scattering

In deep-inelastic lepton-nucleon scattering

$$l + N \rightarrow l' + X \tag{3.1}$$

a lepton l scatters off a nucleon N, which fragments into some hadronic final state X. In the case of COMPASS the lepton is a positively charged muon. The nucleon may be a proton as well as a neutron, since a deuterium target is used. The Feynman graph of such a process is sketched in Figure 3.1.

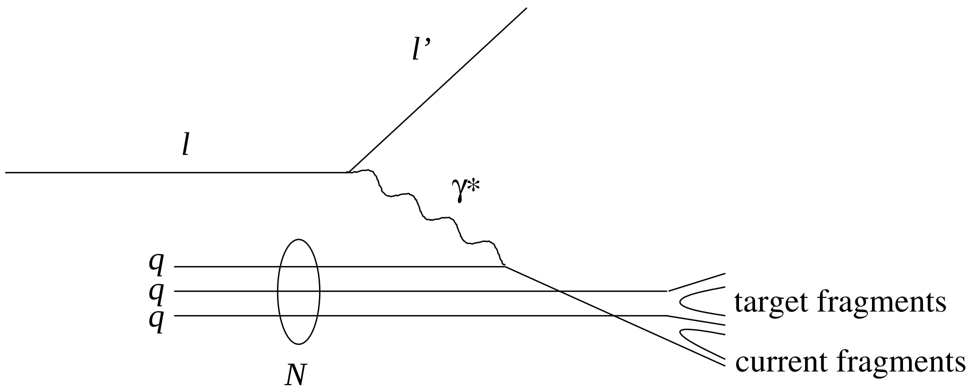

Figure 3.1: Schematic representation of the DIS process.

The lepton-nucleon interaction is mediated by a virtual photon γ^*. In principle the exchange particle could also be a Z^0 boson, but since COMPASS is operated at momentum transfers far below the mass of the Z^0, its contribution is negligible against the γ^* exchange.

If the momentum transfer to the virtual photon and the invariant mass of the final state are large compared to the nucleon mass, one speaks of *deep inelastic scattering (DIS)*. In this limit the partons do not interact among themselves on the time scale of the scattering reaction. DIS can therefore be described as an incoherent sum of scattering processes off free quarks. The corresponding lowest order Feynman graph is sketched in Fig. 3.2. The struck quark cannot be observed itself. Due to quark confinement it fragments immediately into one or more hadrons which, together with the remnants of the target, make up the final state X. If a final state hadron contains quarks from the target remnant, one speaks of a particle from *target fragmentation* . If not, this hadrons is attributed to the *current fragmentation.*

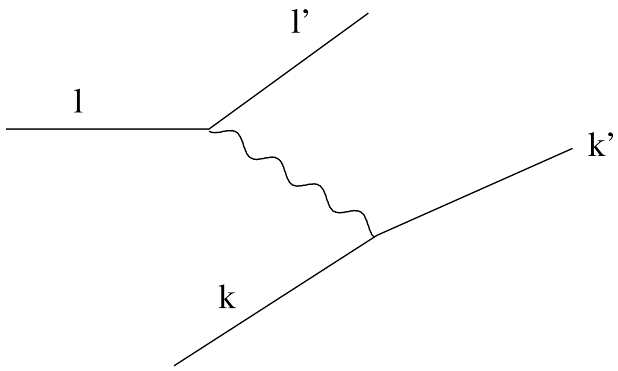

Figure 3.2: Feynman graph of the elementary lepton-quark scattering

Depending on which outgoing particles are detected in the final state one distinguishes *inclusive*, *semi-inclusive* and *exclusive* DIS process. In inclusive processes only the scattered lepton is detected (see Sec. 3.1.1). If in addition one or more hadrons are observed, the process is called semi-inclusive (Sec. 3.1.2). Exclusive processes are processes in which X is completely detected.

3.1.1 Inclusive Scattering Processes

Scattering processes can conveniently be described using a set of appropriate *kinematic variables*. Most of them are defined as scalar products of four-momenta and accordingly are Lorentz invariant. For the notation of four-momenta of the involved particles as used in this thesis see Table 3.1. The most frequently used variables are:

- The fractional energy transfer to the virtual photon is defined as

$$y := \frac{\mathbf{P} \cdot \mathbf{q}}{\mathbf{P} \cdot \mathbf{l}} \,. \tag{3.2}$$

  In the lab frame of a fixed target experiment this expression simplifies to $y = \frac{\nu}{E}$.

particle	**four-momentum**
incoming lepton	$\mathbf{l} = (E, \vec{l})$
scattered lepton	$\mathbf{l}' = (E', \vec{l}')$
nucleon	$\mathbf{P}$
virtual photon	$\mathbf{q} = \mathbf{l} - \mathbf{l}' = (\nu, \vec{q})$
initial quark	$\mathbf{k}$
final quark	$\mathbf{k}'$
final state hadron	$\mathbf{p} = (E_h, \vec{p})$

Table 3.1: Notation of the four-momenta of the particles involved in the scattering process as used in this thesis. If the four-momenta are not decomposed into energy and three momentum like it is shown in the table, the components of a four-momentum $\mathbf{m}$ are denoted m^μ.

- The invariant mass $\mathbf{q}^2$ of the virtual photon is always negative. Therefore one defines the negative squared momentum transfer $Q^2 := -\mathbf{q}^2$ which takes only positive values.

- The *Bjørken scaling variable* x is defined as

$$x := \frac{Q^2}{2\,\mathbf{P} \cdot \mathbf{q}} \,. \tag{3.3}$$

  If the scattering takes place off the free nucleon, it can take values in the range $[0, 1]$. In the lab frame and for a fixed target experiment, x is equal to the expression $x = Q^2/(2M\nu)$. In the *infinite momentum frame*[1] where the transverse momentum of the quarks in the nucleon is negligible, x is the fraction of nucleon momentum that is carried by the considered quark. In every other reference frame this interpretation holds only for the longitudinal momentum component. In scattering processes which do not resolve the sub-structure of the nucleon, x takes the value 1. This means that the nucleon effectively interacts like a point-like particle. Correspondingly, small values of x (at large Q^2) indicate deep inelastic scattering events in which the nucleon momentum is shared by many partons.

- The invariant mass of the hadronic final state $W^2 := (\mathbf{P} + \mathbf{q})^2$.

In terms of these kinematic variables the conditions under which one speaks of deep inelastic scattering are $Q^2 \gg M^2$ and $W^2 \gg M^2$. This is equivalent to the frequently used description of the *deep inelastic limit*:

$$\nu,\ Q^2 \to \infty \qquad \text{while } x \text{ fixed} \tag{3.4}$$

[1]The infinite momentum frame is a reference frame in which the nucleon has infinite velocity compared to the lepton.

Cross section

The cross section for an inclusive scattering process can be expressed as the product of a leptonic part which is described by the *leptonic tensor* $L^{\mu\nu}$ and a hadronic part described by the *hadronic tensor* $W^{\mu\nu}$. Therefore the cross section for this kind of process[2] can be written as

$$\frac{d^2\sigma}{dxdy} = 2\pi\alpha^2 \frac{y}{Q^4} L_{\mu\nu} W^{\mu\nu} . \tag{3.5}$$

$L_{\mu\nu}$ describes the coupling of the virtual photon to the point-like lepton and therefore is a well known quantity which can be calculated [Man92]:

$$L^{\mu\nu} = 2[l^\mu l'^\nu + l^\nu l'^\mu - g^{\mu\nu} \mathbf{l} \cdot \mathbf{l}'] , \tag{3.6}$$

where $g^{\mu\nu}$ denotes the Minkowski metric. $W^{\mu\nu}$ on the other hand describes the coupling of the photon to the nucleon and hence the interaction with a particle which has an internal structure. Since this structure is unknown, $W^{\mu\nu}$ cannot be specified. However, symmetry considerations reveal that only two of the 16 components of $W^{\mu\nu}$ are independent and the spin averaged hadronic tensor can be expressed in terms of two *structure functions* $F_1(x, Q^2)$ and $F_2(x, Q^2)$ which contain all the information about the nucleon structure (see e.g. [Gri87] for a more extended derivation):

$$W^{\mu\nu} = -\left(g^{\mu\nu} + \frac{q^\mu q^\nu}{Q^2}\right) F_1(x, Q^2) + \frac{1}{\mathbf{P}\cdot\mathbf{q}} \left(P^\mu + \frac{\mathbf{P}\cdot\mathbf{q}}{Q^2} q^\mu\right) \left(P^\nu + \frac{\mathbf{P}\cdot\mathbf{q}}{Q^2} q^\nu\right) F_2(x, Q^2) . \tag{3.7}$$

Scaling behaviour

In the deep inelastic limit, when the scattering can be assumed to be elastic scattering off one of the partons, the dependence of the structure functions on Q^2 vanishes and the two functions become dependent on each other. This behaviour is known as *Bjørken scaling*:

$$F_i(x, Q^2) \overset{(\nu, Q^2 \to \infty)}{\longrightarrow} F_i(x) \qquad \text{with} \qquad F_2(x) \approx 2x\, F_1(x) . \tag{3.8}$$

The latter equation is known as *Callan-Gross relation*. Scaling has been observed in various measurements of $F_2(x, Q^2)$ (see Fig. 3.3). F_2 as a function of Q^2 becomes flat, for values of x approaching about 0.2.

The functions $F_1(x)$ and $F_2(x)$ become easily interpretable if the process is described in terms of the *quark parton model (QPM)*. In this picture the nucleon is treated as a flow of collinearly moving point-like partons which do not interact with each other. This description is suitable as long as Q^2 is large enough to resolve the bare partons in the nucleon. The structure functions can then be represented as the sum of so called *parton distribution functions* q_i:

$$F_1(x) = \frac{1}{2} \sum_i e_i^2 q_i(x) . \tag{3.9}$$

The densities $q_i(x)$ give the probabilities for finding a quark or anti-quark of flavour i which carries the momentum fraction x.

[2] In the following the lepton mass is always neglected as it is done in [Cah78].

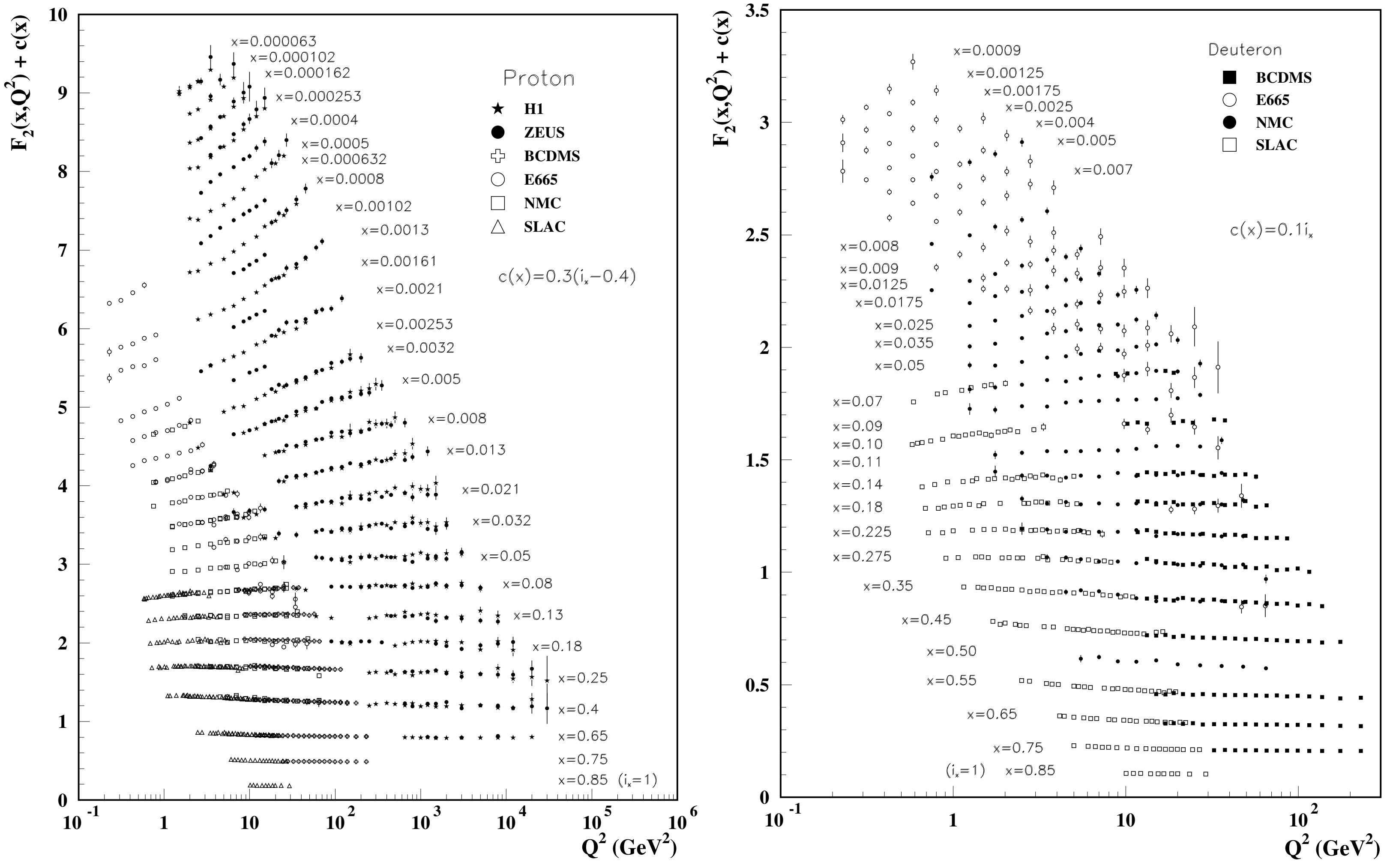

(a) (b)

Figure 3.3: $F_2(Q^2)$ at different values of x [Hag02]. For a better view different constants, depending on x, are added to the data points. In (a) the data from various proton-target or collider experiments are shown, while (b) combines data from measurements with deuteron targets.

Scaling Violation

Figure 3.3 reveals that there are regions at low x, where the scaling behaviour is violated. Here the cross section shows a considerable Q^2-dependence. This is due to the influence of the sea quarks and gluons, which are resolved in this kinematic range. The more partons are observed in the nucleon the lower is the average x per parton. Hence with increasing resolution the probability to find a parton which carries high x drops. Accordingly, the parton distribution functions take larger values at small x and lower values at high x, compared to the behaviour in the regime of Bjørken scaling.

The resulting Q^2-dependence of the structure functions can be derived in operator product expansions, in which the order of a contribution is indicated by its *twist*. The lowest order is twist-2. The twist is correlated to the Q^2 dependence, as an operator of twist n dies off as $1/Q^{n-2}$ at high Q^2 [Hag02].

3.1.2 Semi-Inclusive Scattering Processes

If in addition to the scattered lepton at least one hadron h is observed in the final state the process is called *semi-inclusive (SIDIS)*.

$$l + N \to l' + h + X \tag{3.10}$$

To describe this kind of process additional kinematic variables are necessary (*semi-inclusive kinematic variables*) which introduce the properties of the hadron:

- The fractional energy transfer z from the γ^* to the hadron is defined as the Lorentz scalar
$$z := \frac{\mathbf{P} \cdot \mathbf{p}}{\mathbf{P} \cdot \mathbf{q}}. \tag{3.11}$$
In the lab frame of a fixed target experiment this simplifies to $z = E_h/\nu$, where one can easily see the interpretation as fraction of the energy of the γ^*.

- The *Feynman scaling variable* x_F is not Lorentz invariant. It is defined in the $\gamma^* N$ centre-of-mass system and gives the longitudinal fraction of momentum of the hadron with respect to the momentum of the γ^*
$$x_F := \frac{p_{\|}}{|\vec{q}|}. \tag{3.12}$$
x_F can be approximated by $x_F \approx 2p_{\|}/W$. The variable x_F can serve to distinguish hadrons from target- and current fragmentation. The former are preferentially emitted backwards in the $\gamma^* N$ centre-of-mass frame and therefore have high probability to be produced with negative x_F. The current fragments on the contrary carry positive values.

- The transverse momentum p_T of the hadron with respect to the direction of the virtual photon.

Fragmentation Functions

In SIDIS processes structure functions do no longer suffice to describe the whole scattering process. Another class of functions, the *fragmentation functions* $D_i^h(z)$ must be introduced. While the structure functions, together with the partonic cross section, describe the scattering of the lepton off the parton, the fragmentation functions describe the subsequent hadronisation of the struck parton. $D_i^h(z)$ is the probability density that the fragmentation of a parton of type i produces a hadron of type h which carries the fractional energy z. Therefore the type of the detected hadron can be used to identify the flavour of the quark which absorbed the virtual photon ("*flavour tagging*"). Semi-inclusive measurements therefore reveal additional information on the partonic structure of the nucleon.

Assuming *factorisation*[3] the leading twist cross section for the production of a hadron of type h can be expressed as [CES92]

$$\begin{aligned}\frac{d^5\sigma^h}{dx\,dy\,dz\,dp_T\,d\phi} &= \sum_{i,j} F_i(\xi,Q^2)\frac{d^5\sigma_{ij}}{dx_p\,dy\,dz_p\,dk_T\,d\phi}D_j^h(\zeta) \\ &\quad dx_p\,dz_p\,d\xi\,d\zeta\,\delta(x-\xi x_p)\delta(z-\zeta z_p)\frac{p_T}{k_T}\delta^2(p_T-\zeta k_T) \qquad (3.13)\end{aligned}$$

with x_p and z_p being the partonic equivalents of the variables x and z, which are defined like these quantities but with the four-momenta of the involved hadrons being replaced by those of the incoming and outgoing partons. $d\sigma_{ij}/dx_p dy dz_p$ gives the cross section of the scattering process on the parton level. The sum runs over all types of incoming (i) and outgoing (j) partons, including the gluons. Neglecting QCD contributions to the partonic cross section, integrating over p_T and expressing the $F_i(\xi,Q^2)$ in terms of the parton model, one obtains the simplified expression

$$\frac{d^3\sigma^h}{dx\,dy\,dz} \propto \sum_i e_i^2 q_i(x) D_i^h(z)\,. \qquad (3.14)$$

The distribution functions $q_i(x)$ cannot be accessed by perturbative methods, since the hadronisation takes place on distant scales. Instead phenomenological models are necessary to parametrise them (e.g. the LUND model [And83]).

Because of the variety of possible combinations of i and h there are numerous fragmentation functions. However isospin symmetry and charge conjugation invariance reveal some of them to be equal. In the simple case of just three quark flavours (u, d, s) and two charged final state hadrons (π^+, π^-) twelve structure functions can be reduced to three functions D_1, D_2 and D_3, since

$$D_1 := D_u^{\pi^+} = D_{\bar{d}}^{\pi^+} = D_d^{\pi^-} = D_{\bar{u}}^{\pi^-} \qquad (3.15)$$

$$D_2 := D_d^{\pi^+} = D_{\bar{u}}^{\pi^+} = D_u^{\pi^-} = D_{\bar{d}}^{\pi^-} \qquad (3.16)$$

$$D_3 := D_s^{\pi^+} = D_{\bar{s}}^{\pi^+} = D_s^{\pi^-} = D_{\bar{s}}^{\pi^-}\,. \qquad (3.17)$$

[3]Which means that the two mentioned sub-processes can actually be treated separately. Factorisation, which has theoretically [CSS85] been proven and is also supported by experiments [BKK95], disfavours a possible dependence $D_i^h(z,Q^2)$ on the inclusive variable Q^2.

The so-called *favoured* fragmentation function D_1 describes processes in which the struck quark enters the final state hadron as a valence quark. This is more likely than the indirect processes which the *unfavoured* D_2 refers to, therefore D_2 is smaller than D_1. The order of magnitude of D_3 is comparable to that of D_2 since the underlying processes are similar [Vet98].

3.2 Azimuthal Asymmetries

Up to now the direction into which the final state particles are scattered was not considered in the cross sections. But actually, the unpolarised SIDIS cross section reveals a non-trivial modulation in the hadron azimuthal angle ϕ. This angle is defined as the angle between the lepton scattering and the production plane of the observed hadron (c.f. Figure 3.4). The virtual photon momentum defines the positive z direction[4]. With $\vec{l}$, $\vec{q}$ and $\vec{p}$ being the three-momenta of the incident muon, virtual photon and outgoing hadron, $\cos\phi$ is given by

$$\cos\phi = \frac{\vec{l}\times\vec{q}}{|\vec{l}\times\vec{q}|}\frac{\vec{p}\times\vec{q}}{|\vec{p}\times\vec{q}|}\,. \tag{3.18}$$

From that ϕ can be derived attributing the sign according to

$$sign(\phi) = sign\left(\frac{(\vec{q}\times\vec{l})\cdot\vec{p}}{|(\vec{q}\times\vec{l})\cdot\vec{p}|}\right)\,. \tag{3.19}$$

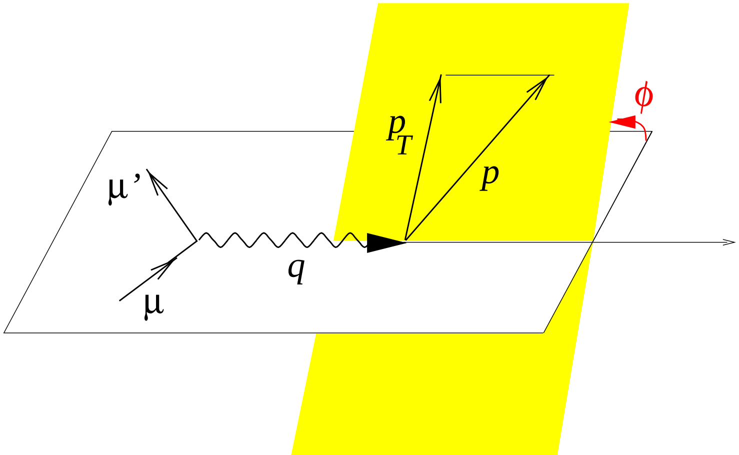

Figure 3.4: Definition of the azimuthal angle ϕ of the produced hadron.

This ϕ-dependence has several sources of which the two most important ones, the Cahn effect and QCD, are discussed in the following sections (Sec. 3.2.1 and 3.2.2). A

[4] The spatial coordinates x, y and z are denoted in roman in order to distinguish them from the kinematic variables x, y and z which are denoted in italic.

third mechanism which contributes to the ϕ-dependence of the cross section is the *final state interaction* [Ber80]. The contribution to $\langle\cos\phi\rangle$ due to this effect is opposite in sign to the others. Like the Cahn effect, final state interaction is a non-leading twist phenomenon. All of these effects lead to an asymmetry in the scattering angle of the struck *quark* which in the following is denoted ϕ_q in order to be clearly distinguished from the azimuthal angle ϕ of the *hadron*. Through fragmentation (Section 3.2.3) the asymmetry in the scattering direction of the quark translates into an azimuthal angular asymmetry of the observed hadrons.

3.2.1 The Cahn Effect

The first mechanism to be considered is a pure leading order QED effect. Although known before, the corresponding azimuthal asymmetry is named the "*Cahn asymmetry*" or the "*Cahn effect*" after R. N. Cahn who published a detailed derivation in 1978 [Cah78]. According to Cahn, the transverse momentum k_T from the so-called *Fermi motion* of the struck quark with respect to the nucleon momentum leads to an asymmetry in the azimuthal *quark* scattering angle. The order of magnitude of the intrinsic quark momentum can be estimated by exploiting the uncertainty principle. Assuming a nucleon diameter of 1 fm and using $\hbar c \approx 0.2\,\mathrm{GeV}\cdot\mathrm{fm}$ this yields a lower limit of approximately $0.2\,\mathrm{GeV}/c$.

Following Cahn's derivation of the resulting angular asymmetry, only the case of charged lepton scattering will be discussed here, while the neutrino scattering is also covered in the publication. The basic calculations are performed in the parton model which means that the scattering process is treated as the interaction of a free massless quark with an incoming massless lepton. In this simple case the cross section of the reaction can be written as

$$\sigma \propto s^2 + u^2 \tag{3.20}$$

with s and u being the Mandelstam variables

$$s := (\mathbf{l}+\mathbf{k})^2 = 2\,\mathbf{l}\cdot\mathbf{k} \tag{3.21}$$

$$u := (\mathbf{l}-\mathbf{k}')^2 = -2\,\mathbf{l}\cdot\mathbf{k}'\,. \tag{3.22}$$

In the photon-nucleon centre-of-mass frame the lepton and the quark carry transverse momenta with respect to the main axis, which is the virtual photon and proton direction of motion. Therefore the quark four-momentum $\mathbf{k}$ can be decomposed like

$$\mathbf{k} = x\mathbf{P} + \mathbf{k}_T \tag{3.23}$$

(see Fig. 3.5). The lepton four-momentum has the representation

$$\mathbf{l} = (E, l_\mathrm{x}, 0, l_\mathrm{z}) \tag{3.24}$$

since the lepton scattering plane defines the xz-plane. Using

$$\mathbf{k}_T = (0, k_T\cos\phi_q, k_T\sin\phi_q, 0) \tag{3.25}$$

one can easily see that the products (3.21) and (3.22) carry a $\cos\phi_q$-dependence. In the deep inelastic limit they can be approximated as

$$s \approx x(1 - \frac{k_T}{Q}\sqrt{1-y}\,\cos\phi_q) \tag{3.26}$$

$$u \approx x(1-y)(1 - \frac{k_T}{Q\sqrt{1-y}}\,\cos\phi_q)\,. \tag{3.27}$$

From these expressions s^2 and u^2 can be calculated and one obtains for the cross section[5]

$$\frac{d\sigma}{d\phi_q} \approx x^2[(1+(1-y)^2) - 2\frac{k_T}{Q}(2-y)\sqrt{1-y}\cos\phi_q + \frac{k_T^2}{Q^2}(1-y)\cos 2\phi_q]\,. \tag{3.28}$$

It is obvious how the intrinsic direction of motion of the quark influences the s^2-contribution to the ϕ-dependence in this cross section: s is the centre-of-mass energy of the lepton-nucleon system. The projection of the transverse part of the quark-momentum and the projection of the transverse lepton-momentum with respect to the photon-nucleon line of motion onto the lepton-scattering plane can either be parallel or anti-parallel to each other depending on the random motion of the quark in the nucleon. In case these projections of the momenta are parallel, which corresponds to a quark scattering angle in the range $-\pi/2 < \phi_q < \pi/2$, this results in a lower centre-of-mass energy and hence in a lower cross section compared to the case where the momenta are anti-parallel ($\phi_q < -\pi/2$ or $\phi_q > \pi/2$). This explains the negative $\cos\phi_q$-contribution.

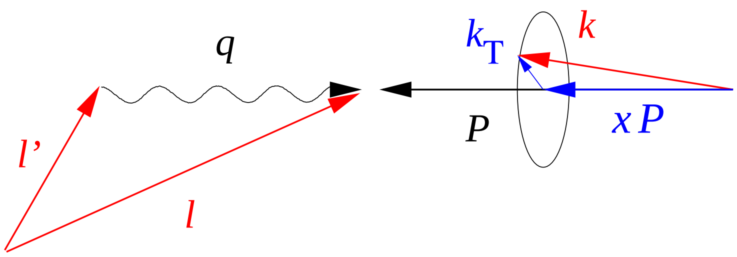

Figure 3.5: Decomposition of the quark momentum into a longitudinal (xP) and transverse (k_T) component with respect to the nucleon momentum

The $\cos(n\phi)$-*moments* of the cross section $\frac{d\sigma}{d\phi}$ are defined as

$$\langle\cos(n\phi)\rangle := \frac{\int_{-\pi}^{\pi}\cos(n\phi)\frac{d\sigma}{d\phi}d\phi}{\int_{-\pi}^{\pi}\frac{d\sigma}{d\phi}d\phi}\,. \tag{3.29}$$

For a cross section of the form

$$\frac{d\sigma}{d\phi} = a_0 + \sum_{n=1}^{N} a_n\cos(n\phi) + b_n\sin(n\phi) \tag{3.30}$$

[5]Making use of the trigonometric identity $2\cos^2\phi = 1 + \cos 2\phi$.

the $\cos(n\phi)$-moments can be calculated from the coefficients a_n according to

$$\langle \cos(n\phi) \rangle = \frac{a_n}{2a_0}\,. \tag{3.31}$$

Especially for the cross section in Eq. 3.28 one obtains:

$$\langle \cos\phi_q \rangle \propto -\frac{k_T}{Q} f_1(y) \tag{3.32}$$

$$\langle \cos 2\phi_q \rangle \propto \frac{k_T^2}{Q^2} f_2(y) \tag{3.33}$$

where the functions $f_1(y)$ and $f_2(y)$ contain the dependence of the moments on the fractional energy transfer y to the photon

$$f_1(y) = \frac{(2-y)\sqrt{1-y}}{1+(1-y)^2} \tag{3.34}$$

$$f_2(y) = \frac{1-y}{1+(1-y)^2}\,. \tag{3.35}$$

If k_T vanishes, the moments are zero and no angular modulation can be derived from this simple model. The extraction of the corresponding moments of the distribution of the hadron angle ϕ from the COMPASS data is the goal of this diploma thesis and will be described in Chap. 4.

At leading twist and zeroth order in α_s, the semi-inclusive cross section (Eq. 3.13) is independent of ϕ. This means that the Cahn effect is a higher twist phenomenon. An expression for the full cross section, employing an empiric ansatz for the fragmentation function, has e.g. been given by Chay et al. [CES92]. Another representation of the cross section has been presented by A. Efremov [Efr03, MT96]. Here it is expressed in terms of the structure functions F_1, $f^\perp$ and $h_1^\perp$, of which the latter two are spin-dependent, and the fragmentation functions D_1 and $H_1^\perp$:

$$\frac{d^4\sigma}{dx\,dy\,dz\,d\phi} \propto xF_1(x)D_1(z) - \frac{M}{Q}x^2 f^\perp(x)D_1(z)\cos\phi + xh_1^\perp(x)H_1^\perp(z)\cos 2\phi\,. \tag{3.36}$$

This representation is of special interest in view of the contributions the Cahn analysis can make to the understanding of *transversity*. The cross section given in Eq. 3.36 contains the *Collins fragmentation function* $H_1^\perp(z)$. Thus the Cahn effect provides access to spin-dependent phenomena.

In case spin effects are considered, the hadronic tensor (Eq. 3.7) in the spin averaged DIS cross sections gets supplemented by an antisymmetric contribution. This description requires further, spin-dependent structure functions, such as the said $f^\perp$ and $h_1^\perp$, as well as the corresponding fragmentation functions, e.g. $H_1^\perp$, to be introduced. One of the most interesting members of the former class is the structure function $h_1^\perp(x)$, which is called the transversity function (see e.g. [BDR02] for an extended treatment of transverse spin phenomena). The knowledge of $H_1^\perp(z)$ is necessary to extract $h_1^\perp(x)$ from the Collins asymmetry

$$A_{UT}^{\sin(\phi+\phi_S)} \propto h_1^\perp(x) H_1^\perp(z)\,, \tag{3.37}$$

which can be obtained in SIDIS measurements with transversely polarised target [Col93, MT96, EGS03].

3.2.2 QCD Asymmetries

Even in case that there is no intrinsic transverse momentum of the quarks in the nucleon one expects a nontrivial ϕ-dependence of the cross section. This is due to QCD processes which, in contrast to the Cahn effect, occur already in leading twist. Gluon radiation introduces non-uniformly distributed transverse momentum and leads to angular modulation (see Fig. 3.6). The source of the angular asymmetry of the gluon radiation is the interference of the incoming and outgoing quark, which can be regarded as a anti-quark pair. This interference is constructive inside the cone defined by the pair. Outside the cone it is destructive. Hence gluons are preferentially emitted inside the cone. The recoil that is transferred to the struck quark in this configuration causes a negative $\cos\phi_q$-moment in the cross section [CES92].

The resulting ϕ-dependence has been calculated by Georgi and Politzer in 1977 [GP78]. At first order in α_s and in the limit of large z their perturbation calculation yields for the complete cross section including fragmentation

$$\langle\cos\phi\rangle \approx -\kappa\frac{\alpha_s}{2}\sqrt{1-z}f_1(y)\,. \tag{3.38}$$

κ is a constant which is about 1. At values of z very close to 1 obviously the QCD contribution vanishes. In this case the emitted gluon carries only a very small fraction of the energy of the virtual photon. Therefore it has low total momentum and consequently the transverse momentum component is small. This means that only little transverse momentum can be transferred to the quark through recoil. The full expressions for the cross section can be found e.g. in the two said publications. It is worth mentioning that the leading twist cross section given in [CES92] depends on x in all orders of α_s (see Eq. 3.13 for the 0th order), while the Cahn contribution shows no dependence on that variable.

3.2.3 Fragmentation

Fragmentation introduces an additional randomly distributed transverse momentum $\vec{p}_T^{\,f}$ by quark anti-quark production. This leads to smearing of the hadron transverse momentum distribution compared to the quark distribution and therefore to a reduction in the observed asymmetry. The transverse momentum of the hadron is

$$\vec{p}_T = z\vec{k}_T + \vec{p}_T^{\,f} \tag{3.39}$$

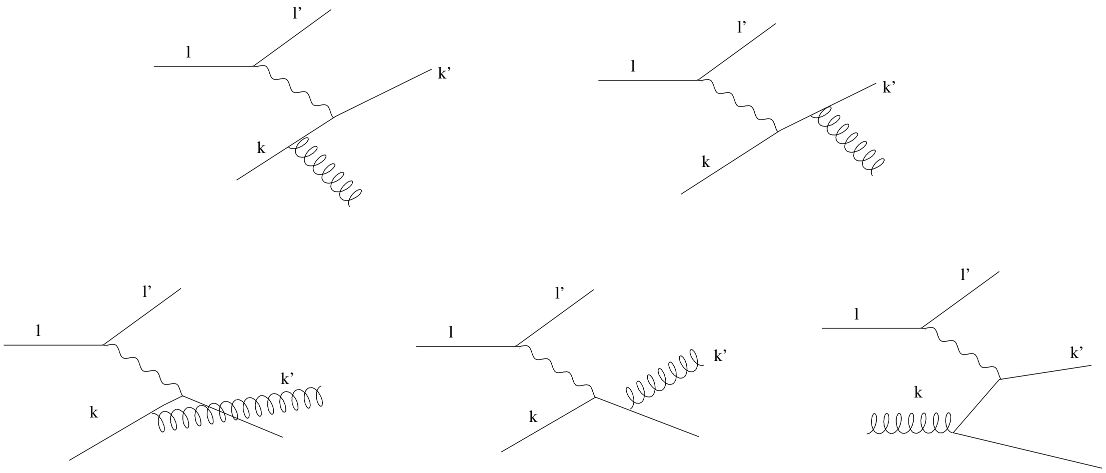

Figure 3.6: First order QCD processes contributing to the azimuthal angular modulation

where here k_T is the transverse momentum of the quark after the scattering process (which may differ from k_T before scattering due to gluon radiation as described in Section 3.2.2). Since $z \leq 1$ the first contribution always diminishes the effect compared to the expectation on the quark level. From Eq. 3.39 one can determine the mean value $\langle k_T^2 \rangle$ according to

$$p_T^2 = z^2 k_T^2 + 2z\,\vec{k}_T \cdot \vec{p}_T^{\,f} + (p_T^f)^2 \tag{3.40}$$

from which one obtains

$$\langle p_T^2 \rangle = \langle z^2 \rangle \langle k_T^2 \rangle + \langle (p_T^f)^2 \rangle \,. \tag{3.41}$$

The average value $\langle (p_T^f)^2 \rangle$ is of about the same order of magnitude as $\langle k_T^2 \rangle$.

Chapter 4

Analysis of the Cahn Asymmetries

This chapter is dedicated to the extraction of the $\cos\phi$- and $\cos 2\phi$-moments in the unpolarised cross section from the COMPASS data. Sec. 4.1 starts with the selection of a suited data sample. The Cahn analysis itself is the subject of Sec. 4.2. Sec. 4.3 shows the results of this analysis, while Sec. 4.4 deals with the sources of systematic errors.

4.1 Data Selection and Statistics

Not all of the recorded events are suited for the analysis of the Cahn asymmetry. The cuts used to select an adequate sample include particle identification and restrictions on event kinematics to separate the desired SIDIS events from other kinds of processes. Additionally, parts of the data are sorted out because in quality checks or already during the data taking they turned out to be biased due to instabilities in the detector acceptance.

From the events which pass all these requirements, samples of hadron tracks are selected, which are the input for the actual analysis of the Cahn effect. In the course of this analysis two different hadron samples are considered: The pure QED Cahn effect shows up in the distribution of the azimuthal angle ϕ of so-called *leading hadrons*. In addition also a sample of hadrons is analysed on which no leading hadron selection is performed. It is referred to as the *all hadron sample* in this thesis. This sample is more adequate for accessing the QCD contributions which are not limited to the leading hadrons. The leading hadrons make a sub-sample of all hadrons, which contains only those hadrons which fulfil dedicated additional requirements (see Sec. 4.2.3).

4.1.1 Event Selection

Only events where the primary vertex is reconstructed are considered. This means that a beam particle has been reconstructed and is associated with this vertex. Events with more than one primary vertex due to ambiguous beam or scattered muon assignment are rejected. This affects about 0.35% of the events with primary vertices. Thus the corresponding kinematic variables can unambiguously be calculated. The event can only be a semi-inclusive candidate if in addition the vertex contains a scattered muon and at least one additional track which is considered as a hadron candidate. All tracks with high reduced χ^2 of the fit of the track to the associated hits in the spectrometer, abbreviated as χ^2_r, are discarded by a cut on $\chi^2_r < 10$. Such tracks may cause the scattering planes of the muon and the hadron to be badly reconstructed and thus affect the azimuthal angle ϕ (see Fig. 4.1 for the distribution of χ^2_r for the raw sample of hadron candidates. Note that "raw" means a sample of semi-inclusive event candidates with scattered muon and one additional outgoing track, where a cut on $Q^2 > 1\,(\mathrm{GeV}/c)^2$ is applied.).

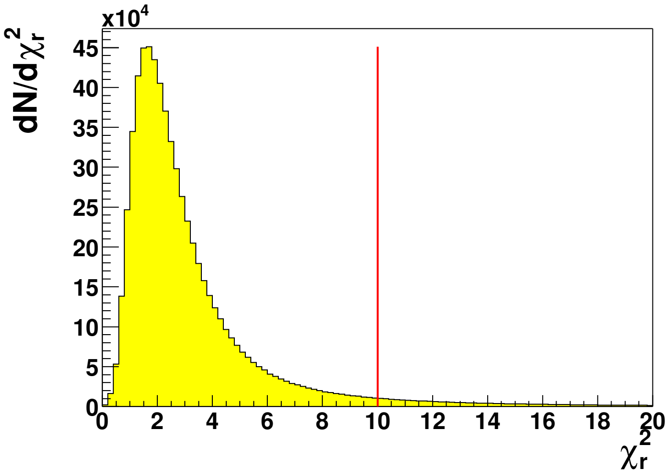

Figure 4.1: χ^2_r - distribution of the hadron tracks (raw sample). All tracks at χ^2_r-values below the line are accepted.

Particle Identification

The beam particle and scattered muon are identified using functions[1] from PHAST [Ger04]. To improve the muon identification, the following additional cuts are applied on the μ' candidates:

- The μ' track is required to have caused a signal in the last hodoscope corresponding to the event trigger type.
- A cut on the hadronic interaction lengths $X/X_0 > 30$ passed by the μ' is applied in order to discard those events where a hadron wrongly passed the muon identification performed by CORAL. Thus this cut removes the excess of events in the region of 0.8 in the y-distribution (c.f. Figure 4.4) which are caused by misidentified hadrons.
- Further cleaning of the muon sample is gained by a cut on the energy deposited in one of the HCALs. If calorimeter information is available the maximum energy is

[1] `isBeam()` and `iMuPrim()`

limited by the requirement $E_{cal}/p < 0.3$, where E_{cal} is the total energy deposited in one of the calorimeters (c.f. Figure 4.2) and p is the momentum measured in the spectrometer.

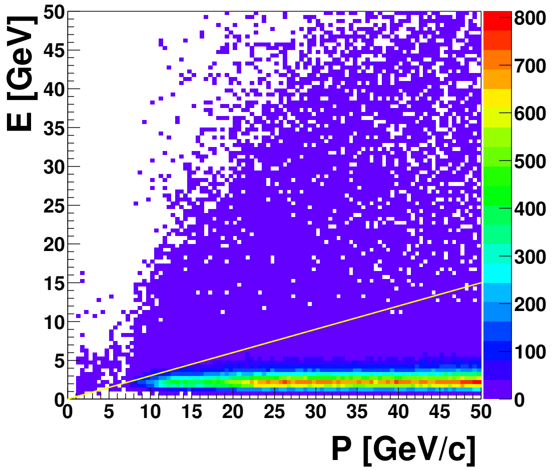

Figure 4.2: Energy of the muon candidates measured in one of the calorimeters vs. the muon momentum. The line marks the cut at $E/p < 0.3$.

The hadron candidates must fulfil the following conditions:

- Tracks which are reconstructed only in the fringe field of the first spectrometer magnet are excluded from the analysis by requiring the last hit associated with the track to be behind SM1. Fringe field reconstructed tracks are biased with large momentum uncertainties[2].
- If the number of interaction lengths passed is large, the probability for a hadron candidate to be a falsely identified muon (pile-up muons) rises. In order to get rid of these muons a cut on $X/X_0 < 10$ is applied.
- For the same reason a minimum energy measured in the hadronic calorimeters is demanded for. Tracks for which no energy measurement from one of the calorimeters exists are not included in the analysis. A hadron candidate is also rejected if an energy measurement exists and $E_{cal}/p < 0.3$, where E_{cal} is the total energy deposited in one of the calorimeters (c.f. Figure 4.3).

Cuts on Inclusive Kinematic Variables

Further conditions for an event to be accepted for the analysis are the following cuts on the event kinematics:

[2]The momentum measurement is difficult here, since outside the magnet the field is weak and therefore also the resulting bend of the track.

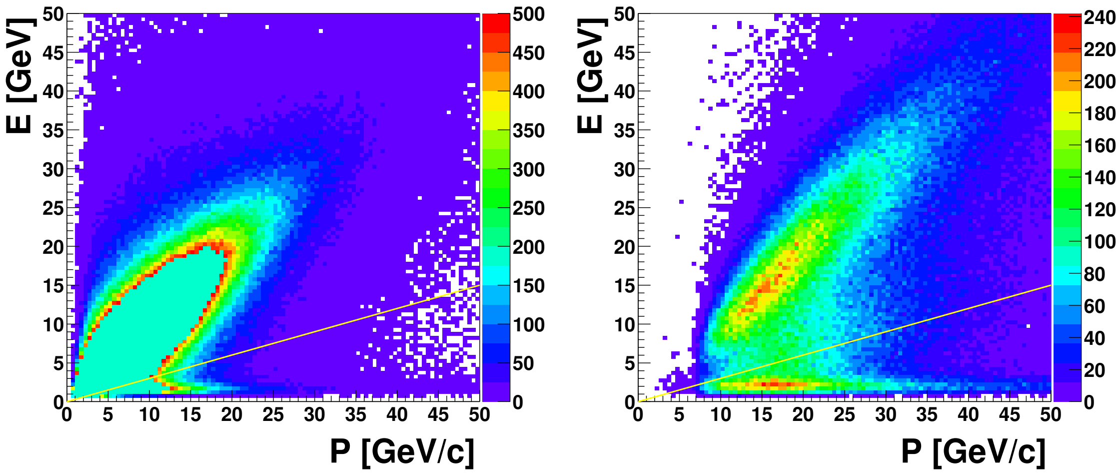

Figure 4.3: Energy measured in HCAL1 (left) and HCAL2 (right) vs. momentum of the hadron candidate. Note that there is a cutoff at 500 entries per bin in the plot at left hand.

- In order to select the deeply inelastic scattering events, a cut on $Q^2 > 1\,(\mathrm{GeV}/c)^2$ is applied.
- A cut on $W > 4\,\mathrm{GeV}/c^2$ avoids the resonance region.
- High y events are strongly affected by radiative corrections which are not yet included in the Monte Carlo simulation. Therefore they are removed from the sample by a cut on $0.1 < y < 0.9$.

For the distributions of these kinematic variables in the raw and in the resulting event sample see Fig. 4.4.

Cuts on Hadronic Kinematic Variables

No particle identification was used to distinguish different types of hadrons. About 80% of the *all hadron* sample (75% of the leading hadron sample, see Tab. B.7 in App. B.1) consists of pions, hence all particles are assumed to have pion mass in order to calculate the quantities z, x_F and E. The following is required for the kinematic variables of the hadron tracks selected for this analysis:

- p_T of the particle, with respect to the virtual photon direction, has to be larger than $0.1\,\mathrm{GeV}/c$. This requirement assures that the azimuthal angle ϕ is measured properly.
- $x_F \geq 0$. In the reconstructed Monte Carlo and the data there are only very few tracks with negative x_F. These tracks correspond to target fragments which are scattered backward in the centre-of-mass system, which corresponds to geometrical regions

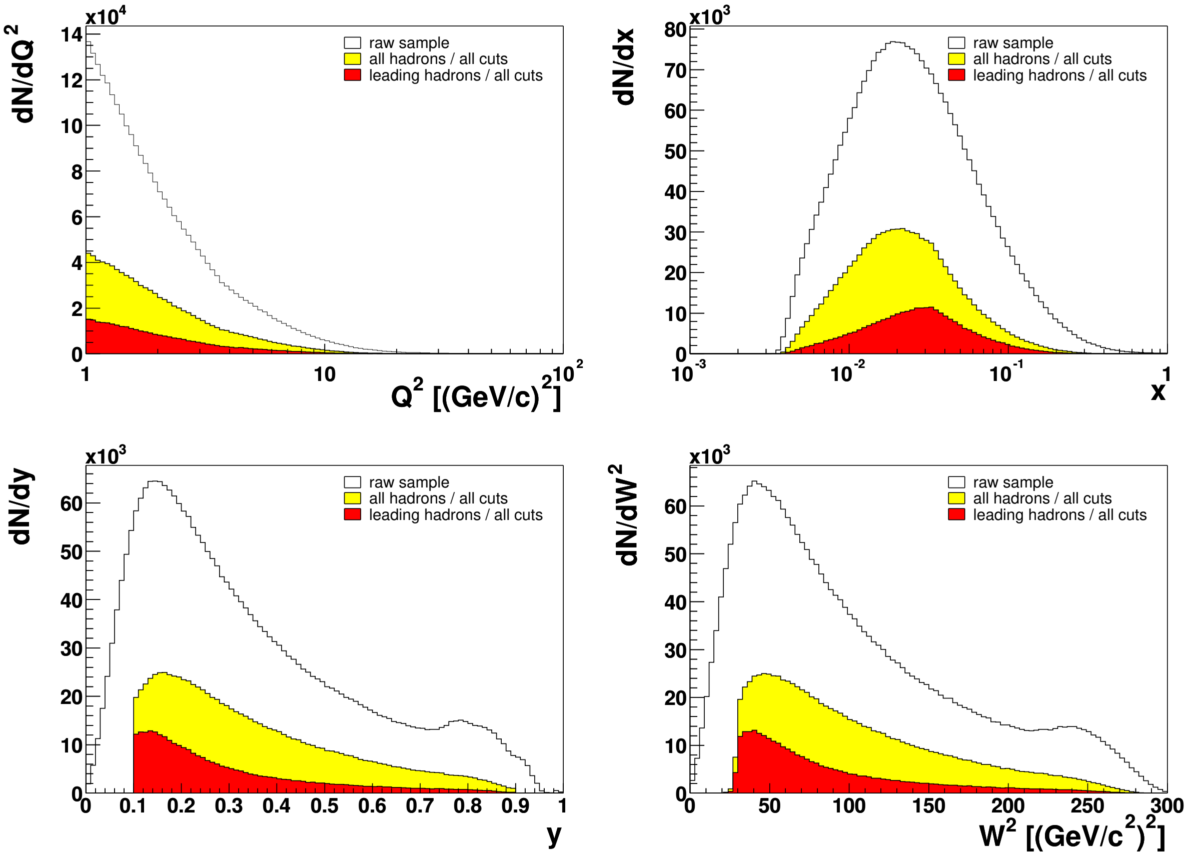

Figure 4.4: Distribution of virtual photon invariant masses (top left), the Bjørken scaling variable x (top right), fractional energy transfer y to the virtual photon (bottom left) and invariant mass of the photon-nucleon system (bottom right); The white region is the distribution of the raw event sample while the light region marks the final *all hadron* sample and the dark region finally is the leading hadron sample.

outside the acceptance of the COMPASS spectrometer. Without the information on the data and reconstructed Monte Carlo, it is impossible to determine the acceptance function and to restore the full ϕ-distribution of the data in this kinematic region. Thus the x_F-cut removes these hadrons from the generated Monte Carlo as well.

- Only for *leading hadrons* in addition $z > 0.3$ is demanded (see Section 4.2.3).

For the distributions of z, x_F and p_T^2 of the resulting hadron samples see Figure 4.5.

Target Geometry

The COMPASS target is shifted and inclined with respect to its nominal position. This inclination is not implemented in the Monte Carlo which is used to correct for the spectrometer acceptance (see Sec. 4.2.4). In order to have comparable vertex distributions and therefore detector acceptance in Monte Carlo and real data, a strict target cut is applied, which ensures that both, the Monte Carlo target and the real target completely contain the volume considered. The maximum deviation of the axis of the inclined target with respect to the nominal axis is 3 mm [Gof03]. Thus a barrel of 1.2 cm radius instead of the actual 1.5 cm around the nominal axis position should fulfil the requirement mentioned above.

Furthermore, the target is not completely filled with polarised material since the ^{6}LiD pieces accumulate in the lower part of the target volume. Hence the cut on the target radius is chosen even more strict ($r < 1.1$ cm) in order to make sure that poorly filled spots of the volume are excluded.

Therefore the following is required for the vertex position of the accepted events (c.f. Figure 4.7):

- Longitudinal position between $-100 < \mathrm{z} < -40$ cm (upstream cell), or $-30 < \mathrm{z} <$ 30 cm (downstream cell).
- Transverse position at a radius $r < 1.1$ cm from the *nominal* target axis.

4.1.2 Run Selection

Only the week P2D of data taking is used for the analysis. This is the only 2002 period for which Monte Carlo is presently available which is produced with a version of the reconstruction software CORAL corresponding to the CORAL version used for the processing of the real data. Furthermore only for this period detector efficiencies have been extracted from the measured data and are put into the Monte Carlo production. Nevertheless, there is plenty of statistics available for a detailed analysis. Furthermore, the statistical error of the result is presently dominated by the contribution of the Monte Carlo.

All spills tagged as "bad" during quality checks are removed [Kor03a, Kor03b] to improve the quality of the data. In addition the runs 22041, 22042, 22043, 22063 and 22306 are completely excluded from the analysis because of problems with the hardware or DAQ

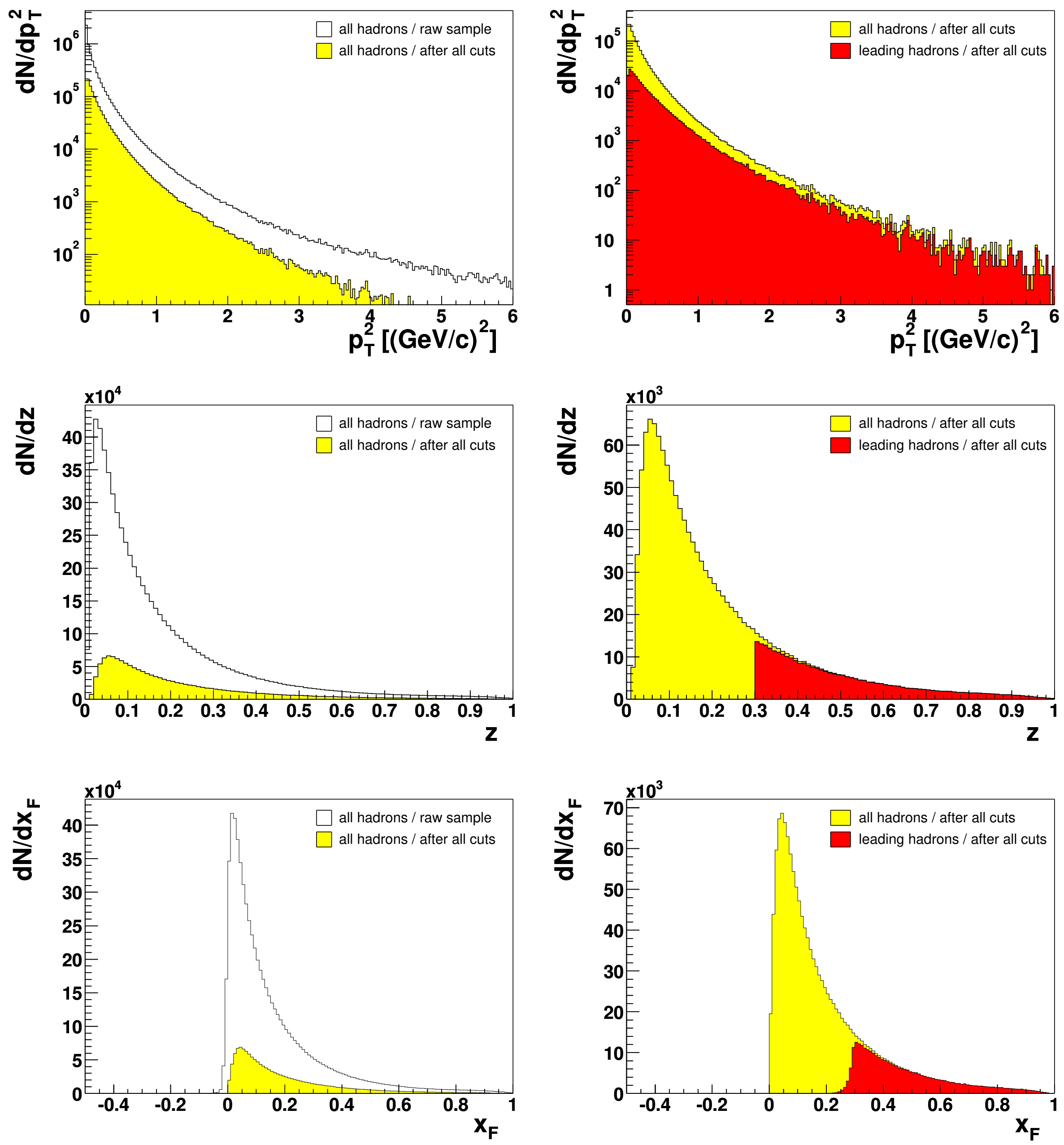

Figure 4.5: Kinematic variables of the analysed hadron sample; Top row: squared transverse momentum p_T^2; Middle row: relative fraction of energy z; Bottom row: longitudinal momentum component x_F; Left: raw sample (white) and after all cuts are applied, right: cut samples for all hadrons (light) and leading hadrons (dark). Note that the light spectra on the left and on the right are identical.

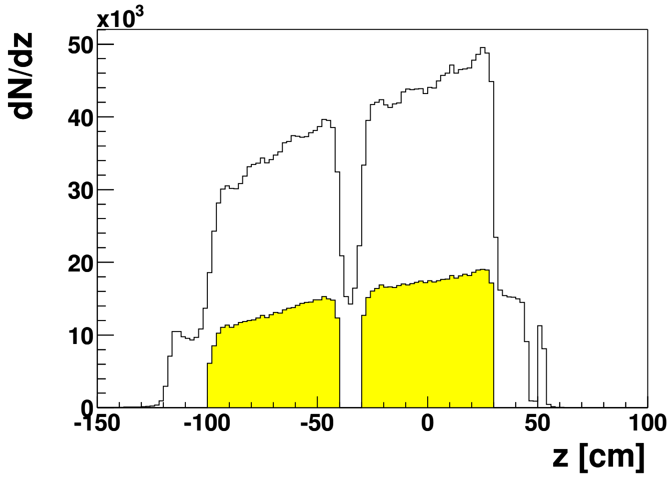

Figure 4.6: Distribution of vertices in z-direction (real data).

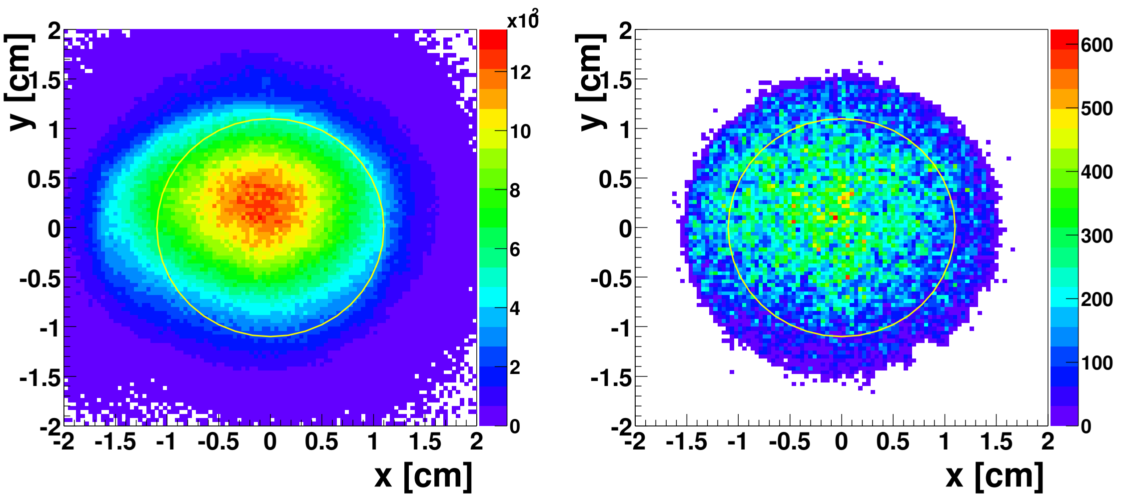

Figure 4.7: Distribution of vertices in radial direction (left: real data; right: reconstructed Monte Carlo). The circle indicates the cut applied on the target radius. Note that the vertex distribution follows a convolution of the distribution of the target material and the beam profile. The vertex distribution in the Monte Carlo is shifted with respect to the (0,0) position because of the tilted incidence of the beam on the target, which is simulated in the Monte Carlo. The inclination of the target itself in contrast is not simulated.

occurring during the data taking [log02]. The runs 22153, 22154, 22176 and 22331 were recorded during the field rotation, which means that the target solenoid field changed during the run. Under these conditions the tracking and vertexing is problematic and thus up to now these runs are omitted from the analysis.

4.1.3 Statistics

In Table 4.1 the numbers of events and hadrons of the resulting Monte Carlo and data samples are listed. Note that the number of reconstructed Monte Carlo events is less than one third of the real data. For a more detailed listing of the losses due to each cut see the tables in Appendix B.1 on Page 91 and following.

	data	**generated MC**	**reconstructed MC**
events (raw sample)	$2.67 \cdot 10^6$		
events after all cuts	$0.90 \cdot 10^6$	$0.59 \cdot 10^6$ $(0.29 \cdot 10^6)$	$0.27 \cdot 10^6$ $(0.11 \cdot 10^6)$
hadrons after all cuts	$1.38 \cdot 10^6$	$1.58 \cdot 10^6$ $(0.31 \cdot 10^6)$	$0.39 \cdot 10^6$ $(0.11 \cdot 10^6)$
hadron multiplicity	1.54		1.43 (1.0)
leading hadrons	$0.30 \cdot 10^6$		

Table 4.1: Number of events and hadrons in data and Monte Carlo. The values in brackets correspond to the Monte Carlo samples with the additional cut on $z > 0.3$.

4.2 Measurement of the Azimuthal Asymmetry

The Cahn asymmetry can be extracted from the angular modulation in the count rates of unpolarised muon nucleon scattering as described in Chapter 3.2.1. The analysis starts with the determination of the resolution in the azimuthal angle (Sec. 4.2.1). The treatment of the contributions to the angular distribution due to the polarised target and beam used at COMPASS is described in Section 4.2.2, while the leading hadron selection algorithm is outlined in 4.2.3. Since the ϕ-dependence of the count rate is also influenced by the geometrical acceptance of the spectrometer, a correction using Monte Carlo is necessary. This is the subject of Section 4.2.4. This analysis is performed separately for positively and negatively charged hadrons and for the two target cells. To extract the kinematic dependence of the moments, the sample is subdivided into several bins in the kinematic variables (see the tables in App. B.2). The $\cos\phi$- and $\cos 2\phi$ moments can then be calculated from the parameters of a fit to the resulting ϕ-distribution (c.f. Section 4.2.5). The results for the two cells are finally combined to an overall asymmetry by calculating the weighted average of both.

4.2.1 Angular Resolution and Binning

The azimuthal angle ϕ of the reconstructed hadron is calculated according to Equations 3.18 and 3.19 and filled into histograms of 18 bins ranging between $-\pi < \phi < +\pi$. On the one hand this number of bins is large enough to ensure a good result when fitting four parameters to the distribution. On the other hand the number of bins may not be chosen too large, since the bin width should be larger than the angular resolution of the measurement.

The angular resolution of the COMPASS spectrometer is estimated by comparing the generated azimuthal angle of a Monte Carlo event to the angle reconstructed in the simulation of the detector. For the *all hadron* sample the distribution of

$$\delta\phi := \phi_{gen} - \phi_{rec}\,, \tag{4.1}$$

where ϕ_{gen} is the azimuthal angle of a generated hadron and ϕ_{rec} is the azimuthal angle of the same hadron after the reconstruction, has a full width at half maximum of 0.045 rad, which is a measure for the resolution. A binning of 18 bins in an interval of 2π corresponds to a bin width of 0.35 rad which is more than seven times as much (see Fig. 4.2.1). This number of bins therefore is an adequate choice for the given resolution in ϕ.

4.2.2 Polarisation Effects

The effect of the target polarisation can be removed since the data are taken with two opposite target polarisations as described in Chapter 2.1. For each hadron charge, target cell and kinematic bin two ϕ-distributions H and H' are produced, containing events from the outward and inward configuration of the target polarisation respectively (see Fig. 2.4,

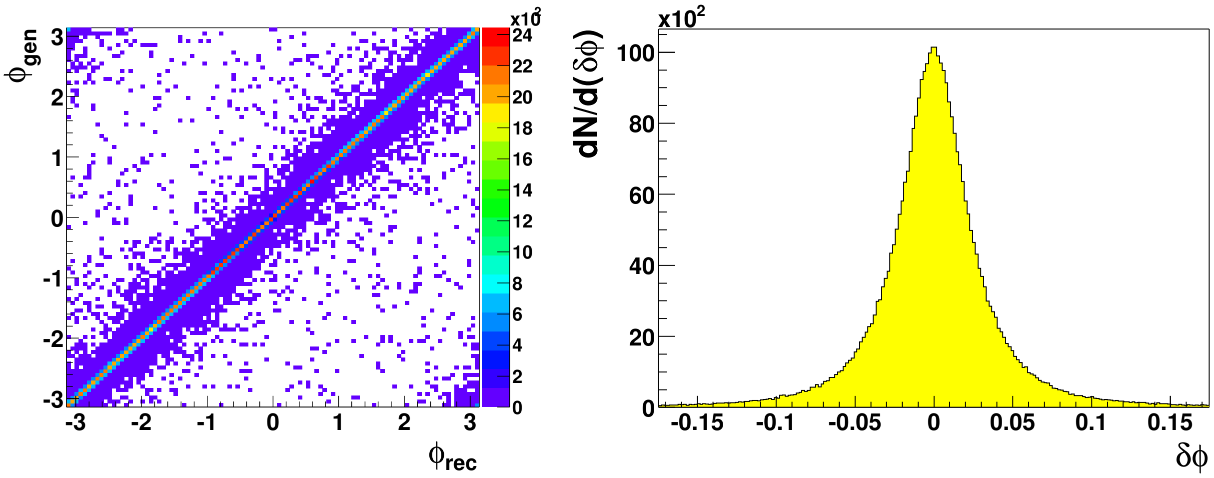

Figure 4.8: Angular resolution of the Monte Carlo data after all cuts. Left: ϕ_{rec} vs. ϕ_{gen}; Right: Distribution of $\delta\phi$. The displayed range corresponds to $2\pi/18$, i.e. the width of one bin.

Pg. 7). The polarisation is cancelled by combining these distributions using a weight in order to make sure that the mean polarisation vanishes:

$$H + \frac{|P_\Sigma|}{|P'_\Sigma|}H' \tag{4.2}$$

with P_Σ and P'_Σ being

$$P_\Sigma = \sum_{i\in H} P_i\,, \qquad P'_\Sigma = \sum_{i\in H'} P_i\,. \tag{4.3}$$

P_i denotes the target polarisation of event number i and the sum runs over all entries into the distributions H and H' respectively. Thus in the case of the *all hadron* sample the event is weighted with the multiplicity of the hadrons.

It is not possible to get rid of beam spin effects by applying a corresponding weighting method, since the beam polarisation cannot be changed. However, it contributes only a $\sin\phi$-moment to the cross section which does not spoil the $\cos\phi$- and $\cos 2\phi$-moments caused by the Cahn effect. Moreover, since any $\sin\phi$-dependence due to the target spin should be removed by the method described above, it should be possible to obtain a beam-spin asymmetry from the remaining $\sin\phi$-moment (see App. A).

4.2.3 Leading Hadron Selection

The predictions made by Cahn (see Sec. 3.2.1) concern the hadrons which contain the quark originally struck by the γ^*. These hadrons are enriched in a sample of so-called *leading hadrons*, which carry the largest fraction z of the virtual photon energy. Among all the hadrons produced in a given event, the leading hadron is the one which has highest probability to contain the struck quark. Therefore the tracks which have maximum z in a given event (after all cuts which are described in Sec. 4.1, except for the cuts on the hadron kinematics) are selected to investigate the Cahn effect.

Errors in this selection mainly occur if the track of the real leading hadron has not been reconstructed, especially if it was not charged, since the COMPASS spectrometer in the muon setup [Bau96] can track only charged particles. Therefore the hadron candidate with the largest z needs to fulfil one of the following criteria:

- z is larger than the *missing* z in the event. The missing z is the maximum fraction of energy which could be carried by neutral or undetected charged particles. It is calculated according to

$$z > 1 - \sum_i z_i \,, \tag{4.4}$$

  where i runs over all detected charged hadron candidates.

- If the hadron does not pass the missing z cut, it is nevertheless accepted if the calorimeter information of the event shows no sign of a neutral particle with higher energy than the energy of the hadron candidate. Such a sign would be an energy deposit (referred to as *cluster*) which
  - is not associated to a track and
  - has an energy larger than the corresponding energy of the leading hadron candidate.

The correlation between the energy measured in the spectrometer and the energy which would have been measured in the calorimeters is calculated according to the relations in Table 4.2. The energy resolution of the calorimeters is taken into account by allowing the leading hadron candidate to have a 2σ excess of energy measured in the spectrometer with respect to a calorimeter cluster associated to a potential neutral leading hadron. Therefore, it is required that there is *no* cluster which fulfils

$$E_{cluster} > E_{LH}^{HCAL} + 2\sigma_{LH}^{HCAL} \tag{4.5}$$

with the energy resolutions σ^{HCAL1} and σ^{HCAL2} as listed in Table 4.2.

HCAL1	**HCAL2**
$E^{HCAL1} = 0.4\,\mathrm{GeV} + 1.22 \cdot E^{SPEC}$	$E^{HCAL2} = 0.3\,\mathrm{GeV} + 1.06 \cdot E^{SPEC}$
$\sigma^{HCAL1} = 0.8\,\mathrm{GeV}\sqrt{E^{HCAL1}/\mathrm{GeV}}$	$\sigma^{HCAL2} = 0.6\,\mathrm{GeV}\sqrt{E^{HCAL2}/\mathrm{GeV}}$

Table 4.2: Correlation between energies measured in the calorimeter and the spectrometer (upper row) and energy resolution (lower row) of the two hadronic calorimeters [Bis04].

If a hadron passes the criteria listed above, it is considered as a leading hadron. The cuts on p_T and x_F (see Sec. 4.1.1) and the additional cut on $z > 0.3$ are applied afterwards.

The cut on z discards leading hadron candidates from a region where the contamination of non leading hadrons is still high. From Monte Carlo studies one can estimate that the contamination by misidentified leading hadrons in the sample falls below 10% if a cut at $z > 0.3$ is applied. To obtain this result the distribution of the fractional energy z_{rec} of the leading hadron candidates is compared for several classes of tracks (c.f. Figure 4.9):

- Tracks for which z_{rec} *and* the generated fractional energy z_{gen} was maximum in this event (*real* leading hadrons).
- Tracks from an event for which the real leading hadron is not reconstructed because it is an uncharged particle[3].
- Tracks from an event for which the real leading hadron is not reconstructed although it is charged (e.g. because it is scattered out of the detector acceptance).
- The sum of the three described before.
- The sum of the two classes of events with misidentified leading hadrons.

In Figure 4.9 the *efficiency* ϵ and the *purity* p of the leading hadron selection are plotted. These are defined by

$$\epsilon = \frac{\text{number of accepted candidates}}{\text{total number of candidates}} \tag{4.6}$$

$$p = \frac{\text{number of correctly id. and accepted candidates}}{\text{number of accepted candidates}} . \tag{4.7}$$

Since the purity of the leading hadron sample increases with a rising value for the cut on z, the analysis was in addition performed with cuts on $z > 0.25$ (which is the standard cut used for the transversity analysis [Bis04]), $z > 0.4$ and $z > 0.5$. In the latter case the sample should per definition contain only leading hadron tracks except for minor contamination due to the resolution in the reconstruction of z, which will be discussed in Sec. 4.4.2.

4.2.4 Acceptance Correction

The distribution of the azimuthal hadron scattering angle is strongly affected by the geometrical acceptance of the spectrometer. Therefore an acceptance correction is performed using LEPTO Monte Carlo data where the angular modulation due to the Cahn effect is not simulated [Ale03]. This Monte Carlo data contains the information of the event as produced by the event generator (*generated events*) as well as the output of the reconstruction that is performed on this event after the detector simulation (*reconstructed events*). From the reconstructed events a sample is selected which fulfils the same requirements as the real data sample (see Sec. 4.1.1), except for the leading hadron selection criteria (c.f. 4.2.4). The generated events and tracks need to pass all cuts on kinematic variables

[3] π^0, which are not recorded in the Monte Carlo sample, but only the photons from their decay, are reconstructed by combining pairs of photons with invariant mass $= m_{\pi^0}$ in the generated Monte Carlo

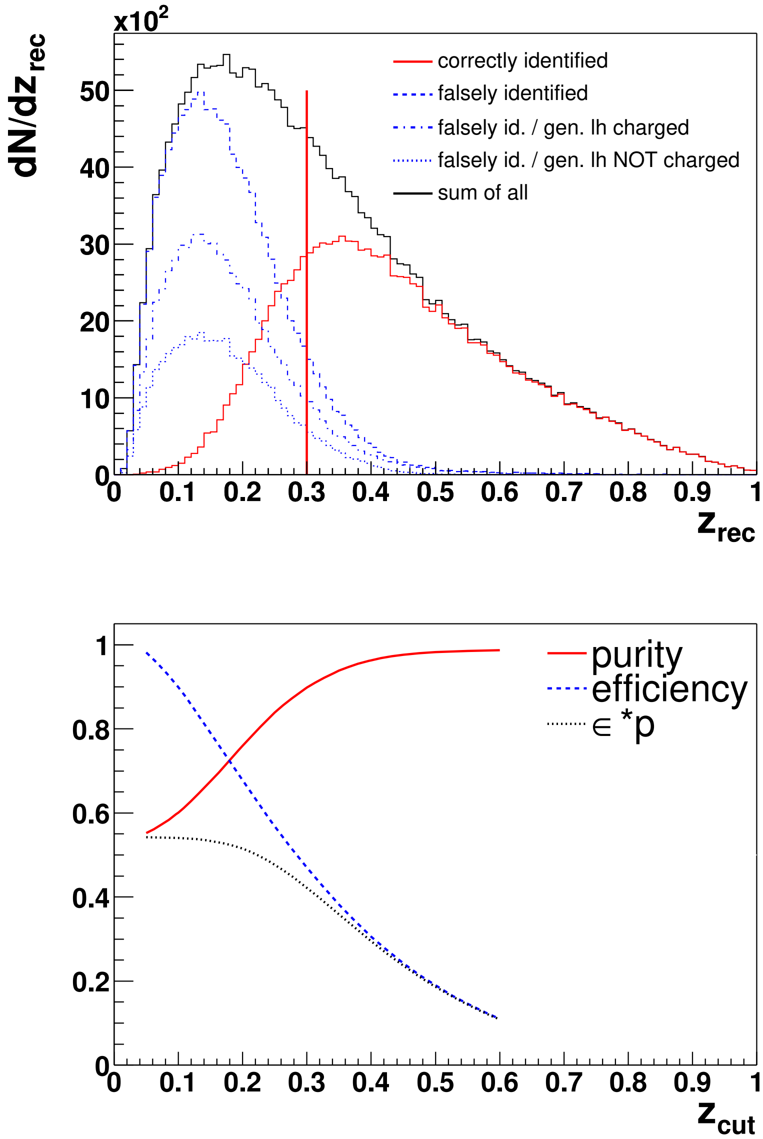

Figure 4.9: Top: Distribution of z_{rec} in the reconstructed Monte Carlo for leading hadron candidates. The vertical line marks the value of z at which the cut is applied. Bottom: Efficiency and purity of the leading hadron selection. The curves are obtained by calculating ϵ and p from the top distributions for twelve different z_{cut} and interpolating between these values. In the Monte Carlo sample considered, a selection of leading hadrons as described in this section is performed. Without the cuts on z, x_F and p_T this selection yields 235,525 leading hadron candidates. Note that no leading hadron selection is applied on the Monte Carlo sample which is used for the acceptance correction in the following analysis (see Sec. 4.2.4).

in order to be accepted for the analysis. Any properties like calorimeter energy or χ^2_r which are introduced by the detector simulation or reconstruction are not defined for the generated sample. Only tracks from the most frequently produced long living charged hadrons (π^+, π^-, K^+, K^-, p, $\bar{p}$) are taken into account. This ensures that the acceptance correction does not re-introduce electron- and muon-tracks which are discarded from the reconstructed Monte Carlo and data samples, but not from the generated sample, by the cuts on hadron identification. Correct hadron masses are used for calculating the kinematics of the Monte Carlo input while all reconstructed tracks are assigned pion mass as it is done in real data[4].

From both samples ϕ-distributions using the same binning as for the data are produced. For each histogram of real data that is to be fitted later, the acceptance function $h(\phi)$ is calculated according to

$$h(\phi) = \frac{N_{rec}(\phi)}{N_{gen}(\phi)}\,. \tag{4.8}$$

It can be interpreted as the probability for a hadron that is emitted into a certain azimuthal angle ϕ to be detected in the spectrometer. As the ϕ-resolution of COMPASS is high (as seen in Section 4.2.1), smearing effects due to detection of a hadron under a shifted angle $\phi + \delta\phi$ do not play an important role. The error of the acceptance is

$$\delta h = \sqrt{\frac{h(1-h)}{N_{gen}}} \tag{4.9}$$

which takes into account that N_{rec} follows a binomial distribution. The corrected counting rate distributions are then obtained as

$$N^{corr}(\phi) = \frac{N(\phi)}{h(\phi)}\,, \tag{4.10}$$

with the error of this expression being determined according to Gaussian error propagation:

$$\frac{\delta N^{corr}}{N^{corr}} = \sqrt{\left(\frac{\delta N}{N}\right)^2 + \left(\frac{\delta h}{h}\right)^2} = \sqrt{\frac{1}{N} + \left(\frac{\delta h}{h}\right)^2}\,. \tag{4.11}$$

As an example Figure 4.10 shows the raw distribution, the acceptance function and the corrected counting rate for the *all hadron* sample of positively charged particles, together with the fit (see Section 4.2.5) to the so obtained distribution.

The overall acceptance ranges between about 0.2 and 0.3 depending on the target cell where the vertex has been detected (c.f. Table 4.3). The cylindrical magnet coils around the target volume absorb most of the hadrons which are emitted under large opening angles. Thus the geometrical acceptance of the upstream cell is smaller than that of

[4] This assumption is made for the real data, since no identification of the hadron type is performed and the majority of all hadrons are pions (see Table B.7 on Page 94).

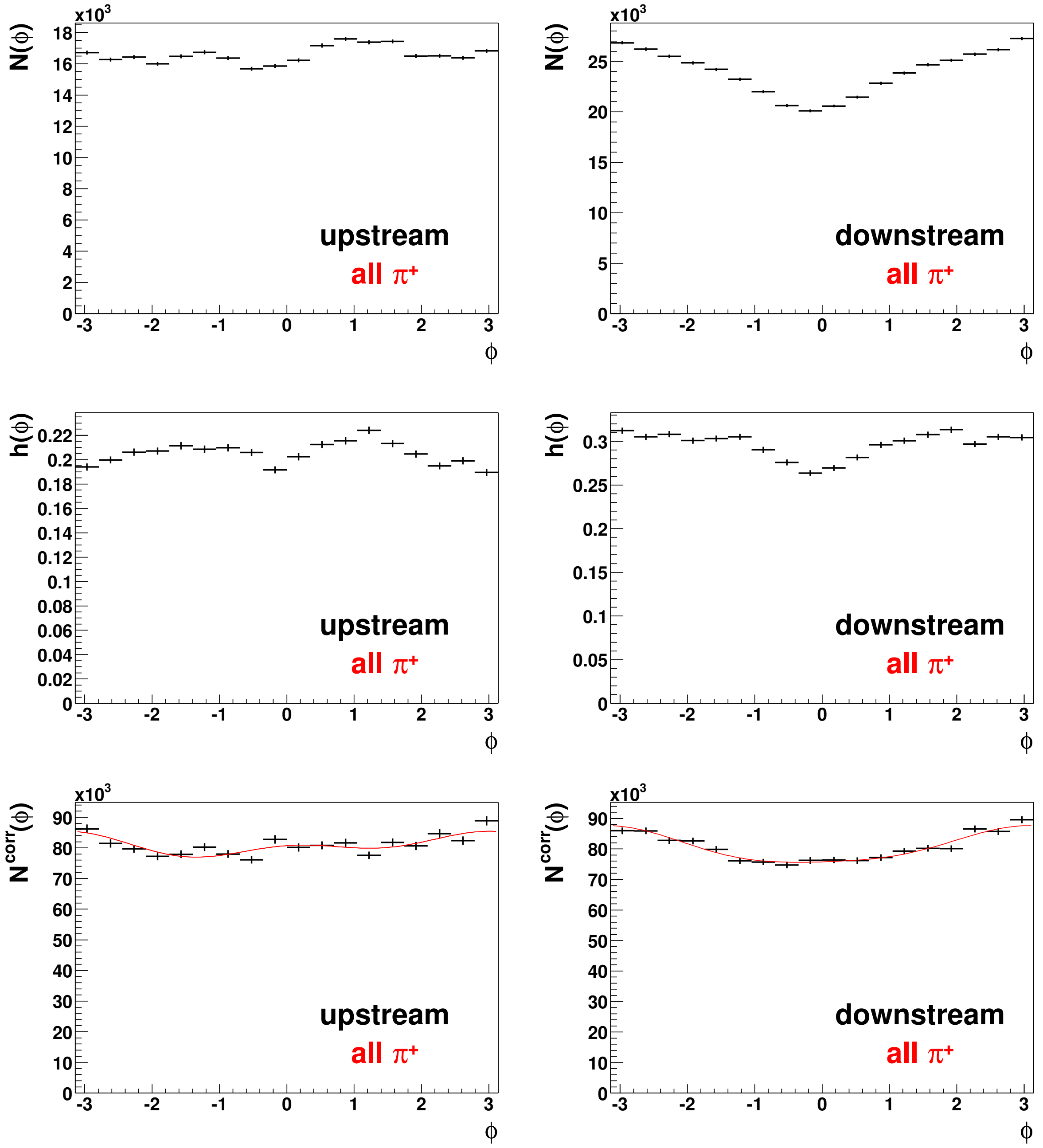

Figure 4.10: Top to bottom: Raw ϕ-distributions, acceptance functions $h(\phi)$ and corrected count rates for positively charged hadrons from the *all hadron* sample. Left: Upstream target cell. Right: Downstream target cell.

the downstream cell. Also the ϕ-dependence of h is stronger in the upstream than in the downstream cell. A slight difference in the overall acceptance between positively and negatively charged hadrons can be observed, which is strongest at small z. On average the probability for reconstructing a positively charged particle is somewhat higher than for a negatively charged one. This is due to the fact that particles of different charge are deflected to opposite directions in the field of the spectrometer magnets. Hence they are tracked in different regions of the spectrometer, which is designed asymmetrically because of the deflection of the positively charged muon beam in the field of the spectrometer magnets.

	all hadrons	**leading hadrons**
upstream / π^+	0.20	0.31
downstream / π^+	0.30	0.42
upstream / π^-	0.19	0.31
downstream / π^-	0.28	0.42

Table 4.3: Overall acceptances of the spectrometer.

Furthermore, the overall acceptance depends strongly on the kinematic range in which it is measured. The strongest one is the dependence on z, which is shown in Figure 4.11 (upper left). Here the overall acceptance ranges between about 0.1 (low z) and 0.35 (high z) for the upstream and between 0.15 and 0.5 for the downstream target cell. The dependence on x_F is similar due to the strong correlation with z. As a function of p_T, the acceptance rises with increasing transverse momentum. The Q^2-dependence is very weak while with increasing x there is a decrease of the acceptance. Between $0.1 < y < 0.3$ the acceptance increases but then slightly decreases again (see Fig. 4.11, upper right).

The influence of the acceptance correction on the ϕ-distributions of the data is estimated by extracting the moments of $h(\phi)$ like it is done with the corrected data (see Sec. 4.2.5 on Pg. 44 ff.). The results for the fits to the overall acceptances are listed in Tab. 4.2.4. The overall $\cos\phi$ and $\cos 2\phi$-moments are mostly negative. Both are on the same order of magnitude with the minimum values being about -0.03 for the sample of all hadrons and -0.05 for the leading hadrons. The $\sin\phi$-moment of the detector acceptance is always compatible with zero. As an example for the kinematic dependence of $h(\phi)$ the results of this procedure are shown as functions of x and y in Fig. 4.11 (middle and lower row). As a function of these variables, $\langle\cos\phi\rangle$ and $\langle\cos 2\phi\rangle$ both are on the same order of magnitude and take values ranging between -0.12 and +0.2. For leading hadrons the overall modulation is somewhat stronger than for the *all hadron* sample, while the variation between the kinematic bins is lower. The strongest ϕ-dependence of the acceptance function can be observed in bins of y and x (see Fig. 4.12 as an example).

For a reasonable Monte Carlo correction it is necessary that the simulation describes the data correctly. This can be tested e.g. by comparing distributions of kinematic variables for these two samples. The corresponding distributions are shown in Fig. 4.13. Presently

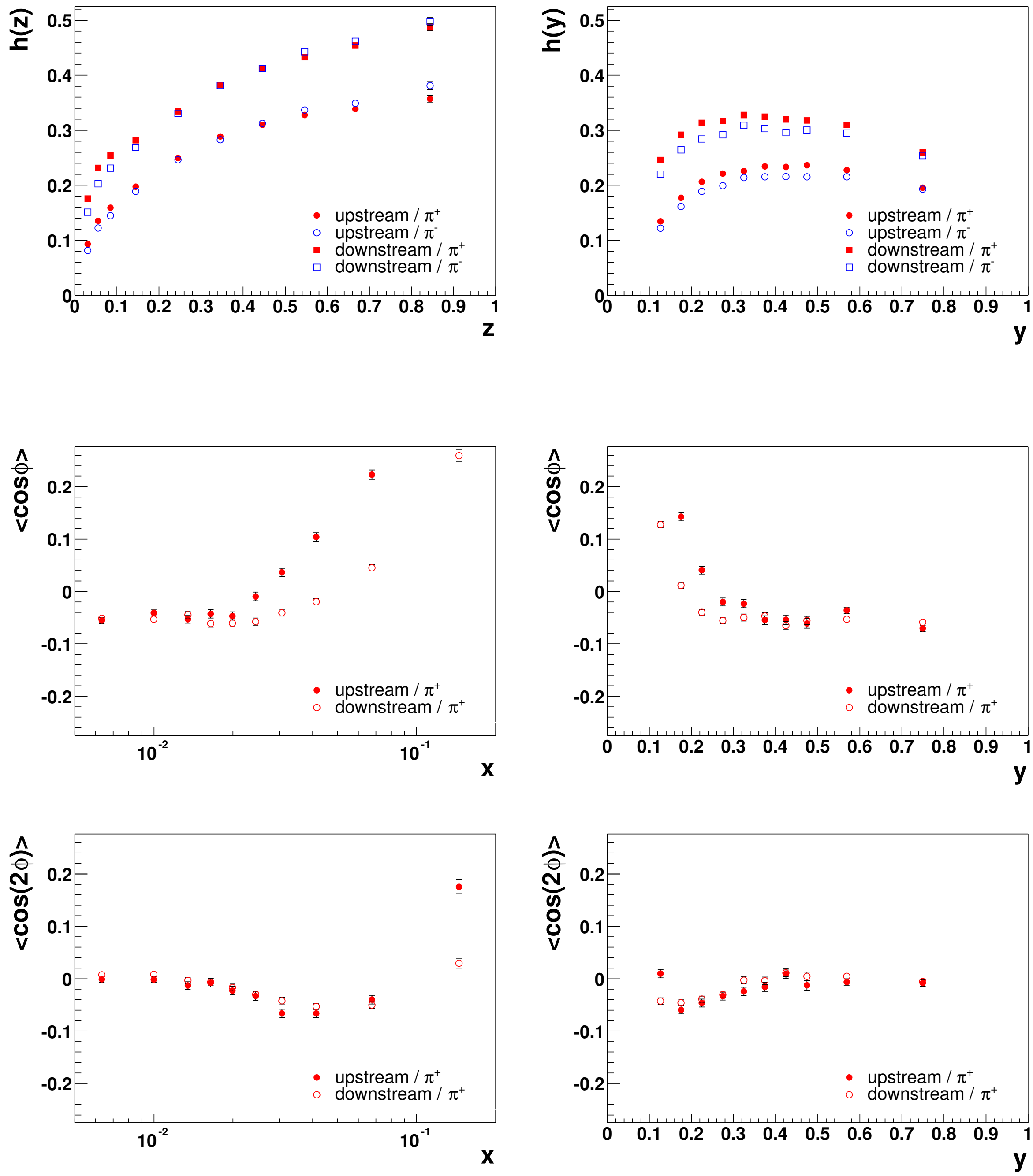

Figure 4.11: Upper row: Left: z-dependence of the overall acceptance h (*all hadron* sample). Right: dependence on y. Note that some of the error bars are too small to be shown. **Middle and lower row:** Dependencies of $\langle \cos\phi \rangle$ and $\langle \cos 2\phi \rangle$ of the acceptance function on the variables x (left) and y (right). All values are derived from the full Monte Carlo sample for the correction of the *all hadron* data sample.

		all π^+	all π^-	leading π^+	leading π^-
$\langle\cos\phi\rangle$	up down	$+0.013 \pm 0.002$ -0.027 ± 0.002	-0.004 ± 0.003 -0.034 ± 0.002	-0.021 ± 0.004 -0.053 ± 0.004	-0.022 ± 0.005 -0.050 ± 0.004
$\langle\cos 2\phi\rangle$	up down	-0.021 ± 0.002 -0.017 ± 0.002	-0.021 ± 0.003 -0.020 ± 0.002	-0.046 ± 0.004 -0.034 ± 0.004	-0.037 ± 0.005 -0.034 ± 0.004
$\langle\sin\phi\rangle$	up down	$+0.003 \pm 0.002$ $+0.002 \pm 0.002$	-0.004 ± 0.003 -0.003 ± 0.002	$+0.003 \pm 0.004$ -0.003 ± 0.004	$+0.005 \pm 0.005$ $+0.005 \pm 0.004$

Table 4.4: Overall Moments of the acceptance function $h(\phi)$. "Leading" refers to the Monte Carlo sample with an extra cut on $z > 0.3$.

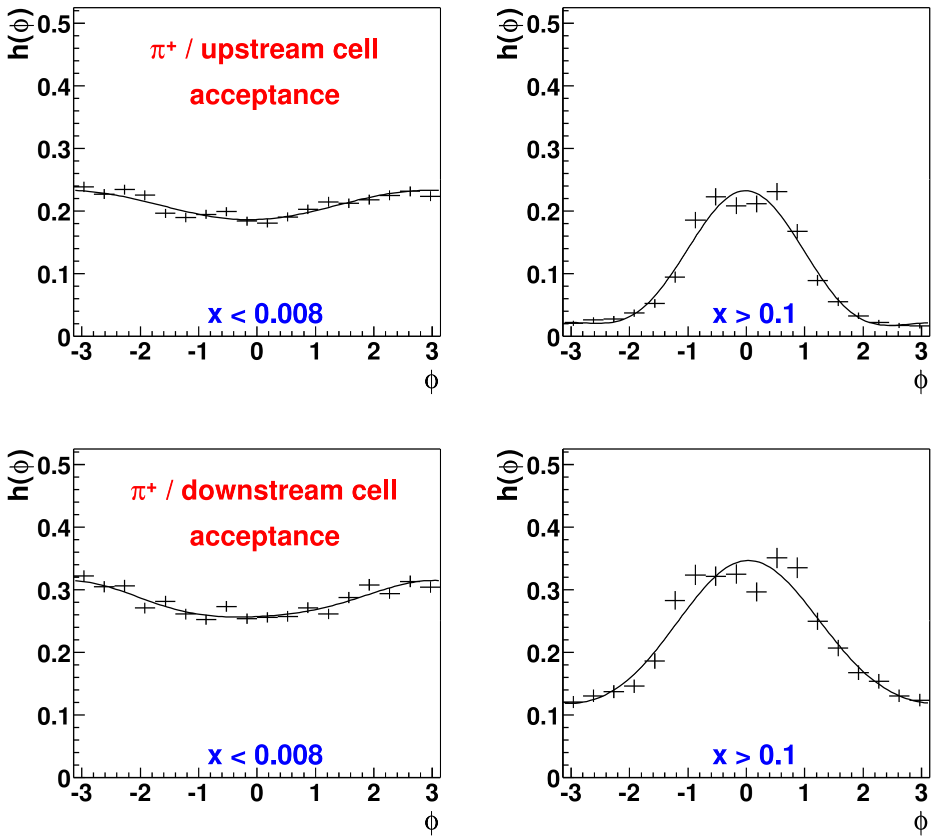

Figure 4.12: ϕ - dependence of the acceptance in the lowest and largest bins of x. Upper row: tracks from events with the primary vertex in the upstream target cell; Lower row: downstream cell. The distributions shown contain the positively charged Monte Carlo tracks for the correction of the *all hadron* sample.

there is a non-negligible disagreement between Monte Carlo and data. This leads to errors which are estimated in Sec. 4.4.1.

Acceptance Correction for Leading Hadrons

The acceptance correction for leading hadrons is performed using the same Monte Carlo samples as for the correction of the *all hadron* data sample. The only additional cut on these samples compared to the analysis of the *all hadrons* sample is the cut on $z > 0.3$ (see Sec. 4.2.3). Performing a selection of leading hadrons on the Monte Carlo samples would be problematic: it could happen that tracks from two *different* particles would pass the identifying criteria in generated and reconstructed Monte Carlo. This will e.g. be the case if the real leading hadron is identified in the generated sample, while in the reconstructed sample another hadron is falsely identified as leading, which happens in about 10% of all events (see Sec. 4.2.3). In consequence the tracks of the reconstructed sample would not be a sub-sample of the generated tracks which is necessary to obtain a reasonable detection probability.

Dispensing with the leading hadron selection in the Monte Carlo is possible since the probability for a particle of given properties to be detected is independent of whether it is leading or not. However, the probability of detection depends on the kinematics of the event the hadron is derived from. Hence in case of the leading hadrons, one needs not only to ensure good agreement of the kinematic variables of the real data sample and the reconstructed Monte Carlo sample in order to exclude systematic errors from insufficient description of the Monte Carlo simulation, but also in order to account for the different hadron multiplicities in the two samples. Since the cut on z reduces the multiplicity to a value close to 1 (see Tab. 4.1, Pg. 33), only small deviation is expected due to this treatment. The corresponding distributions are shown in Fig. 4.14, while Fig. 4.15 shows an example for the correction of the leading hadron distributions.

4.2.5 Calculation of the Moments

From each of the corrected ϕ distributions the moments are determined by fitting a function of the form

$$f(\phi) = A + B\cos\phi + C\cos 2\phi + D\sin\phi \tag{4.12}$$

where the $\sin\phi$ contribution describes the influence of the beam spin. The fits are of reasonable quality as one can see from the distributions of the reduced χ^2_r and the probability which are shown in Figure 4.16. The χ^2_r of all 240 fits (all combinations of binning in the kinematic variables, hadron charges and target cells) entered these histograms. For the *all hadron* sample there is a slight shift in the χ^2_r distribution with respect to the expected distribution. This excess at high χ^2_r corresponds to the excess which can be observed at low probabilities. This indicates that maybe there are higher moments in $\cos(n\phi)$ and $\sin(n\phi)$ which have not been taken into account. A possible source of such higher moments might be higher order contributions to the cross section [MT96]. However, the $\cos(n\phi)$ and

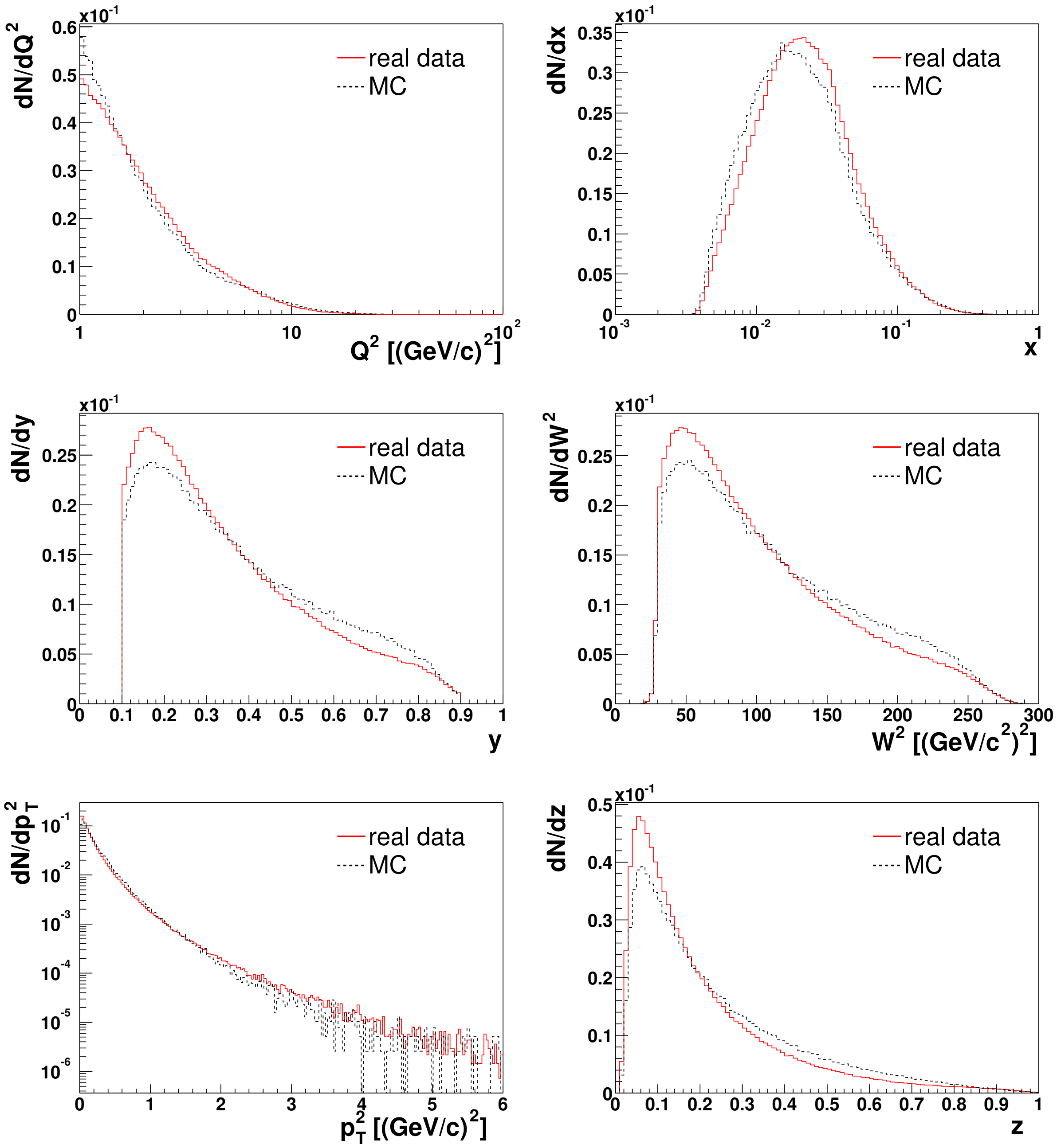

Figure 4.13: Comparison of the distribution of several kinematic variables in real data (full line) and Monte Carlo (dashed line). From upper left to lower right: momentum transfer Q^2; the Bjørken scaling variable x; fractional energy loss y of the lepton; invariant mass W^2 of the proton γ^* system; squared transverse hadron momentum p_T^2; fractional energy transfer z to the hadron (all cuts applied). For the distributions of the inclusive variables (upper and middle row) the entry of each event is weighted with the hadron multiplicity in order to account for the difference in these multiplicities in the data and the Monte Carlo simulation.

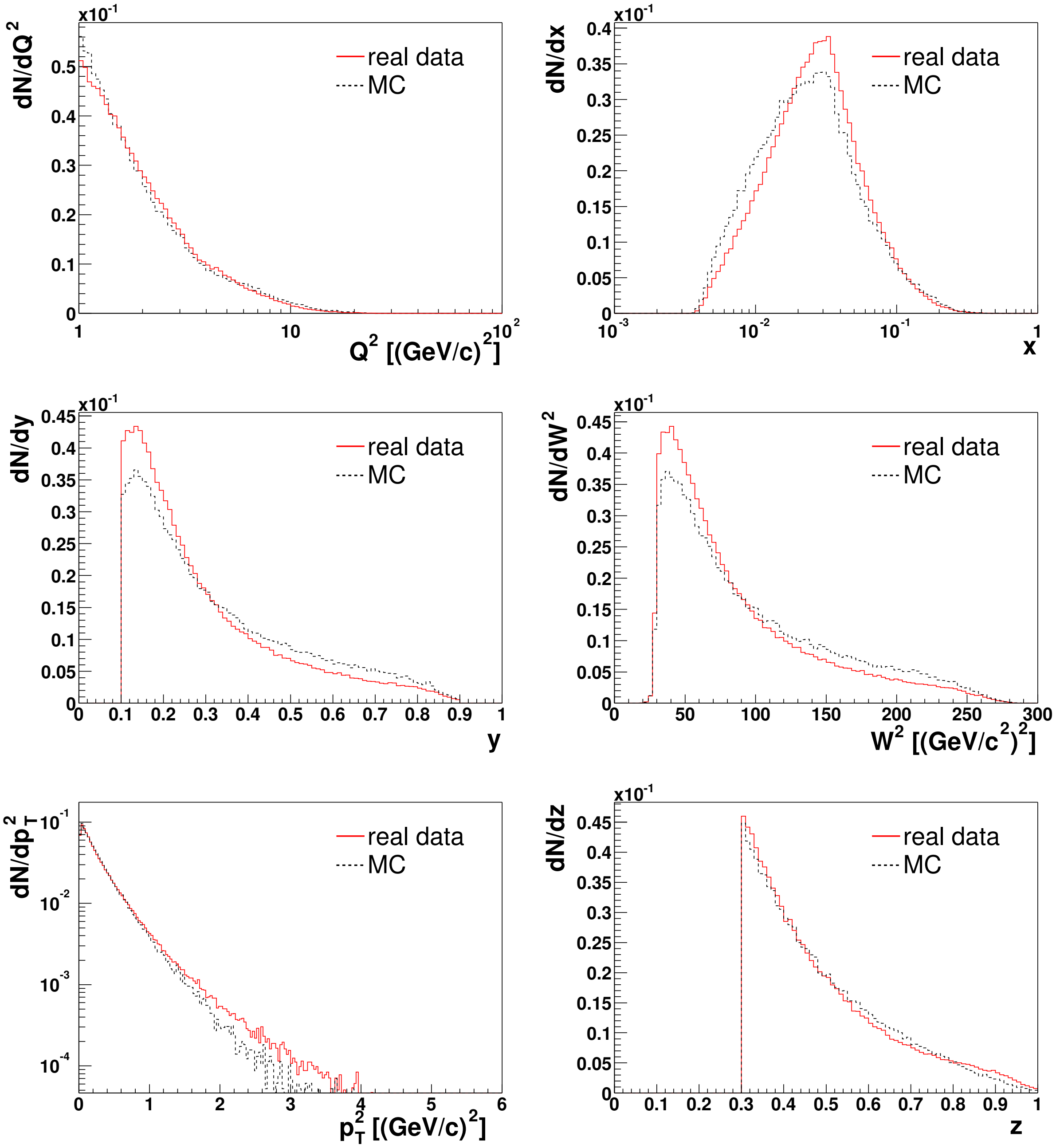

Figure 4.14: The same as in Fig. 4.13 for the sample of leading hadrons (full line) and the Monte Carlo sample for the correction of this sample (dashed line).

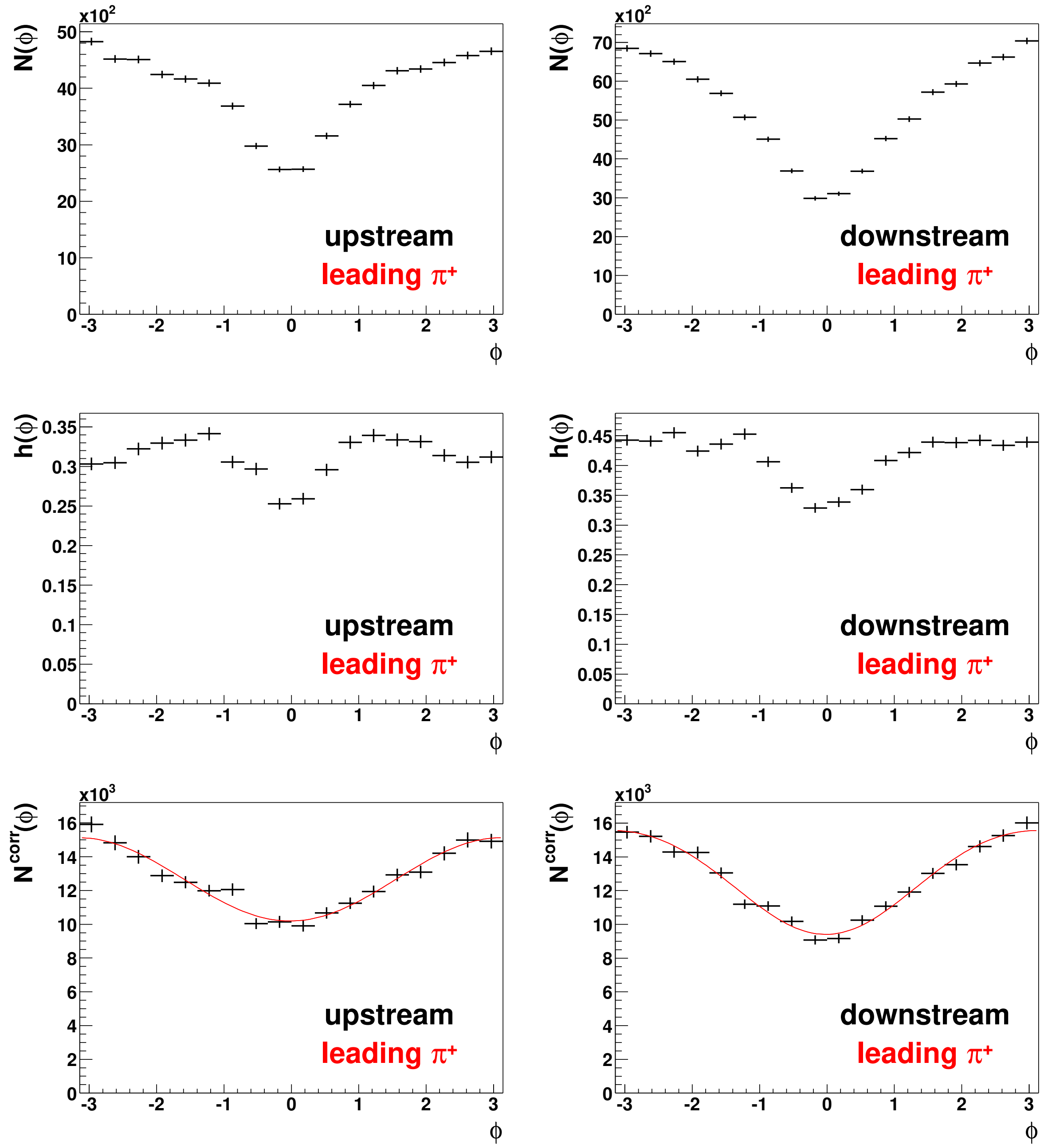

Figure 4.15: Top to bottom: Raw ϕ-distributions, acceptance functions $h(\phi)$ and corrected count rates for positively charged hadrons from the upstream (left) and downstream target cell (right) for the leading hadron sample. The source of the difference of the acceptances compared to the sample of all hadrons (Fig. 4.10) is the cut on $z > 0.3$.

$\sin(n\phi)$ are a set of orthogonal functions, hence ignoring these higher moments should not influence the fit parameters obtained for the interesting moments. If one considers only the 40 fits which correspond to the binning in one kinematic variable, the χ_r^2 for the fits to the bins in z and x_F stand out to be worse than the χ_r^2 for the other dependencies. For leading hadrons the fits seem to be better than for all hadrons.

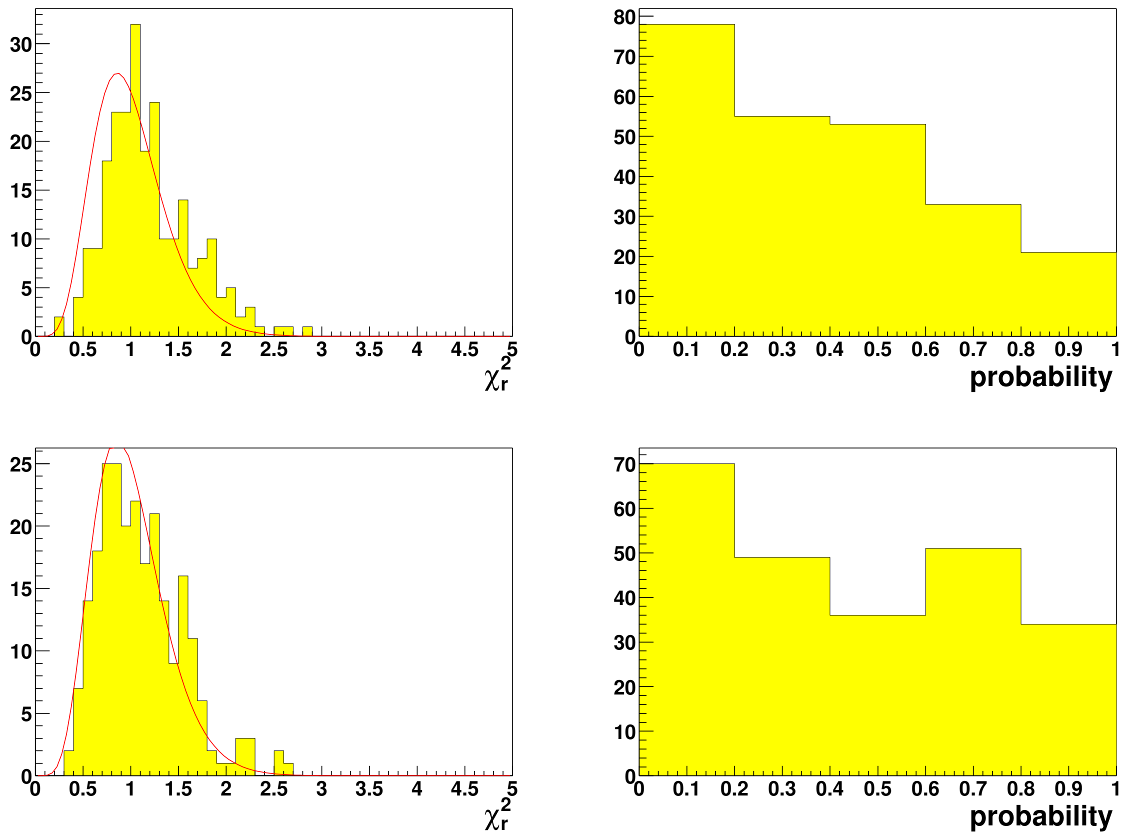

Figure 4.16: Distributions of χ_r^2 (left) and probabilities (right) of the 240 fits to the *all hadron* distributions (upper row) and the leading hadrons sample (lower row). The curves show the expected χ_r^2-distributions.

From the parameters A, B and C one can derive the moments according to Eq. 3.31 (see Page 21):

$$\langle \cos\phi \rangle = \frac{B}{2A} \qquad \langle \cos 2\phi \rangle = \frac{C}{2A}\,. \tag{4.13}$$

The y-dependence as predicted by Cahn can be removed from these values by dividing each by $\langle f_1(y) \rangle$ or $\langle f_2(y) \rangle$, respectively (see Eq. 3.34, Pg. 21). The average values of $f_i(y)$ are calculated separately for the two cells and charges by weighting each event with the number of hadrons which enter into the analysis (see Fig. 4.17).

Finally the moments for the two target cells are combined by calculating the weighted average. As one can see in Figure 4.18 there is agreement within the errors between the

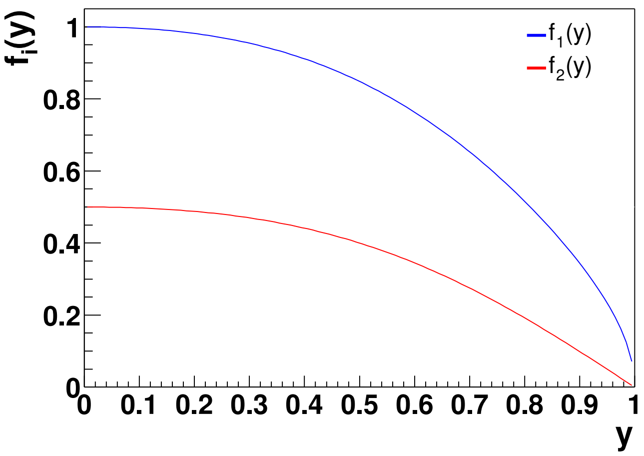

Figure 4.17: y-dependence of $\langle \cos\phi \rangle$ and $\langle \cos 2\phi \rangle$ according to Equations 3.34 and 3.35 (see Pg. 21).

overall results for the two cells, except for $\langle \cos\phi \rangle / \langle f_1(y) \rangle$ in the case of positive hadrons. Furthermore, both moments are systematically larger for the downstream cell than for the upstream cell. This behaviour can be observed for the sample of all hadrons as well as for the sub-sample of leading hadrons. It also shows up in case the moments are calculated as a function of the kinematic variables, but not as strong as in the result for the overall distribution. The reason for this behaviour probably is the dependence of the asymmetry on the kinematic variables and the different acceptance of the two target cells in these variables. The distributions of y and x, where these deviations are strongest, are compared in Fig. 4.19 (see also Tabs. B.12 and B.13 in the appendix). In the Monte Carlo the same behaviour can be observed. Differences in the values extracted from the data of the two cells are therefore expected.

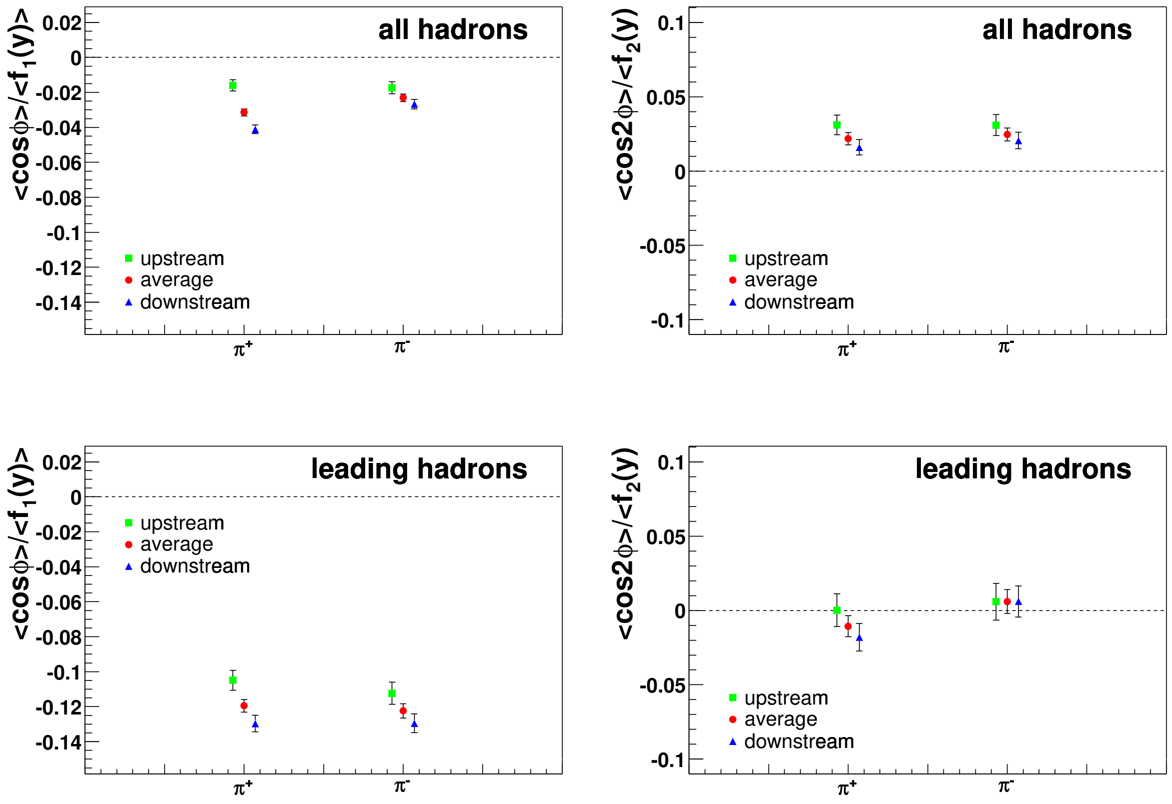

Figure 4.18: Comparison of the overall $\langle \cos\phi\rangle/\langle f_1(y)\rangle$ (left) and $\langle \cos 2\phi\rangle/\langle f_2(y)\rangle$ (right) from the two target cells. The upper row shows the results from the *all hadron* sample while the lower row shows the results for leading hadrons. The systematic differences in the results for the two target cells can, at least partly, be attributed to the different acceptance of the two target cells. Thus the difference in the values mirrors the kinematic dependence of the moments.

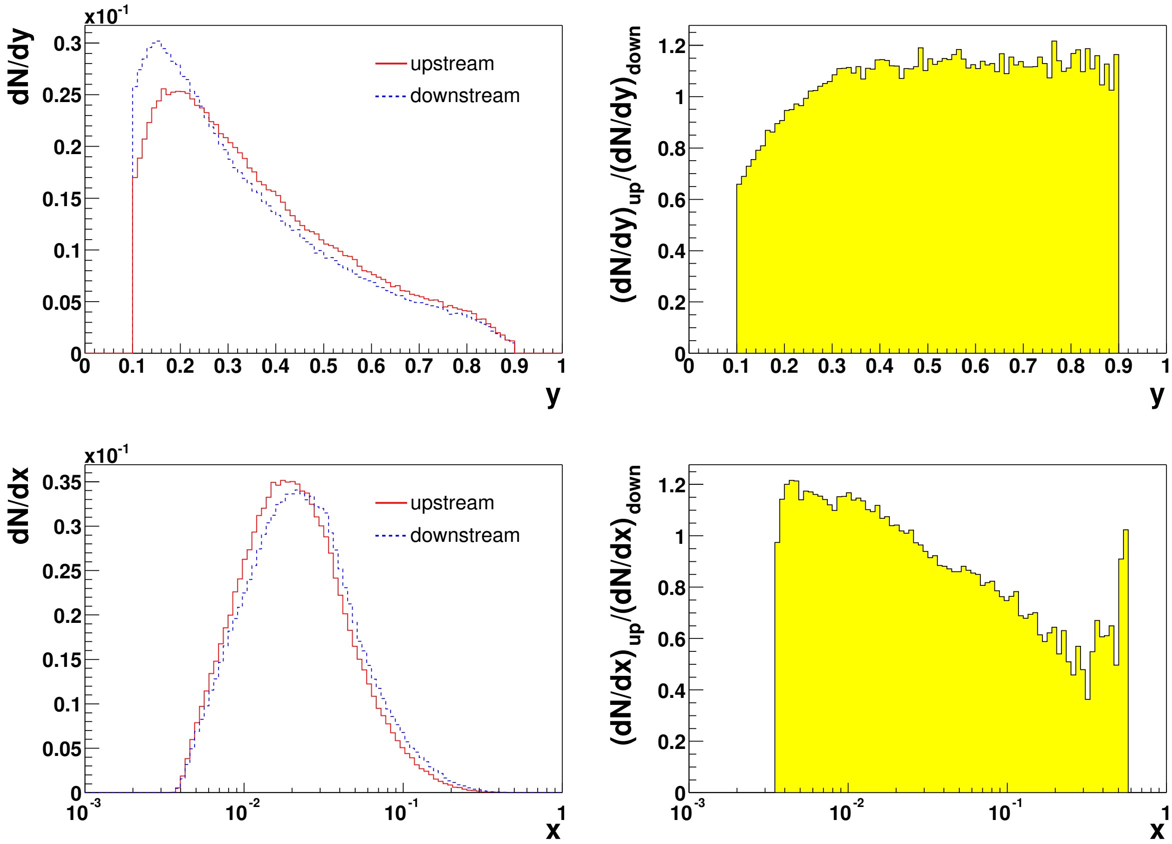

Figure 4.19: Comparison of the distributions of the kinematic variables y (upper row) and x (lower row) in the two target cells (*all hadron* sample). On the left the distributions for the two cells are shown. Both are normalised to the number of entries. On the right the ratios of the two distributions (up/down) are shown.

4.3 Results

The results shown in the following are $\langle\cos\phi\rangle/\langle f_1(y)\rangle$ and $\langle\cos 2\phi\rangle/\langle f_2(y)\rangle$, i.e. moments weighted with the average y-dependence as predicted by Cahn (c.f. Eq. 3.34). Within this chapter the term "moment" always refers to these weighted moments. A discussion of the results in terms of the theoretical expectation lined out in Chap. 3.2 will be given in Chap. 5. The numbers which correspond to the data points in the plots below can be found in Appendix B.4 (Pages 99 ff.). Only statistical errors are given in this section. For a discussion of the magnitude of systematic errors see the following Sec. 4.4.

The overall results obtained for the $\cos\phi$- and $\cos 2\phi$-moments are listed in Tab. 4.5. The values of the $\cos\phi$-moments from the samples of all π^+ and all π^- are significantly negative and differ from each other with the moment being more pronounced for π^+ than for π^-. The values of the $\cos 2\phi$-moments agree within the statistical errors. The order of magnitude of the $\cos 2\phi$-dependence is about the same as for the $\cos\phi$-dependence with a positive sign of the $\cos 2\phi$-moments. The absolute errors are larger for the $\cos 2\phi$-moment than for the $\cos\phi$-moment because the value of $\langle f_2(y)\rangle$ it is weighted with is about half of the corresponding value of $\langle f_1(y)\rangle$. The observed $\cos\phi$-asymmetry is much larger for the samples of leading hadrons which are sampled on average with much larger $\langle z\rangle$ (see Tab. B.12 and B.13 in App. B.3) than the *all hadron* samples. For the leading hadrons the results of the $\cos\phi$-moment agree within the errors. The results for the $\cos 2\phi$-moment differ for the two charges. While for π^- this moment is compatible with zero with a tendency to positive values, a slightly negative value is observed for the π^+. In the following the results from the analysis, binned in kinematic variables, are shown.

	π^+		π^-	
	$\langle\cos\phi\rangle/\langle f_1(y)\rangle$	$\langle f_1(y)\rangle$	$\langle\cos\phi\rangle/\langle f_1(y)\rangle$	$\langle f_1(y)\rangle$
all hadrons	-0.031 ± 0.002	0.889	-0.023 ± 0.002	0.885
leading	-0.120 ± 0.004	0.932	-0.122 ± 0.004	0.924
	$\langle\cos 2\phi\rangle/\langle f_2(y)\rangle$	$\langle f_2(y)\rangle$	$\langle\cos 2\phi\rangle/\langle f_2(y)\rangle$	$\langle f_2(y)\rangle$
all hadrons	$+0.022 \pm 0.004$	0.428	$+0.025 \pm 0.004$	0.425
leading	-0.011 ± 0.007	0.455	$+0.006 \pm 0.008$	0.450

Table 4.5: Overall $\langle\cos\phi\rangle/\langle f_1(y)\rangle$ and $\langle\cos 2\phi\rangle/\langle f_2(y)\rangle$; Left: π^+, right: π^-

y-dependence

Since the results shown in Fig. 4.21 are moments corrected for the y-dependence as predicted by Cahn, one expects no dependence on this variable. However, a strong modulation can be observed. Probably this dependence partly results from some correlation of y and some other kinematic variable. For example there is a strong connection with z. Small values of y favour large values of z, since the γ^* energy is not sufficient to produce a final state with high multiplicity. Thus there can still be some hidden dependence on y, since binning in y means to some extent binning in z. While for the leading hadron sample π^+ and π^- match each other except for some data points, for the *all hadron* sample they do not. At low y the result for all positive hadrons is flat, while for negative hadrons starting with positive values it decreases to negative values. For leading hadrons all values are negative and show a minimum at values between 0.3 and 0.4. The values of the $\cos 2\phi$-moment fluctuate very much, especially for the leading hadrons. For the π^- from the *all hadron* sample the $\cos\phi$-moment takes rather high values of the order of 0.1 at low y and drops if y increases.

Q^2-dependence

There is almost no dependence on Q^2 (see Fig. 4.22), neither in the $\cos\phi$-moment, which is expected to slope like $1/Q$, nor in the $\cos 2\phi$-moment for which a $1/Q^2$-dependence is predicted. Both moments are flat and of about the same order of magnitude for the *all hadron* sample. For the leading hadrons the $\cos\phi$-moment is strongly negative while the $\cos 2\phi$-moment is compatible with zero.

x-dependence

The $\cos\phi$-moment (see Fig. 4.23) extracted from the sample of all hadrons shows almost no dependence on x. For the sample of π^+ it is flat over the whole range of x, while for the π^- at values of $x > 0.03$ rises up to positive values of the $\cos\phi$-moment. Below $x = 0.03$ the values for these two particle types agree with each other. For the leading hadron sample a strong dip in the x-dependence can be observed with the minimum value of -0.17 being reached at about $x = 0.02$. All values are negative but π^+ and π^- are still not compatible at high x. The $\cos 2\phi$-moment, which is significantly positive at least for the *all hadron* sample, shows no x-dependence for all hadrons. The $\cos 2\phi$-moment of the leading hadrons varies much more due to the lower statistics.

p_T-dependence

The dependence on p_T is shown in Fig. 4.24. At high p_T a clear negative signal can be observed for the *all hadron* sample. Going to lower values of p_T, the magnitude of the effect decreases and vanishes at about $p_T = 0.3\,\mathrm{GeV}/c$. Below this value $\langle\cos\phi\rangle$ is positive and the values for π^+ and π^- differ. For the leading hadrons the p_T-dependence of the $\cos\phi$-moment reveals a minimum at $p_T \approx 0.4\,\mathrm{GeV}/c$. The $\cos 2\phi$-moment is flat and positive for the *all hadron* sample, while for the leading hadron sample it shows strong fluctuations around zero.

z- and x_F-dependences

Because there is a strong correlation between x_F and z (see Fig. 4.20), the dependencies on these two variables, which are shown in Figures 4.25 and 4.26 resemble each other very much. In the last four bins, which cover the same ranges of z for leading and all hadrons, the results for these two samples are equal. This has to be expected since above $z > 0.5$ the *all hadron* sample contains only leading hadrons.

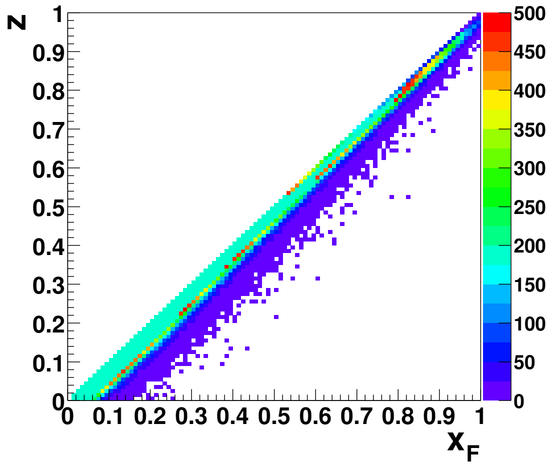

Figure 4.20: Correlation of the hadronic kinematic variables x_F and z (For all hadrons; The maximum number of entries per bin is set to 500.)

The highest z data point shows a large difference between π^+ and π^-: While the π^- behave smooth, the π^+ value in the last bin seems to be much too high. The same can be observed in the $\cos 2\phi$-moment. Probably this is still due to a contamination of the hadron sample by muons (see Sec. 4.4.2, Pg. 68 ff.). Additional uncertainty is introduced to the result in the last bin by the exclusive hadron production which takes place at $z = 1$. In the lowest z- and x_F-bins of the leading hadron sample the points fluctuate strongly.

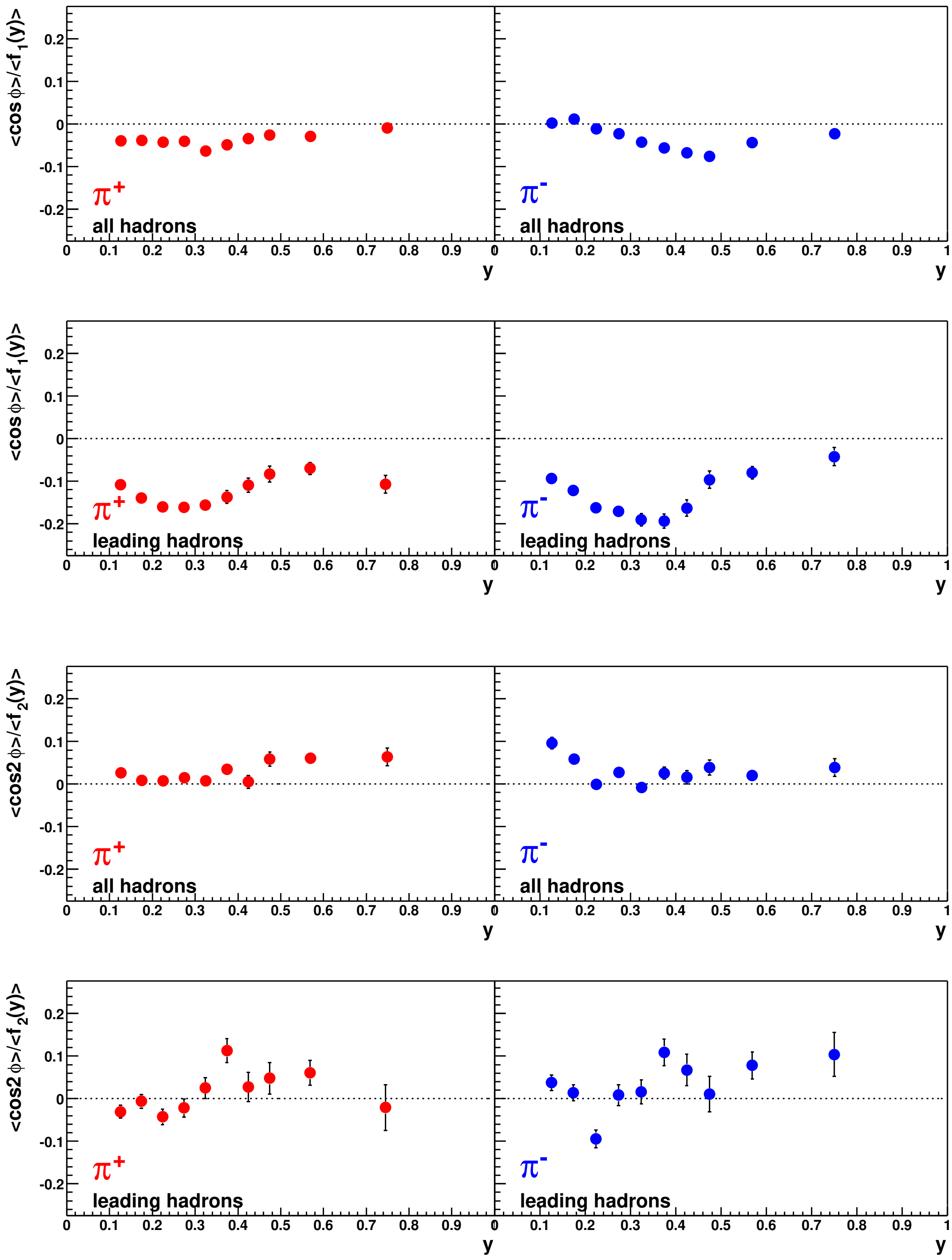

Figure 4.21: Dependence of $\langle \cos\phi \rangle / \langle f_1(y) \rangle$ and $\langle \cos 2\phi \rangle / \langle f_2(y) \rangle$ on y

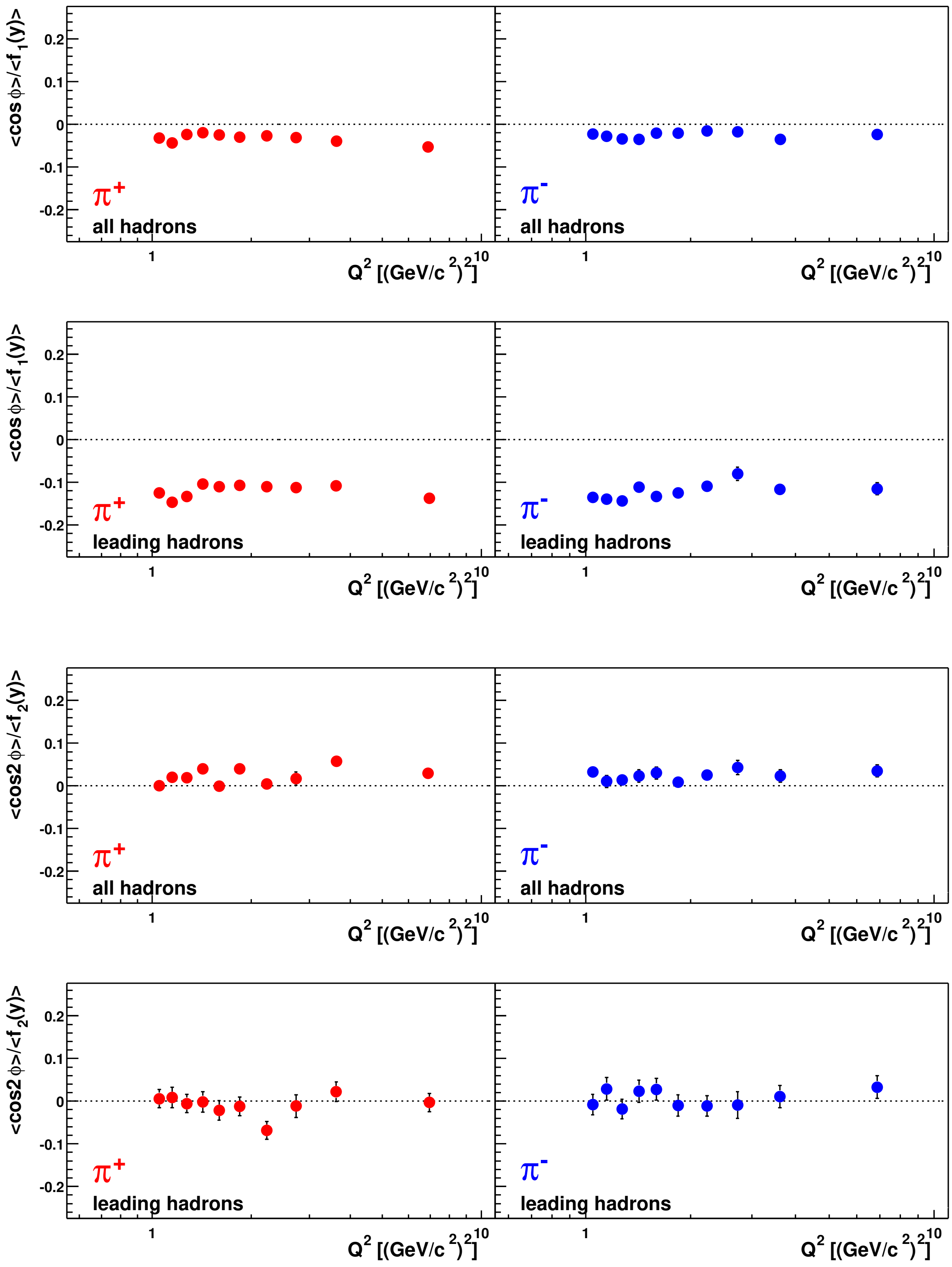

Figure 4.22: Dependence of $\langle \cos\phi \rangle / \langle f_1(y) \rangle$ and $\langle \cos 2\phi \rangle / \langle f_2(y) \rangle$ on Q^2

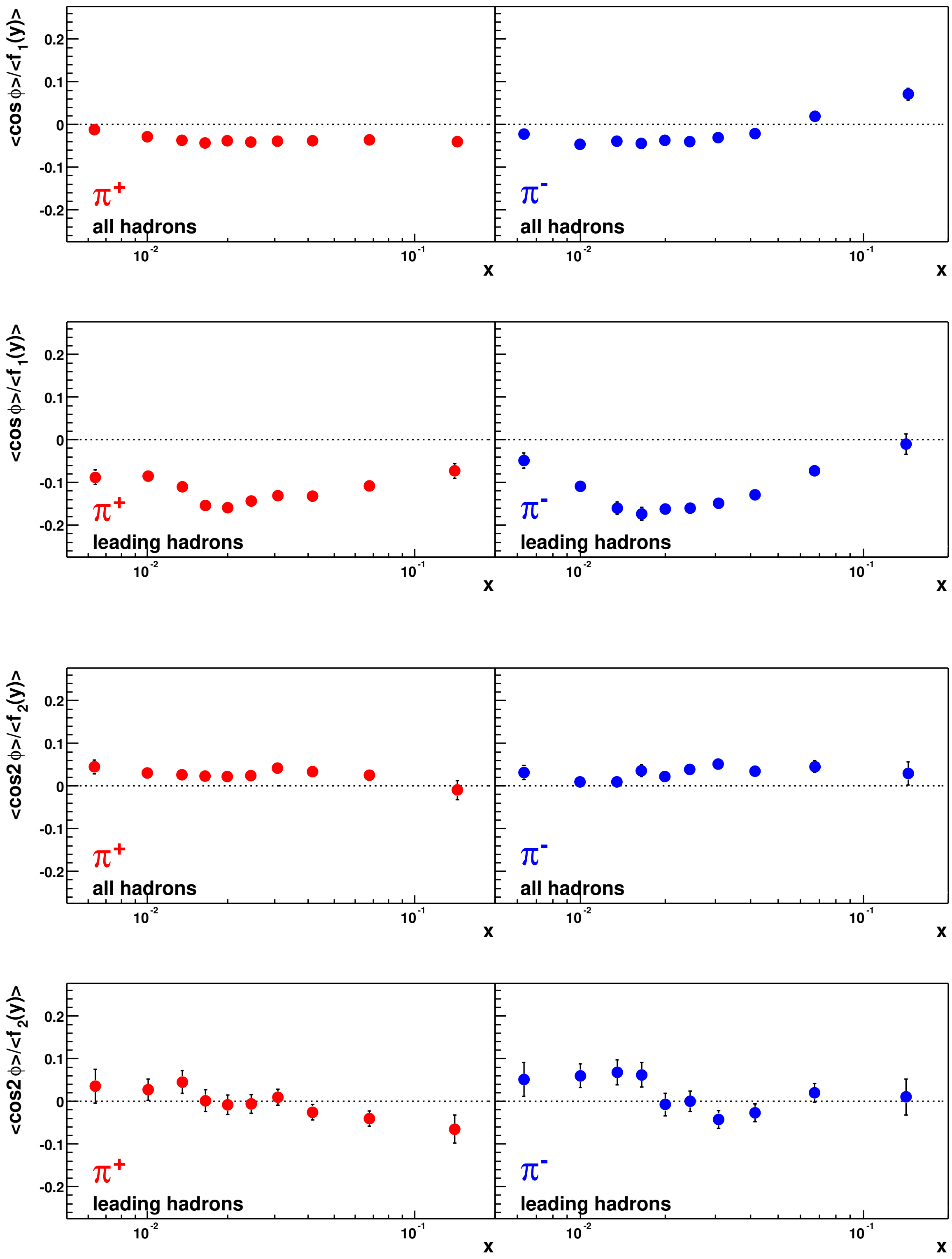

Figure 4.23: Dependence of $\langle \cos\phi \rangle / \langle f_1(y) \rangle$ and $\langle \cos 2\phi \rangle / \langle f_2(y) \rangle$ on x

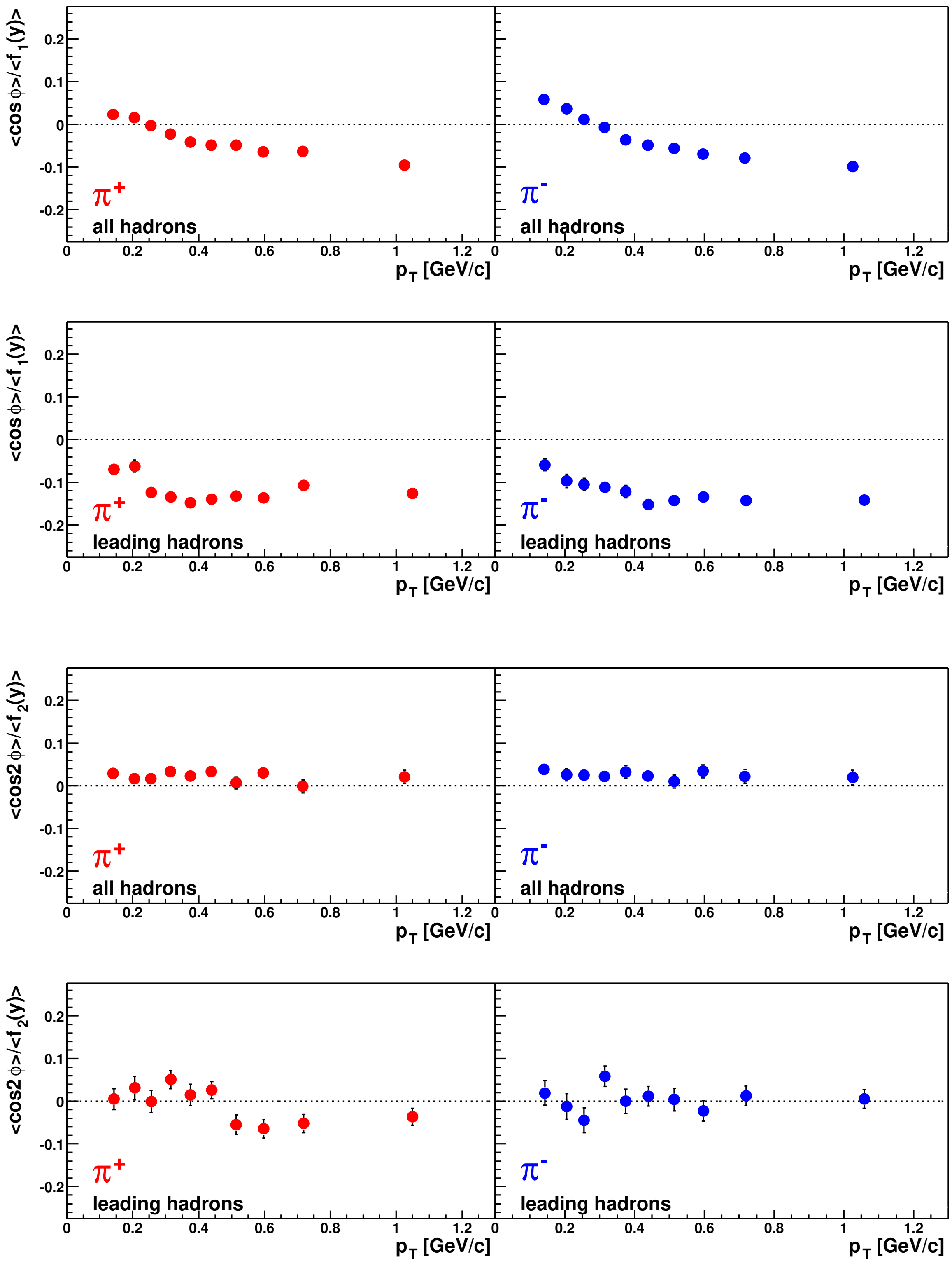

Figure 4.24: Dependence of $\langle \cos\phi \rangle / \langle f_1(y) \rangle$ and $\langle \cos 2\phi \rangle / \langle f_2(y) \rangle$ on p_T

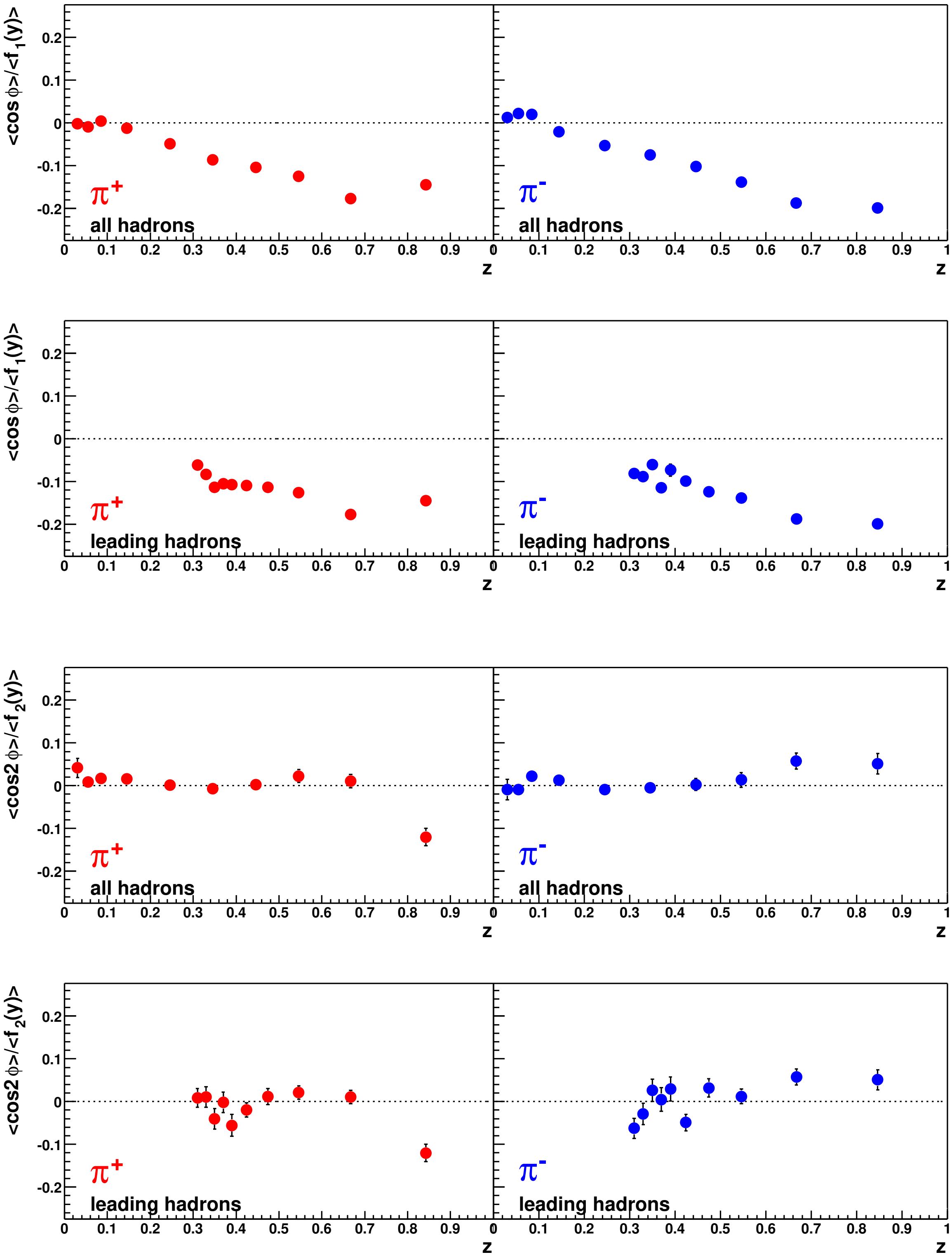

Figure 4.25: Dependence of $\langle \cos\phi \rangle / \langle f_1(y) \rangle$ and $\langle \cos 2\phi \rangle / \langle f_2(y) \rangle$ on z

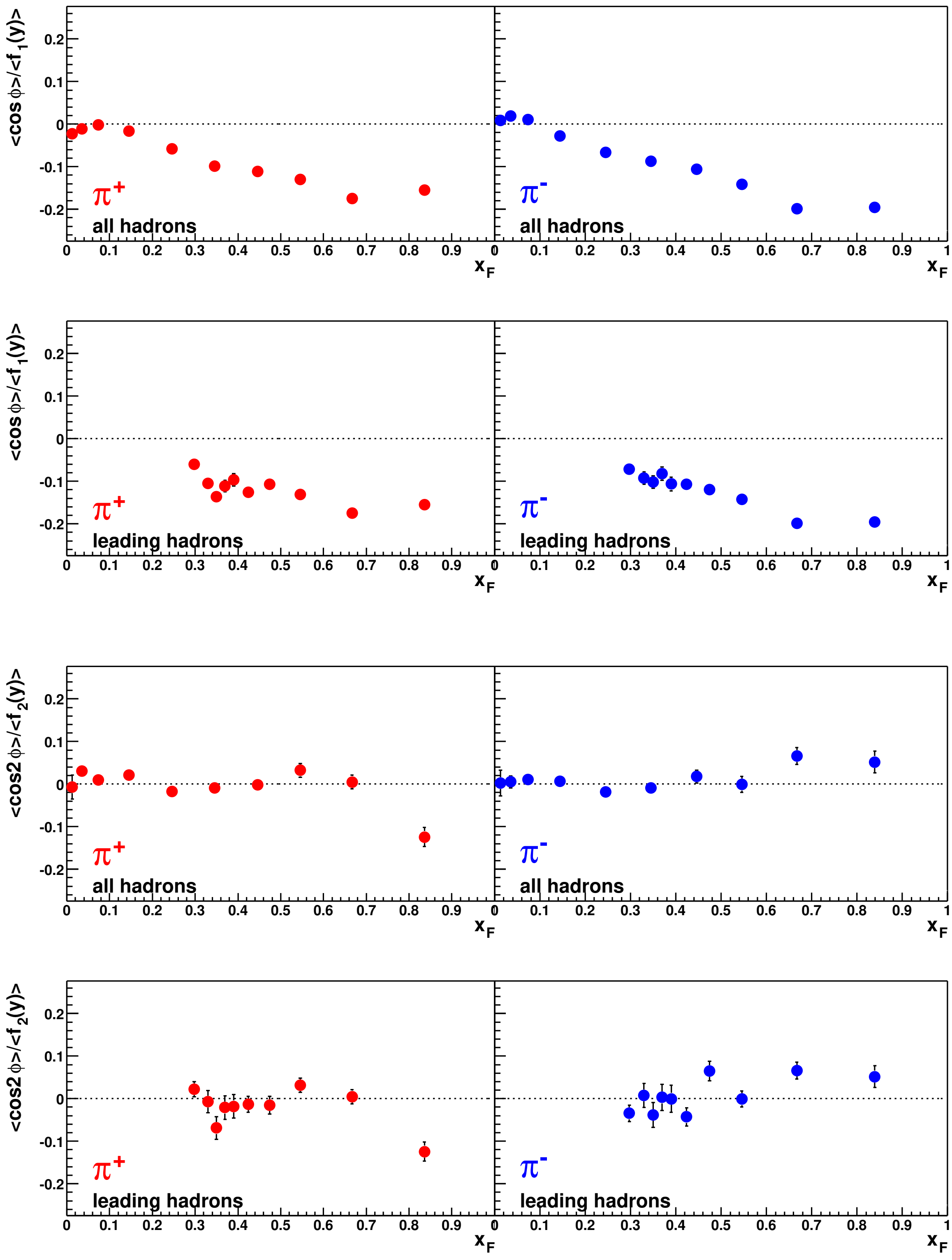

Figure 4.26: Dependence of $\langle\cos\phi\rangle/\langle f_1(y)\rangle$ and $\langle\cos 2\phi\rangle/\langle f_2(y)\rangle$ on x_F

4.4 Errors and Systematics

4.4.1 Systematic Influence of the Monte Carlo Quality

As shown in Sec. 4.2.4 the $\langle \cos\phi \rangle$ of the acceptance function is about the same order of magnitude as the corresponding moment of the corrected *all hadron* sample. The magnitude of the $\cos 2\phi$-moment of the acceptance is even larger than the result from the fit to the corrected data. This means that the influence of the Monte Carlo correction on the result is strong. Therefore it is necessary that the acceptance of the detector is described accurately. During the analysis several sources of systematic errors showed up, whose influence on the final result has to be estimated. Some of them must be ascribed to insufficient description of the reality in the Monte Carlo which is available so far. Mismatches are observed in the distributions of the kinematic variables, the composition of trigger types and the target position.

Attempts are made to correct for this mismatch, but this treatment is problematic: the methods described in the following are all based on the assumption that the differences in the behaviour of the reconstructed Monte Carlo and the real data are due to insufficient reconstruction only. There could be errors in the generated events as well due to insufficient event generation, but these are not taken into account in this case. Furthermore, corrections are applied on single kinematic variables or on the trigger rates but since these depend on each other, improvement in one variable might introduce worsening in some other. Therefore no corrections on the Monte Carlo sample are included in the main analysis. In this section of the thesis the impact of some corrections of single properties on the result are listed. The outcome can be used to estimate a systematic error on the results.

In order to have a measure for the influence of the corrections, each of them is applied to an unbinned sample of all hadrons. The results for the moments from these fits are compared to the moments from the corresponding values obtained without any correction. The result of this procedure will be discussed together with the description of the methods to correct for the mismatches in the following.

Triggers in Data and Monte Carlo

As already seen in Figs. 4.13 and 4.14 (see Secs. 4.2.4 and 4.2.4, Pg. 37 ff.), the distributions of the kinematic variables in the Monte Carlo sample differ from the corresponding distributions in the data. Since the different triggers used in COMPASS directly correspond to the kinematics of the selected events, failures in the description of the triggers in the detector simulation could be the source of this mismatch. Especially, the efficiencies for the various types of triggers must occur in the same ratios in the simulation as they do in reality. This is not fulfilled as one can see in Figure 4.27. Hence, as a first attempt to correct for the mismatch in the kinematic variables, the Monte Carlo samples from the different triggers are re-weighted according to their distribution in the real data.

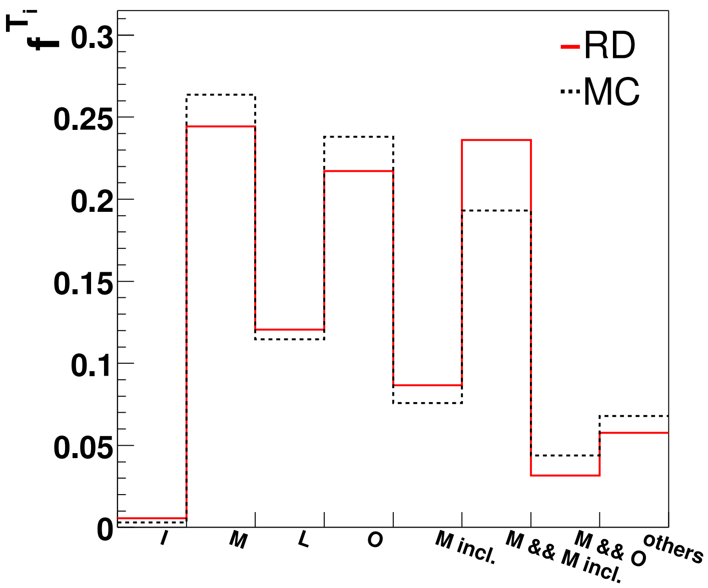

Figure 4.27: Comparison of the fractions of the most frequent types of triggers in P2D data (full line) and Monte Carlo (dashed line). The deviations are significant since the errors are below 0.001. (complete *all hadron* sample)

The basic idea of the correction method applied is to produce a corrected acceptance function $h(\phi)$, where the different triggers are weighted according to the fraction they account for in the real data. For each of the trigger types T_i the reconstructed Monte Carlo ϕ-distribution is determined and a trigger-dependent acceptance function h^{T_i} is calculated according to

$$h^{T_i}(\phi) = \frac{N^{T_i}_{rec}(\phi)}{N_{gen}(\phi)} . \tag{4.14}$$

These distributions are then summed taking into account the different fractions in data and Monte Carlo by weighting them according to

$$h(\phi) = \frac{\sum_{T_i} h^{T_i}(\phi) w_{T_i}}{\frac{1}{N_t} \sum_{T_i} w_{T_i}} . \tag{4.15}$$

The normalisation factor $1/N_t$, with N_t being the number of trigger types that are treated separately, makes sure that Equation 4.15 reduces to the acceptance without the correction of the trigger ratios (Eq. 4.8). With the errors of the weights being negligible and according to Gaussian error propagation the error of this expression is obtained as

$$\delta h(\phi) = \sqrt{\sum_{T_i} \left(\frac{\delta h^{T_i}(\phi) w_{T_i}}{\frac{1}{N_t} \sum_{T_i} w_{T_i}} \right)^2} , \tag{4.16}$$

where the $\delta h^{T_i}(\phi)$ are calculated according to Eq. 4.9. This re-weighted acceptance function is then used to correct the ϕ-distribution of the data, employing Equations 4.10 and 4.11 (see Sec. 4.2.4 on Page 39).

In order to determine the weights w_{T_i}, the fractions of the most frequently occurring types of triggers in the final event samples are compared in real data and in the Monte Carlo simulation. The largest absolute deviations show up in the fractions of the *middle*, *outer* and the combination of *middle and middle inclusive* triggers. Therefore these three are treated separately for the estimation of the influence of the trigger ratios. All other triggers and combinations of triggers are analysed together. The fractions $f_{rec}^{T_i}$ and $f_D^{T_i}$, which are the fractions of trigger type T_i in Monte Carlo and real data respectively, are listed in Table 4.6 together with the corresponding weighting factors. From these the weights are determined according to

$$w_{T_i} = \frac{f_D^{T_i}}{f_{rec}^{T_i}} . \tag{4.17}$$

	f_{rec}^i	f_D^i	w_i
Outer	0.233	0.203	1.193
Middle	0.268	0.225	1.148
Middle & Middle incl.	0.196	0.218	0.903
others	0.302	0.355	0.852

Table 4.6: Weighting factors for the triggers in acceptance correction

By this method it is ensured that at least the ratios of the four trigger types in the Monte Carlo are identical with the ones in the data. It does not ensure that the overall fraction of reconstructed events is described correctly. This means that the procedure provides a correct description of the shape of the ϕ-distributions while the total counting rates are not reconstructed correctly. However, this does not affect the resulting moments, since they are normalised for the total counting rate.

Figure 4.28 shows the influence of the re-weighting on the distributions of the kinematic variables x and y. In case the mismatch between the data and the Monte Carlo distributions is entirely caused by the use of wrong trigger efficiencies in the simulation of the detector, these distributions should be closer to the real distributions than without the correction. Obviously the re-weighting of the trigger ratios causes only negligible changes in the Monte Carlo distributions. Correspondingly, the influence of these corrections to $\langle\cos\phi\rangle/\langle f_1(y)\rangle$ and $\langle\cos 2\phi\rangle/\langle f_2(y)\rangle$ is small. The changes stay below the statistical errors of the results (see the top data points in Fig. 4.29).

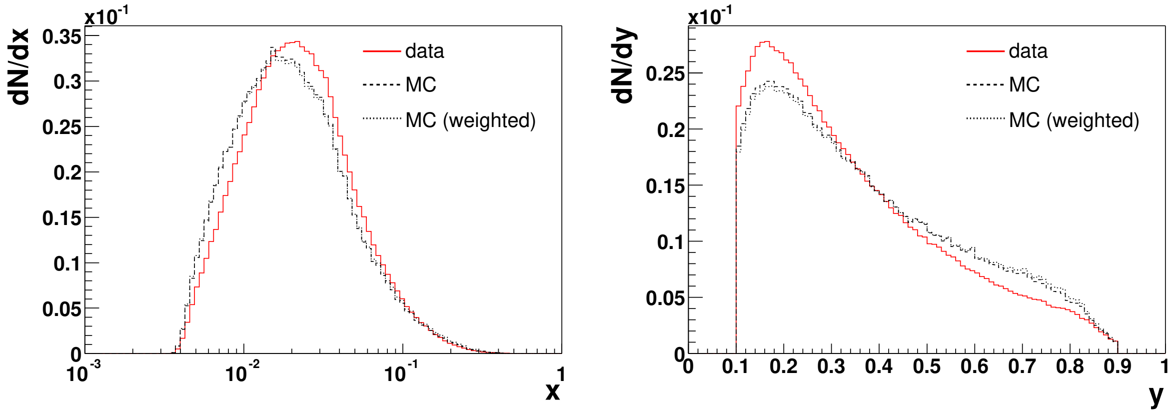

Figure 4.28: Influence of the correction of the trigger type composition in the Monte Carlo sample. Right: Distributions of x for the complete *all hadron* data sample (full line), the raw Monte Carlo sample (dashed line) and the Monte Carlo sample after re-weighting (dotted). Left: The same for the distributions of y.

Correction for Mismatch of Kinematic Variables

As seen in the previous section, the mismatch in the kinematic variables can not be removed by re-weighting the triggers in the Monte Carlo simulation. Thus next the Monte Carlo sample is re-weighted in a way that the agreement between these distributions becomes better, using a set of weighting factors which are extracted from the distributions of the kinematic variables themselves. This is done for z, y and Q^2 exemplarily.

Therefore the full range of a given variable X is subdivided into ten parts as it is done to extract the kinematic dependence (see the tables in the Appendix B.2). The weighting factors w_{X_i} are determined from the distributions of X in the data and Monte Carlo by calculating

$$w_{X_i} = \frac{f_D^{X_i}}{f_{rec}^{X_i}}, \tag{4.18}$$

with f_{rec}^i and f_D^i being the fractions of events in the range X_i compared to the full range of X in Monte Carlo and real data respectively.

Using these weights, in principle the same correction procedure as for the trigger types is applied. For each of the ten kinematic bins acceptance functions are calculated, weighted and combined in an analogous manner to the way described in equations 4.14 and 4.15. Of course the index T_i is now replaced by another index X_i which denotes the kinematic bin in question and the Number of trigger types N_t is replaced by the number of kinematic bins considered. These acceptance functions are used to correct the ϕ-distributions of the real data.

The results are shown in the second to fourth point (from top to bottom) of the plots in Fig. 4.29. Compared to the case of the correction for the trigger ratios, the resulting differences in the moments are much larger. The largest deviation from the uncorrected

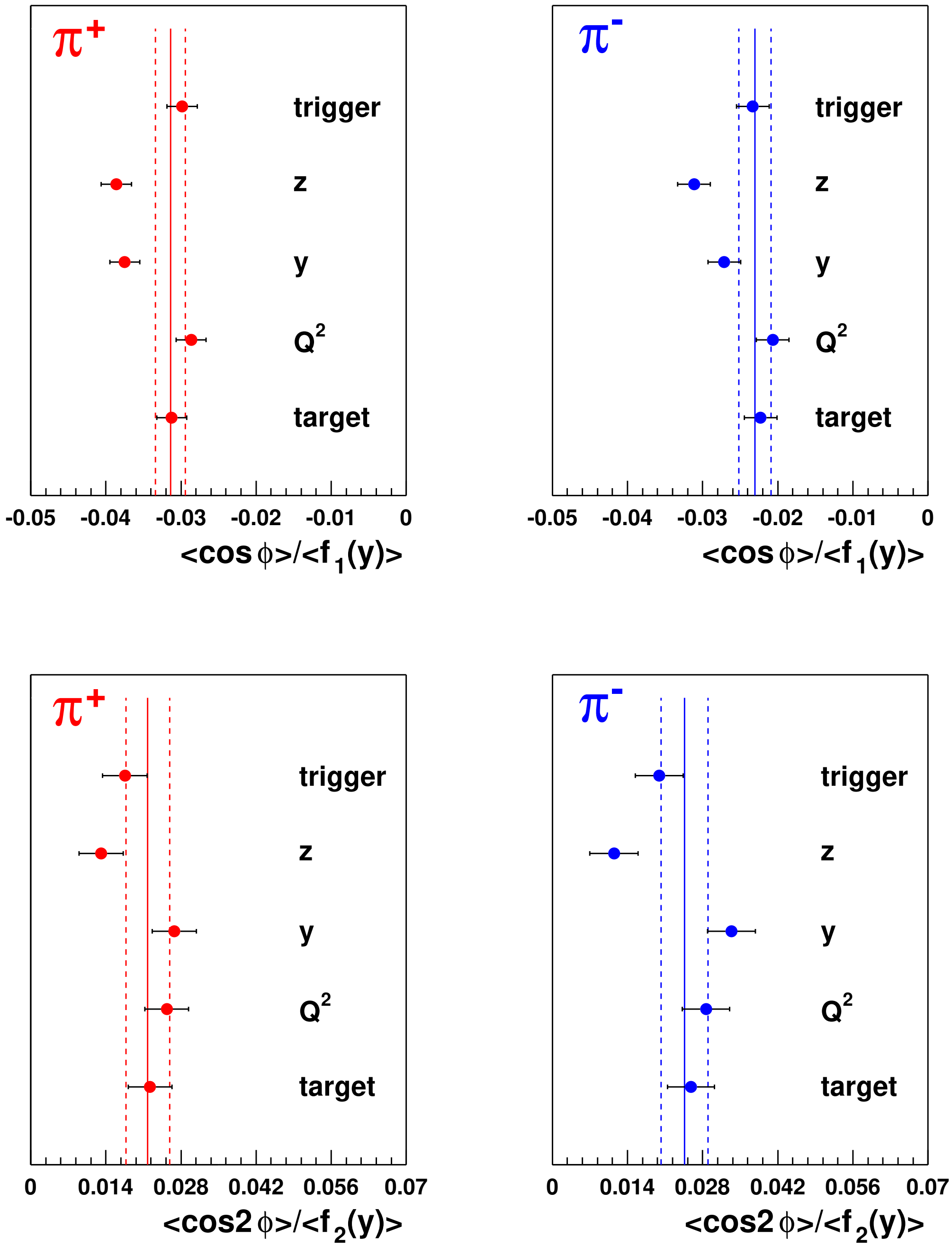

Figure 4.29: Upper row: $\langle\cos\phi\rangle/\langle f_1(y)\rangle$ of the *all hadron* samples (left π^+, right π^-), for different corrections on the Monte Carlo sample. The band indicates the result obtained without any correction with the corresponding error. The points mark the results of the analyses described in the following sections. From upper to lower point: correction for trigger ratios, corrections for kinematic variables: z, y and Q^2, different target cut. These absolute deviations correspond to relative changes up to 40% for the z-correction. Lower row: the same for $\langle\cos 2\phi\rangle/\langle f_2(y)\rangle$.

moment is observed when the correction is applied to the distribution in z. Here the relative correction is up to 35%. Also the correction for y yields results which are not compatible with the values obtained without the correction.

Target Position

As mentioned in Section 4.1.1 the positions of the target in Monte Carlo and data differ from each other. Therefore it is required that the vertex lies within a volume that is contained in both targets. A barrel around the Monte Carlo target axis is chosen arbitrarily. In order to find out whether the choice of the target volume influences the outcome of the analysis significantly, the same analysis was performed choosing the real target axis as symmetry axis of the accepted barrel.

The maximum difference in $\langle\cos\phi\rangle/\langle f_1(y)\rangle$ which results from this change in the analysis lies below 1% and therefore the error which is introduced through the target is much smaller than the statistical error of the result and can be neglected for the time being.

Contribution of Ghost Tracks

Another source of difference in data and Monte Carlo are so-called *ghost tracks*. In principle, these are tracks which are reconstructed although there was no particle which caused the hits the track was reconstructed from. In the reconstructed Monte Carlo sample ghost tracks can be identified, since no generated track can be attributed to them from which they are derived. For the Monte Carlo there is yet another reason for missing association which is not in the data: The association algorithm sometimes fails although the track is existing in both samples. This is due to a problem in the algorithm used to produce the Monte Carlo sample. Agreement in 100% of the hits of the generated and reconstructed track is necessary to associate these tracks with each other. More recent versions of the software demand a less strict criterion to be fulfilled and thus have a better efficiency in the association.

For this analysis, which is performed using Monte Carlo produced with the old version of the software, the ghost tracks are considered to be tracks which are not reconstructed correctly and hence they are discarded. After all cuts, they would make about 10% of all tracks in the reconstructed Monte Carlo sample (c.f. Tables B.6 and B.7 in App. B.1). As long as their distribution in ϕ is the same as that of the associated hadron tracks, they influence only the statistical error of the acceptance function. However, Fig. 4.30 shows that this is not the case. In order to estimate the change in the moments in case the ghost tracks are included in the Monte Carlo sample, the moments are calculated for the complete hadron sample, where no separation of charges or cells has been performed (see Fig. 4.31). There is no significant change in $\langle\cos\phi\rangle$, where the calculation without the ghost tracks yields -0.0241 ± 0.0014 in contrast to a value of -0.0237 ± 0.0014. For $\langle\cos 2\phi\rangle$ the corresponding values are 0.0098 ± 0.0014 without, and 0.0077 ± 0.0014 with the ghost tracks included.

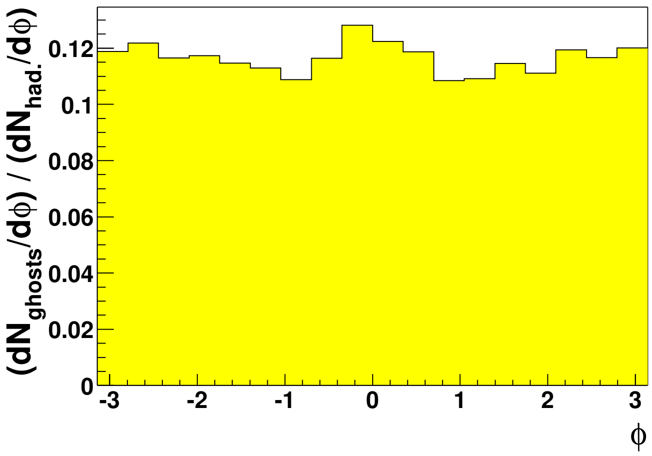

Figure 4.30: Ratio of the ϕ-distribution of the ghost tracks over the ϕ-distribution of the associated hadron tracks. The distributions are obtained from the corresponding *all hadron* sample (no separation of charges or target cells). The ratio should be uniformly distributed if the failing in the association of reconstructed to generated tracks was ϕ-independent.

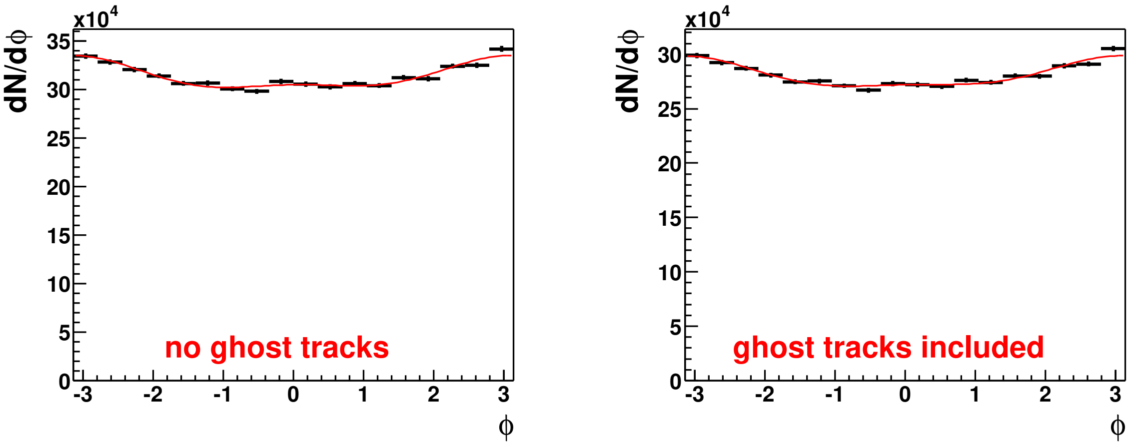

Figure 4.31: Impact of the ghost tracks on the acceptance correction of the ϕ-distributions of the data. Left: Distribution corrected with the acceptance function excluding the ghost tracks (as done in the main analysis). Right: Including the ghost tracks. The distributions are obtained from the complete *all hadron* sample, without separation of charges or target cells.

4.4.2 Other Systematic Errors

Final State Photon Radiation

Like gluons which are radiated by the quarks during the scattering process (Sec. 3.2.2), also photon radiation introduces an angular modulation of the cross section. This radiation is not included in the Monte Carlo used for the correction of the detector acceptance. Other Monte Carlo studies, including these modulations, have been shown by A. Kotzinian [Kot03]. In order to estimate the resulting influence on the moments, a fit of the form $A + B\cos\phi + C\cos(2\phi) + D\cos(3\phi) + E\cos(4\phi)$ was applied to the distribution shown in this reference (see Fig. 4.32). The distributions of the kinematic variables of this special Monte Carlo sample (also shown in [Kot03]) are comparable to those of the *all hadron* sample used for this analysis. The resulting moments, integrated over the whole available kinematic range, are $\langle\cos\phi\rangle = -0.034$ and $\langle\cos 2\phi\rangle = 0.018$. Assuming $\langle f_1(y)\rangle = 1$ and $\langle f_2(y)\rangle = 0.5$, this corresponds to about $\langle\cos\phi\rangle/\langle f_1(y)\rangle = -0.034$ and $\langle\cos 2\phi\rangle/\langle f_2(y)\rangle = 0.036$. This means that the higher order QED contributions are on the order of magnitude of the observed $\langle\cos\phi\rangle/\langle f_1(y)\rangle$ and $\langle\cos 2\phi\rangle/\langle f_2(y)\rangle$ of the *all hadron* sample. A more detailed analysis of Monte Carlo simulations of final state photon radiation would be necessary to determine the dependence of these contributions on the kinematic variables. E.g. these contributions should be high at values of p_T above about 2 GeV/c and should vanish at high z, like in case of the radiation of gluons. Thus the influence on the sample of leading hadrons is somewhat smaller because of the higher $\langle z\rangle$ of this sample.

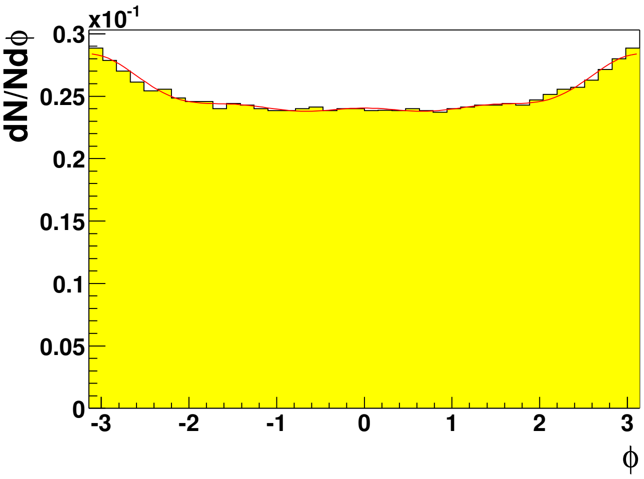

Figure 4.32: ϕ-dependence of higher order QED processes [Kot03]. The line shows the fit of a function $A + B\cos\phi + C\cos(2\phi) + D\cos(3\phi) + E\cos(4\phi)$ to the distribution.

Misidentification of Particles

Two systematic contributions due to particle misidentification occur. First, all hadrons are assumed to be pions and hence the corresponding kinematic variables which depend on the particle mass are wrongly calculated. This affects z and x_F and leads to a systematic shift to lower reconstructed values of these variables and a broadening of the z-resolution for the heavier hadrons (see Fig. 4.33), which make about 20% of the *all hadron* sample and 25% of the leading hadrons sample (see Tab. B.7 in the appendix). This can cause smearing effects if the results are calculated in bins of these variables. For the distribution of the difference of the values of z calculated from the generated and reconstructed track parameters, $\delta z := z_{gen} - z_{rec}$, one obtains a full width at half maximum of 0.0020, 0.0028 and 0.0044 for pions, kaons and protons respectively. The larger width of the distributions of the heavier hadrons, together with their shifts to negative δz, leads to a width of 0.0028 for the complete hadron sample. This loss in the resolution of z can be neglected since the width of the bins (see Tab. B.2.2, Page 97) is larger than the resolution in the corresponding variable.

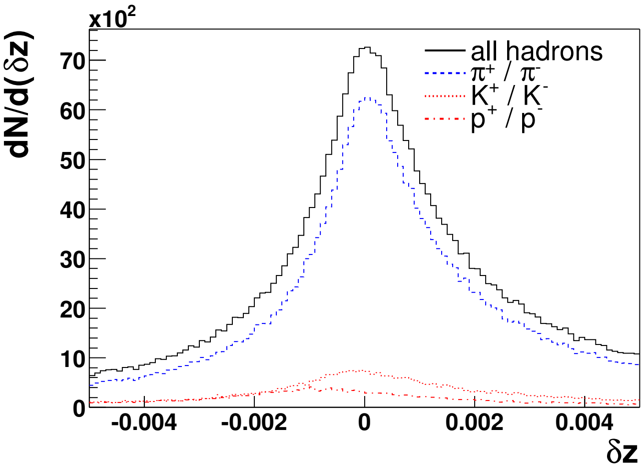

Figure 4.33: Resolution in z. The plotted variable is $\delta z := z_{gen} - z_{rec}$ of the full Monte Carlo sample (solid line) and for the three most frequent hadron types separately (other lines). The full width at half maximum of the overall distribution is 0.0028. The shift of the kaon- and proton-distributions to negative δz and the increasing widths are the result of the attribution of pion mass in the reconstruction of these particles, which leads to a systematic underestimation of z_{rec}.

The second contribution is the influence of a lepton contamination in the hadron sample. The influence of muons which are falsely treated as hadrons shows up in an analysis in which tracks are accepted as hadrons for which no calorimeter information is available. Even if tracks are rejected which have hits behind the muon absorbers, the contamination with these tracks causes large differences in the results for π^+ and π^- and also is a source of significant changes on the moments. The influence on $\langle\cos\phi\rangle$ is especially strong in the highest z-bin. There a very obvious and narrow peak is observed at $\phi = 0$ in the ϕ-distribution of the π^+. This results in a value of $\langle\cos\phi\rangle/\langle f_1(y)\rangle$ in this bin which is almost zero. The spike does not show up in the distribution for the π^-. Thus tracks without information from the energy measurement are discarded. Estimating the background from remaining muons is difficult, but due to strict cuts on the hadron candidates this contamination is probably small enough to be negligible in most kinematic bins. However, the deviating behaviour of $\langle\cos\phi\rangle/\langle f_1(y)\rangle$ and $\langle\cos 2\phi\rangle/\langle f_2(y)\rangle$ of the π^+ sample in the highest bin of z can at least partly be caused by misidentified muons.

According to the composition of particle types which can be found in the reconstructed Monte Carlo sample (see Tab. B.6), there is also a non-negligible admixture of electrons and positrons, which makes up about 8% of the sample. In contrast to the ϕ-distribution of the hadron tracks in the reconstructed Monte Carlo sample, which shows a negative $\langle\cos\phi\rangle$ due to the detector acceptance, the ϕ-distribution of the electrons exhibits a positive $\cos\phi$-moment (see Fig. 4.34). This means that, given there is also a large fraction of electrons in the data sample, this electron contamination leads to an underestimation of the $\cos\phi$-moment of the hadron distribution. Estimating the magnitude of this effect is difficult, since it is doubtful whether the numbers obtained from the Monte Carlo simulation are reliable. The number of radiation lengths, that an electron or positron must have passed in order to be accepted as an hadron candidate, should be large enough to discard almost all electrons from the hadron sample. Thus a fraction of 8% seems to be an overestimation.

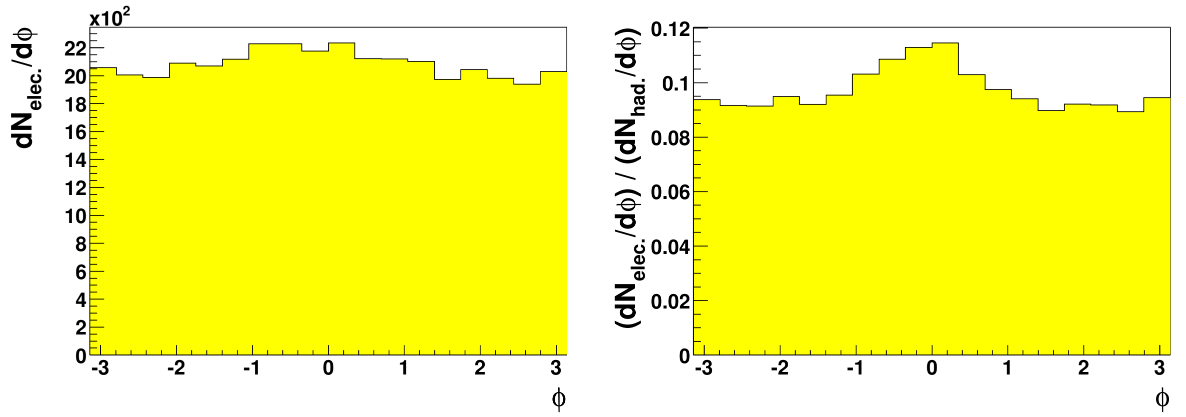

Figure 4.34: Left: ϕ-distribution of the electrons and positrons in the reconstructed Monte Carlo sample (all hadrons, no separation of charges or target cells). Right: Comparison with the ϕ-distribution of the produced hadrons. Obviously the ratio is not flat, thus an admixture of electrons in the real data can bias the moments of the ϕ-distribution.

Procedures for Acceptance Correction and Fitting

In order to cross-check the code and to estimate the order of magnitude of the error occurring during the fitting procedure, the analysis is performed for the sample of reconstructed Monte Carlo instead of the real data. This is done for the same sample as is used for the correction of the *all hadron* sample. The resulting asymmetries are mostly compatible with zero as expected (see Tab. 4.7). The z-dependence (see Fig. 4.35) of the moments allows to estimate the fluctuations of the result that are introduced by the procedures for the correction for acceptance and for fitting. The resulting fluctuation is below 0.01 and therefore negligible compared to the contributions estimated in Sec 4.4.1.

	π^+	π^-
$\langle\cos\phi\rangle/\langle f_1(y)\rangle$	-0.001 ± 0.003	-0.002 ± 0.003
$\langle\cos 2\phi\rangle/\langle f_2(y)\rangle$	-0.001 ± 0.005	-0.005 ± 0.006
$\langle\sin\phi\rangle/\langle f_3(y)\rangle$	$+0.001 \pm 0.010$	-0.007 ± 0.010

Table 4.7: Overall $\langle\cos\phi\rangle/\langle f_1(y)\rangle$ and $\langle\cos 2\phi\rangle/\langle f_2(y)\rangle$ as it is extracted from the Monte Carlo sample which is used for the correction for the acceptance. The values are expected to be compatible with zero.

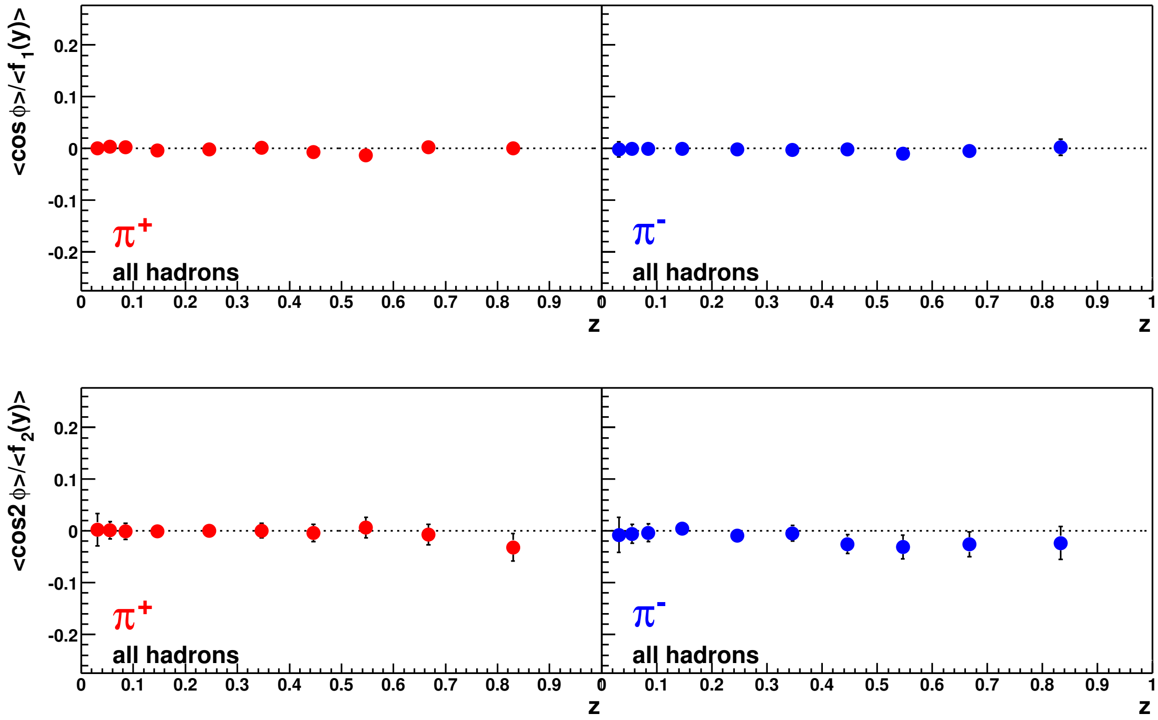

Figure 4.35: Dependence of $\langle\cos\phi\rangle/\langle f_1(y)\rangle$ and $\langle\cos 2\phi\rangle/\langle f_2(y)\rangle$ from the reconstructed Monte Carlo sample on z. The correction for acceptance is applied.

Errors of ϕ-Distributions of the *All Hadron* Sample

Since all hadrons in a given event are used for the analysis of the *all hadron* sample, it happens that more than one hadron per event enter a certain bin of the histograms which are fitted. This means that the distributions are no longer Poissonian and the statistical error is [GP04, Pre97]

$$(\delta N_h)^2 = \frac{\langle n_h^2 \rangle}{\langle n_h \rangle} N_h \equiv C^2 N_h \,. \tag{4.19}$$

N_h denotes the number of entries in one bin and n_h the number of entries coming from the same event. Yet the correction C^2 is close to 1 and therefore can safely be neglected.

This can be shown by calculating the correction for one single histogram which contains the full statistics. The value obtained is $C^2 < 1.059$, which means that in this case the error would be underestimated by a factor $1/C = 0.97$ when assuming a Poisson distribution. This is a lower limit for the binned distributions which are sub-samples of the tested one. For a check with positive hadrons only, the correction is even less, namely $C^2 < 1.024$. Furthermore, due to the low statistics of the Monte Carlo available so far, the statistical error is dominated by the error of the acceptance function.

Chapter 5

Discussion of the Results

5.1 Dependence on the Kinematic Variables

The results shown in Chapter 4.3 exhibit a contradictory behaviour. On the one hand some of the predictions of Cahn and the QCD seem to be confirmed by the data. On the other hand there are features in the kinematic dependence which can not be explained by these predictions. Moreover it is not yet clear which role the final state photon radiation plays in different kinematic regions. Additional uncertainty in the interpretation of the dependencies of the result on the different kinematic variables comes from the correlation between these. Due to these correlations "hidden" dependencies on other variables can influence the dependence on the plotted variable.

According to Cahn [Cah78], the angular modulation in the SIDIS cross section should be dominated by the contribution of the intrinsic transverse momenta of the quarks at COMPASS kinematics of $\langle Q^2 \rangle < 2.5\,(\mathrm{GeV}/c)^2$ (see Tab. B.13 in the appendix). He estimates this effect to be larger than the QCD contribution, as long as

$$Q < 4\frac{k_T}{\alpha_s} \approx 20k_T\,. \tag{5.1}$$

Assuming $k_T \approx 0.5\,\mathrm{GeV}/c$ this estimation yields $Q^2 < 100\,(\mathrm{GeV}/c)^2$ as the upper limit of the kinematic region in which the Cahn effect should be the strongest contribution. The pure leading order cross section at quark level as calculated by Cahn (see Eq. 3.28) predicts the dependence on y and Q^2.

The complicated y-dependencies have been removed from the moments by dividing them by the $\langle f_i(y) \rangle$. Hence no y-dependence should be observed as long as the effect is fully described by Cahn's ansatz. But in fact the corrected moments both show a strong dependence on y. Furthermore the y-dependence of the results for π^+ and π^- shows larger disagreement than observed in any other kinematic variable, though no difference in the production cross section for positively and negatively charged hadrons is predicted by Cahn. One cannot exclude that the observed y-dependence is due to some hidden correlation of y to other kinematic variables. It might be however, that the significant deviation in the

y-dependence of the two charges indicates that after reducing the influence of the Cahn effect, the modulation of the moments as a function of y is dominated by some other effect.

The dependence of the cross section on Q^2 is simpler and therefore the results given in Chap. 4.3 are not corrected for this dependence. According to Cahn's calculation $\langle\cos\phi\rangle$ slopes like $1/Q$. Actually only a weak Q^2-dependence is observed. This behaviour matches somewhat better the prediction for the QCD-effects, where the only dependence on this variable is introduced by the strong coupling constant α_s, which itself shows only a weak dependence on Q^2. Cahn's prediction of $\langle\cos 2\phi\rangle \propto f_2(y)/Q^2$ suggests for a value of $Q^2 \approx 2.4\,(\mathrm{GeV}/c)^2$ (see Tab. B.12), $\langle f_1(y)\rangle \approx 1$ and $\langle f_2(y)\rangle \approx 0.5$ that the ratio $(\langle\cos 2\phi\rangle/\langle f_2(y)\rangle)\,/\,(\langle\cos\phi\rangle/\langle f_1(y)\rangle)$ should be approximately one. For the sample of all hadrons the results agree with this prediction, while for the leading hadrons the results on $\langle\cos 2\phi\rangle/\langle f_2(y)\rangle$ are consistent with zero. However, the interpretation of the $\cos\phi$-moment is especially difficult since it is very sensitive to the detector acceptance as shown in Sec. 4.2.4.

Eq. 3.28 (see Pg. 20) gives the cross section for the Cahn effect at the quark level. Assuming an empiric ansatz for the fragmentation function, one can give the complete cross section and its dependence on the hadron azimuthal angle ϕ. Such an attempt for example gives [Kot03, Kot95], which is similar to the corresponding cross sections in [CES92], but simplified by neglecting weakly contributing terms:

$$\frac{d\sigma}{dx\,dy\,dz\,dp_T\,d\phi} \propto \exp\Big(-\frac{p_T^2}{\langle p_T^2\rangle}\Big)[1+(1-y)^2-4(2-y)\sqrt{1-y}\frac{p_T z\langle k_T^2\rangle}{Q\langle p_T^2\rangle}\cos\phi]\,. \quad (5.2)$$

This is the cross section for unpolarised scattering up to first order in $\cos\phi$. Higher order moments are not calculated in the references given. Also QCD effects are not taken into account here. From Eq. 5.2 one can calculate the corresponding overall $\cos\phi$-moment of the distribution by dividing the ϕ-dependent part by twice the contribution independent of ϕ (see Eq. 3.31, Pg. 21) and averaging the result over the full kinematic range. This yields

$$\langle\cos\phi\rangle = -2\Big\langle\frac{f_1(y)p_T z}{Q}\Big\rangle\frac{\langle k_T^2\rangle}{\langle p_T^2\rangle}\,. \quad (5.3)$$

Accordingly, if $\langle\cos\phi\rangle$ is plotted as a function of z or p_T, one expects a linear dependence of the form

$$\langle\cos\phi\rangle(z) = -2\Big\langle\frac{f_1(y)p_T}{Q}\Big\rangle\frac{\langle k_T^2\rangle}{\langle p_T^2\rangle}z \qquad \text{and} \qquad \langle\cos\phi\rangle(p_T) = -2\Big\langle\frac{f_1(y)z}{Q}\Big\rangle\frac{\langle k_T^2\rangle}{\langle p_T^2\rangle}p_T\,. \quad (5.4)$$

Since the fragmentation functions enter the cross section as multiplicative terms, the dependence of $\langle\cos 2\phi\rangle$ on the variables introduced by fragmentation, namely z and p_T can be expected to be the same as for $\langle\cos\phi\rangle$. The moments depend linearly on both variables. In z the COMPASS results, at least for the sample of all hadrons, show the expected linear behaviour at $z > 0.15$. This agrees with the fact that at high values of z neither QCD nor higher order QED processes can contribute noticeably to the angular modulation due to energy conservation. At low z $\langle \cos\phi \rangle / \langle f_1(y) \rangle$ becomes positive for the *all hadron* sample. This behaviour is expected, since in this region hadrons from target fragmentation are enriched. These are expected to carry opposite signs of p_T than the current fragments for reasons of momentum conservation. Hence they cause positive $\cos\phi$-moments. The z-dependence of $\langle \cos 2\phi \rangle / \langle f_2(y) \rangle$ shows no corresponding behaviour. A clean Cahn effect can only be observed at small values of p_T. Values of p_T^2 which are much higher than $\langle k_T^2 \rangle + \langle (p_T^f)^2 \rangle$ (see Eq. 3.41, Pg. 23) can not be reached without final state radiation. The observed p_T-dependencies show a linear behaviour up to $p_T \approx 0.5\,\mathrm{GeV}/c$. Then there is further linear decrease, but with a smaller slope. For the sample of all hadrons the result is significantly positive at low p_T, which is not in agreement with the predictions by Cahn. No noticeable dependence of $\langle \cos 2\phi \rangle / \langle f_2(y) \rangle$ on p_T is measured.

Though the variables x and x_F do not enter the moments of the Cahn cross section (Eq. 5.3) directly, one can observe a dependence on them. The x_F-dependence mirrors the dependence on z, because of the said correlation between these two quantities (Sec. 4.3). A dependence of the cross section on x is introduced by the QCD-contributions (see Sec. 3.2.2). Theoretical predictions of this x-dependence of $\langle \cos\phi \rangle$ and $\langle \cos 2\phi \rangle$ exist [Oga03, GGO04], but for values of Q^2 above and values of p_T somewhat below the COMPASS values (see Tab. B.12 in the appendix). The shape of the calculated curves for $\langle \cos\phi \rangle$ resembles that of the COMPASS result, but with the minimum being shifted compared to the COMPASS result to higher x of about 0.06 and with an overall magnitude, which is more than twice the magnitude observed.

In summary, the quark level Cahn cross section is poorly mirrored in the data, while the dependence on the fragmentation seems to match the predictions better. This suggests that even in the kinematic region of COMPASS, where the Cahn effect is predicted to play an important role, contributions from QCD and higher order QED or unknown other effects are necessary to explain the measured results. Although the observed behaviour can not be explained satisfactorily by the Cahn effect, the sources of the kinematic dependence must be of fundamental physical nature. Major failings of the analysis procedure can be excluded, since the COMPASS results on the whole confirm the observations obtained by the EMC and E665 experiments. These are the subject of Section 5.3.

5.2 Estimate of $\langle k_T^2 \rangle$

The simplest approach to estimate $\langle k_T^2 \rangle$ is to solve Eq. 5.3 for this value by putting in the moment from the fit to the overall ϕ-distribution and the corresponding averaged values. This has to be done for the leading hadron sample, since this sample is the one that gives the cleanest access to the Cahn effect. Also Equations 5.4 can be exploited for a determination of $\langle k_T^2 \rangle$ by fitting the linear z and p_T-dependence to the values of $\langle \cos\phi \rangle$. $\langle k_T^2 \rangle$ can then be determined from the slope by dividing by the corresponding average value. The resulting fits are shown in Fig. 5.1. In case of the p_T-dependence, only the range $0 < p_T < 0.5\,\mathrm{GeV}/c$ is used for the fit because at high values of p_T the influence of the QCD contributions to

$\langle\cos\phi\rangle$ rises. The dependence on z is fitted in the range $0 < z < 0.8$. This means that the last data point, which shows the strange behaviour (see Sec. 4.3) is not taken into account. Also the average values $\langle f_1(y)p_T/Q\rangle$ and $\langle f_1(y)z/Q\rangle$ are determined in the corresponding kinematic ranges. Although no constant term is expected it is included in the fit. In three of the four cases the constant differs significantly from zero. This may be taken as a hint that this approach to extract $\langle k_T^2\rangle$ is too naive and that there are other contributions than just the pure Cahn effect.

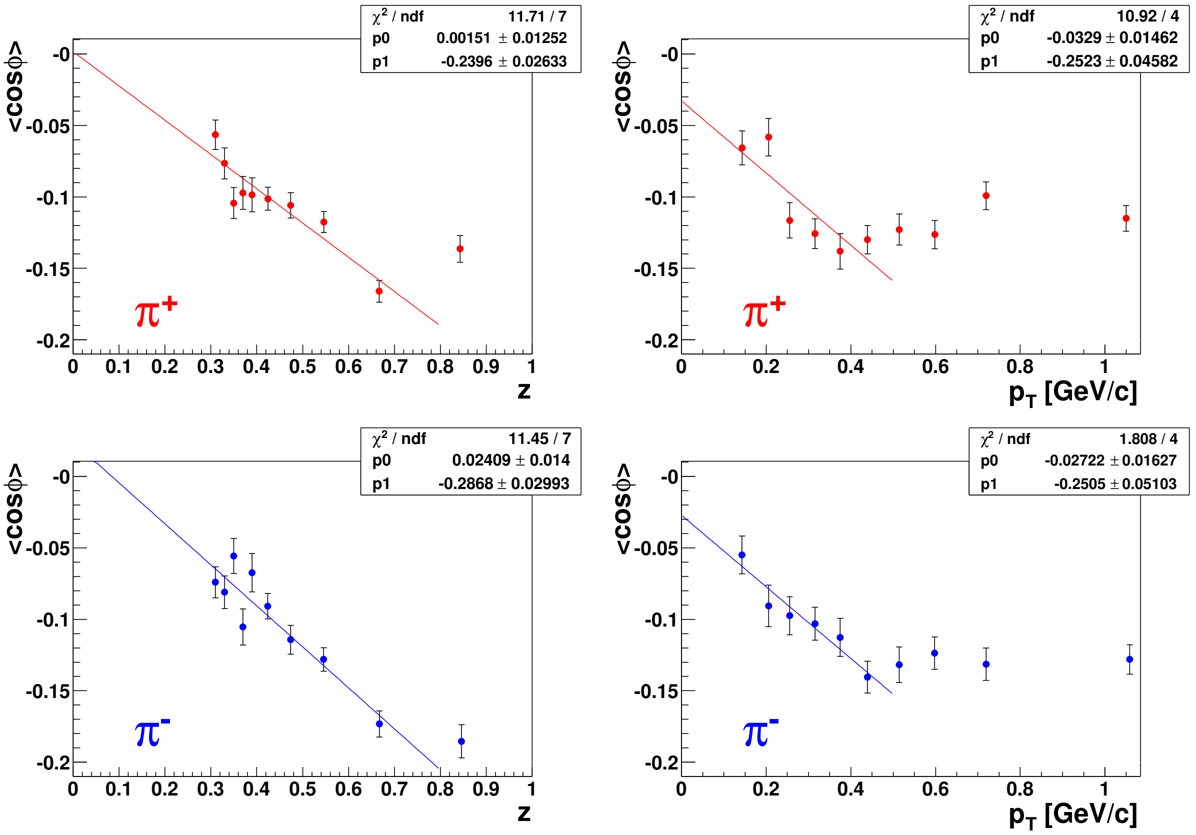

Figure 5.1: Fits of a function $f(z) = p_0 + p_1 z$ to the z-dependence (left) and $f(p_T) = p_0 + p_1 p_T$ to the p_T-dependence (right) of $\langle\cos\phi\rangle$ of the sample of leading hadrons. Top row: π^+, bottom row: π^-.

The results from these attempts of extracting $\langle k_T^2\rangle$ are listed in Tab. 5.1. If $\langle k_T^2\rangle$ is extracted from the averaged values for each of the ten kinematic bins, the result varies from bin to bin, with the variation being much stronger than the statistical errors of the estimation. This indicates that the ansatzes chosen are too simple and that the other effects which are not taken into account here, may not be neglected. Therefore it is difficult to extract a reliable value of $\langle k_T^2\rangle$ from the data. The safest approach to determine $\langle k_T^2\rangle$ would be to include non-zero k_T and final state radiation effects in Monte Carlo studies and to adapt the size of $\langle k_T^2\rangle$ to fit the asymmetries from the experiment.

method	$\langle p_T^2 \rangle$ $\pi^+ \mid \pi^-$	$\langle * \rangle$ $\pi^+ \mid \pi^-$	$\langle k_T^2 \rangle$ $\pi^+ \mid \pi^-$
z-dependence	$0.367 \mid 0.363$	$0.278 \mid 0.281$	$0.16 \pm 0.02 \mid 0.19 \pm 0.02$
p_T-dependence	$0.367 \mid 0.363$	$0.265 \mid 0.274$	$0.17 \pm 0.03 \mid 0.17 \pm 0.03$
overall $\langle \cos\phi \rangle$ (upst.)	$0.359 \mid 0.352$	$0.138 \mid 0.136$	$0.127 \pm 0.007 \mid 0.134 \pm 0.008$
overall $\langle \cos\phi \rangle$ (downst.)	$0.373 \mid 0.373$	$0.138 \mid 0.138$	$0.164 \pm 0.006 \mid 0.162 \pm 0.007$
average of two cells			$0.148 \pm 0.004 \mid 0.150 \pm 0.005$

Table 5.1: Estimated values of $\langle k_T^2 \rangle$ (fourth column) from the fits to the z- and p_T-dependence of $\cos\phi$ and the direct calculation from the overall moment. The values in the second and third column give the averages which are used to estimate the value of $\langle k_T^2 \rangle$ from the fit parameters (see Fig. 5.1) or the overall moments (see Tab. 4.5). In the second column the average p_T^2 is given. This is calculated integrating over the full kinematic range available. The abbreviation $\langle * \rangle$ in the third column stands for $\langle f_1(y) p_T/Q \rangle$ (for the fit to the z-dependence), $\langle f_1(y) z/Q \rangle$ (for the fit to the p_T-dependence) and $\langle f_1(y) z p_T/Q \rangle$ (for the extraction from the overall moments) respectively. While the latter again integrates over the full kinematic range, for the former two only the range in which the fit is applied is taken into account.

5.3 Results from Previous Experiments

EMC at CERN

The EMC experiment at CERN has twice published results on the Cahn effect [Aub83, Arn87]. EMC was operated with polarised muon beams of 120 and 280 GeV and an unpolarised fixed proton target. The analysis performed in this thesis in principle follows the analysis as it was performed at EMC. Especially, the weighting of the moments with the $\langle f_i(y) \rangle$ is done to gain comparability with this experiment. However, there are differences in the kinematic range covered by EMC and also in the cuts on the kinematic variables (see Tab. 5.2). At EMC a sample was analysed which contains all hadrons from a given event. In contrast to this work, a cut on $z > 0.15$ selects hadrons from the current fragmentation only. Positively and negatively charged hadrons were not treated separately.

	COMPASS	**EMC**	**E665**
y	$0.1 < y < 0.9$	$y < 0.8$	$0.1 < y < 0.85$
z	no cut	$z > 0.15$	no cut
p_T	$p_T > 0.1\,\mathrm{GeV}/c$	$p_T > 0.2\,\mathrm{GeV}/c$	no cut
Q^2	$Q^2 > 1\,(\mathrm{GeV}/c)^2$	$Q^2 > 5\,(2)\,(\mathrm{GeV}/c)^2$	$Q^2 > 3\,(\mathrm{GeV}/c)^2$
W^2	$W^2 > 16\,(\mathrm{GeV}/c^2)^2$	$W^2 > 160\,(60)\,(\mathrm{GeV}/c^2)^2$	$300\,(\mathrm{GeV}/c^2)^2 < W^2 < 900\,(\mathrm{GeV}/c^2)^2$

Table 5.2: Comparison of the kinematic ranges covered by COMPASS, EMC and E665. The EMC values in bracket hold for the lower beam energy.

EMC observed a negative $\langle \cos\phi \rangle / \langle f_1(y) \rangle$, while $\langle \cos 2\phi \rangle / \langle f_2(y) \rangle$ is compatible with zero with a tendency to positive values. Since the asymmetry strongly depends on $\langle z \rangle$ of the sample, for comparability the analysis of the *all hadron* sample is performed with an additional cut on $z > 0.15$ as EMC did. The results of this analysis, together with the EMC results are shown in Figs. 5.2 and 5.3. Within the relatively large statistical errors of the 1983 EMC results the z- and p_T-dependences of $\langle\cos\phi\rangle/\langle f_1(y)\rangle$ agree with the behaviour found within this analysis. In the z-dependence systematic differences between the results of the two experiments can be observed at low values of z. In this region the angular modulation measured by COMPASS is much smaller than that observed by EMC. At high z the results match. The mismatch in the region of low z can have two reasons. Either the QCD contributions, which should be strongest at low z, are much larger in the range of W^2 EMC has measured than in the COMPASS range (for comparison: the average value of the COMPASS data sample is $\langle W^2\rangle = 104\,(\mathrm{GeV}/c)^2$). Or, more probably, the deviations are caused by systematic errors in this kinematic region, e.g. from the acceptance correction. Until the 1987 publication, the data statistics was enhanced and the observed kinematic region was extended to negative x_F. The dependence of the 1983 results as well as of the results from the new data on x_F is shown in Fig. 5.3.

The EMC results were interpreted by means of theoretical calculations of König and Kroll [KK82]. A non-zero k_T as well as first order QCD effects were taken into account. The outcome of these calculations depended only weakly on the QCD contributions and on the model that was assumed for the fragmentation. On the other hand, a strong dependence on k_T was calculated. Therefore the conclusion was that within the valid energy range the Cahn Effect still dominates the azimuthal modulation. A fit of the Monte Carlo predictions to the data, including the contributions by QCD, yielded an average transverse quark momentum of about $\langle k_T\rangle = 0.7\,\mathrm{GeV}/c$. This corresponds to $\langle k_T\rangle^2 = 0.49\,(\mathrm{GeV}/c)^2$, which is a lower limit for $\langle k_T^2\rangle$.

E665 at Fermilab

E665 investigated the scattering of 490 GeV muons off fixed hydrogen and deuteron targets [Ada93]. Therefore their invariant photon-nucleon mass region is even higher than the range covered by EMC (see Tab. 5.2 for a list of the most important cuts used for this analysis). Only high multiplicity events with at least four charged hadrons from the current fragmentation ($x_F > 0.2$) region were studied. This restriction probably leads to a much lower $\langle z\rangle$ of the sample compared to the corresponding value at COMPASS. No separation of positively and negatively charged hadrons was done.

In the said publication the $\langle\cos\phi\rangle$ extracted from the azimuthal asymmetries are shown as a function of the minimum p_T of the sample considered. The comparison of these results to the COMPASS results is difficult, since the average p_T and z of the E665 results are not known. E665 observed a $\langle\cos\phi\rangle$ which decreases with increasing p_T^{cut} to a minimum value of -0.12 at $p_T^{cut} = 1.5\,\mathrm{GeV}/c$. With larger p_T^{cut} the angular modulation grows smaller again. At $p_T^{cut} = 1.0\,\mathrm{GeV}/c$ the asymmetry is about -0.11. This corresponds to the COMPASS value in the highest bin of p_T, where $\langle p_T\rangle$ is somewhat higher than $1\,\mathrm{GeV}/c$. Therefore one can state that at least the order of magnitude of $\langle\cos\phi\rangle$, together with the decreasing

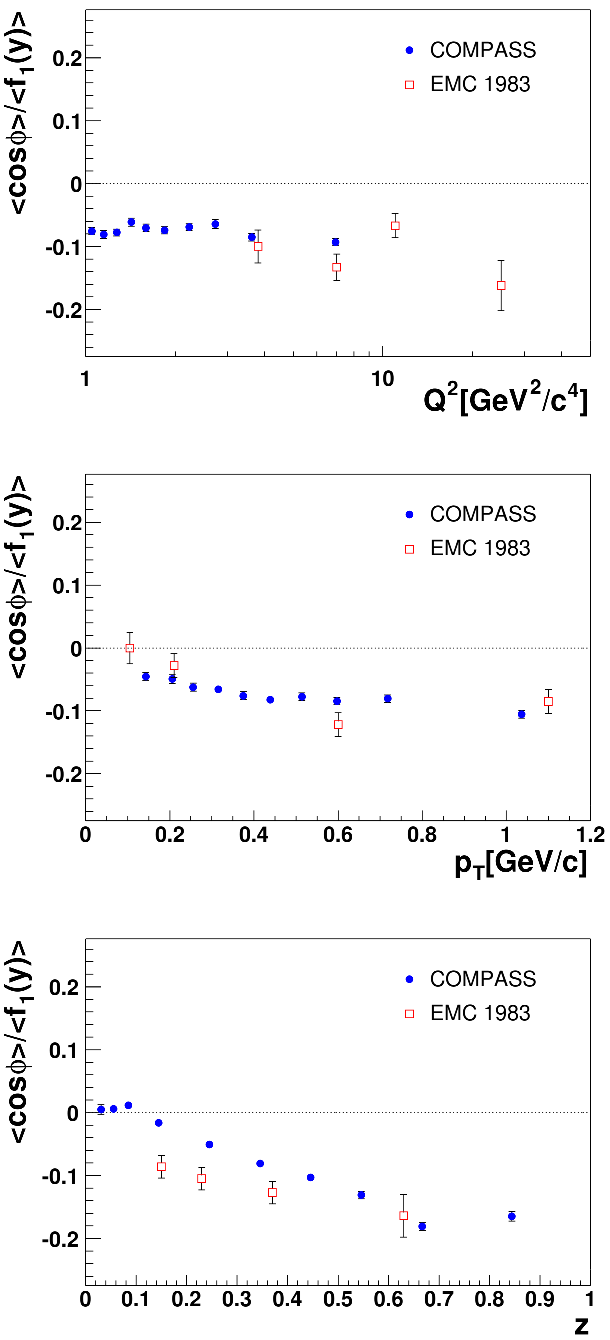

Figure 5.2: Comparison of the dependence of $\langle \cos\phi \rangle / \langle f_1(y) \rangle$ on Q^2 (top), p_T (middle) and z (bottom) as measured at EMC and COMPASS. The COMPASS values are extracted from the *all hadron* sample, with an additional cut on $z > 0.15$ (top and middle) to be comparable with the EMC results [Aub83]. Furthermore, the COMPASS results are averaged over the two hadron charges. Note that the EMC cut on p_T was lowered to $p_T < 0.05\,\mathrm{GeV}/c$ for the plot in the middle.

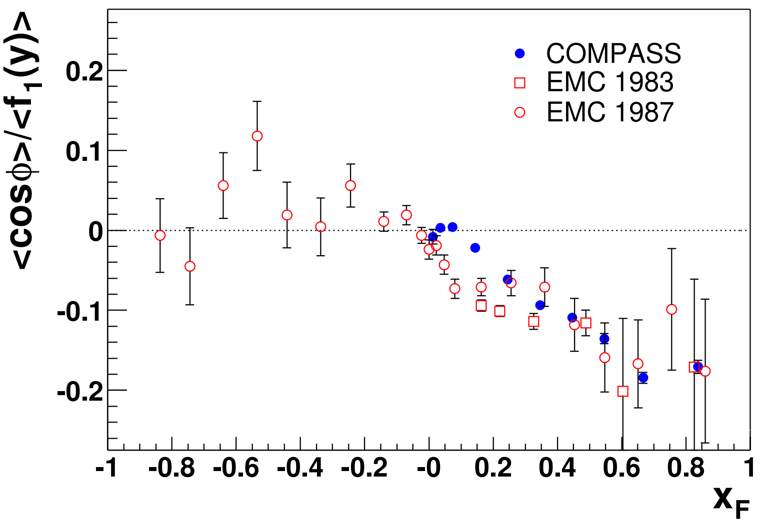

Figure 5.3: Comparison of the dependence of $\langle \cos\phi\rangle/\langle f_1(y)\rangle$ on x_F as measured at EMC [Aub83, Arn87] and COMPASS. The COMPASS results show the charge averaged moment as it is extracted from the *all hadron* sample. Some of the COMPASS error bars are too small to be visible in this plot.

behaviour of the p_T-dependence up to about $p_T = 1\,\mathrm{GeV}/c$ is common to both experiments.

Like the results by EMC, the E665 results were compared to model calculations including the QCD processes [CES92]. These were necessary to describe the experimental results. The intrinsic transverse quark momentum was estimated to be $\langle k_T\rangle = 0.5\,\mathrm{GeV}/c$. There was also an estimation of the transverse momentum p_T^f introduced by fragmentation, for which E665 obtained an averaged value of about $\langle p_T^f\rangle = 0.7\,\mathrm{GeV}/c$ which yields a lower limit of $\langle k_T^2\rangle > 0.25\,(\mathrm{GeV}/c)^2$.

5.4 Outlook

The analysis performed in this work leads to first results on the Cahn effect at COMPASS which look very promising. If the Monte Carlo statistics is enhanced, the statistical error of the result will no longer be dominated by the error of the acceptance function but by the contribution from the data. Then COMPASS will have the chance to use the data of more than one week of data taking and to do the analysis of the Cahn asymmetries with even finer kinematic binning than shown here. Multi-dimensional analyses will then be feasible and will help to understand the dependence of the results on the correlation between different kinematic variables. From these results a more reliable estimation of $\langle k_T^2\rangle$ can be extracted. Therefore the effects from the quark transverse momenta as well as models of the fragmentation and the QCD contributions have to be simulated in Monte Carlo, treating $\langle k_T^2\rangle$ as a free parameter which can be fit to the data.

Also a more precise measurement of $\langle \cos 2\phi \rangle$ will be possible, which, as mentioned in Sec. 3.2.1, can give access to a measurement of the Collins fragmentation function $H_1^{\perp}(z)$. Furthermore, the analysis could be performed using a sample of kaons identified by the RICH. These give access to events in which the γ^* was scattered off a strange quark from the sea and may answer the question whether the k_T-distributions of the valence and sea quarks differ from each other.

However, progress has to be made in improving the Monte Carlo quality and in understanding the higher order QED contributions to remove the large systematic uncertainties due to these influences. If the statistics increases, also the other sources of systematic errors will become larger compared to the statistical error. Therefore an effort will have to be made in reducing these errors or at least to get a more precise estimation of their magnitude.

Chapter 6

Summary

The COMPASS experiment at CERN aims at investigating the spin structure of the nucleon in polarised muon-nucleon scattering. In 2002 the first high quality DIS data have been taken for this purpose. This work contributes to the analysis of this data by investigating one of the spin-averaged effects that can be observed in DIS. The unpolarised SIDIS cross section shows a modulation in the azimuthal angle ϕ of the produced hadrons with respect to the muon scattering plane and the virtual photon direction. This behaviour has three main sources:

- The Cahn effect, which is a pure QED effect. Source of the angular asymmetry is the transverse momentum k_T of the struck quark with respect to the photon-nucleon direction.
- QCD contributions, where the angular modulation is due to transverse momentum which is transferred to the quark through the recoil of the gluon radiation.
- Final state photon radiation, which is a background to the interesting Cahn and QCD contributions.

These effects result in $\cos\phi$ and $\cos 2\phi$-moments of the unpolarised contribution to the cross section, which have been determined within this thesis. Furthermore a $\sin\phi$ moment has been extracted from the cross section which is due to the beam polarisation at the COMPASS experiment. In order to study the kinematic dependence of the modulation, the moments were measured as a function of the inclusive kinematic variables y, x and Q^2 as well as of the hadronic variables z, x_F and p_T. Since the Cahn effect determines the behaviour of the hadron produced from the struck quark, the so-called "leading hadrons" have been selected for the analysis. These have a high probability to contain the struck quark. The QCD effects on the other hand influence the complete set of hadrons from the current fragmentation. Therefore the analysis was in addition performed without leading hadron selection.

The main challenge of the Cahn analysis is to deal with the additional angular modulations introduced by the geometrical acceptance of the COMPASS spectrometer. A Monte

Carlo correction was applied to the data in order to correct for these contributions. While the $\cos\phi$-moment of the detector acceptance is lower than the result for the data, the $\cos 2\phi$-moment of the acceptance is somewhat stronger than that of the corrected data. Therefore the acceptance has to be determined precisely in order to obtain reasonable results from the data. The difficulty of the correction procedure lies therein that the Monte Carlo simulation available up to now describes the data in a way that is not satisfactory. Major effort was therefore put into estimating systematic errors occurring due to this mismatch.

However, the results show encouraging agreement with measurements of EMC and E665. Thus an interpretation of the data based on the theoretical predictions of Cahn, assuming only the lowest order QED process to contribute, was tried. This model turned out to be insufficient for explaining the observed kinematic dependence of the moments. The conclusion to be drawn from this is that probably all three mechanisms mentioned above influence the modulation in the cross section. The order of magnitude of the final state photon radiation was roughly estimated from a dedicated Monte Carlo simulation. This effect was found to be producing angular modulations comparable with the asymmetry found in the sample of all hadrons. It did not suffice to explain the larger modulations of the leading hadron ϕ-distributions. More detailed Monte Carlo studies of the final state radiation processes will offer an approach to separate the three contributions in future analyses.

The main interest in the analysis of the Cahn effect is to gain access to the transverse quark momenta and to determine the mean average momentum $\langle k_T^2 \rangle$. Simple attempts to extract $\langle k_T^2 \rangle$ from the results based on the assumption that the observed modulation is purely due to the Cahn effect have been tried. The results of these ansatzes differ but are in the expected order of magnitude. Nevertheless, compared to the $\langle k_T^2 \rangle$ estimated by EMC and E665 they are smaller by a factor of two. Advanced Monte Carlo studies will be necessary to get a more reliable estimate of $\langle k_T^2 \rangle$, taking into account the contributions of QCD and higher orders QED.

Appendix A

The $\sin\phi$-Moment

For the sake of completeness, the $\sin\phi$-moments, which are a by-product of this analysis, are presented in this section.

In the case of an unpolarised target and a polarised beam an additional angular modulation of the cross section can be observed. This is due to the correlation of the beam-spin projection onto the virtual photon momentum and the momentum component of the final state hadron transverse to this direction. The result of the correlation is a $\sin\phi$-moment in the SIDIS cross section, which, like the $\cos 2\phi$-moment caused by the Cahn effect, contains the Collins fragmentation function $H_1^\perp(z)$ [MT96]. The y-dependence of the $\sin\phi$-moment is (see Fig. A.1)

$$\langle \sin\phi \rangle \propto \frac{y\sqrt{1-y}}{1+(1-y)^2} =: f_3(y)\,. \tag{A.1}$$

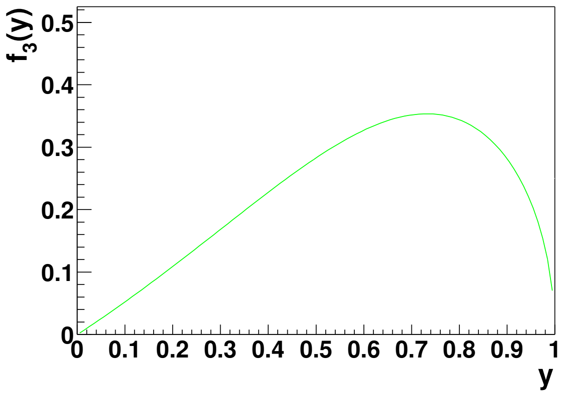

Figure A.1: Theory curves for the $f_3(y)$ and mean values $\langle f_3(y)\rangle$ calculated for the all hadrons sample (π^+ from downstream cell).

The $\sin\phi$-moment can be derived from the fit parameter D in Equation 4.12 (Sec. 4.12, Pg. 44) according to

$$\langle \sin\phi \rangle = \frac{D}{2A\langle P_b \rangle} \tag{A.2}$$

where $\langle P_b \rangle$ takes into account the average polarisation of the beam. The moments obtained from the fits to the overall distributions, normalised to the average value of the y-dependence $\langle f_3(y) \rangle$ are listed in Tab. A.1. The observed $\sin\phi$-moment takes positive values for π^+ and negative values for π^-.

	π^+		π^-	
	$\langle \sin\phi \rangle / \langle f_3(y) \rangle$	$\langle f_3(y) \rangle$	$\langle \sin\phi \rangle / \langle f_3(y) \rangle$	$\langle f_3(y) \rangle$
all hadrons	0.042 ± 0.011	0.200	-0.022 ± 0.012	0.202
leading	0.019 ± 0.027	0.156	-0.095 ± 0.029	0.161

Table A.1: Overall values of $\langle \sin\phi \rangle / \langle f_3(y) \rangle$; Left: π^+, right: π^-

In the course of the studies on the systematics which influence $\langle \cos\phi \rangle$ and $\langle \cos 2\phi \rangle$, also the $\sin\phi$-moment is considered. The influence of the trigger- and kinematic corrections, as well as the impact on the alternative target cut are shown in Fig. A.1. Neither of these corrections leads to significant changes in the result.

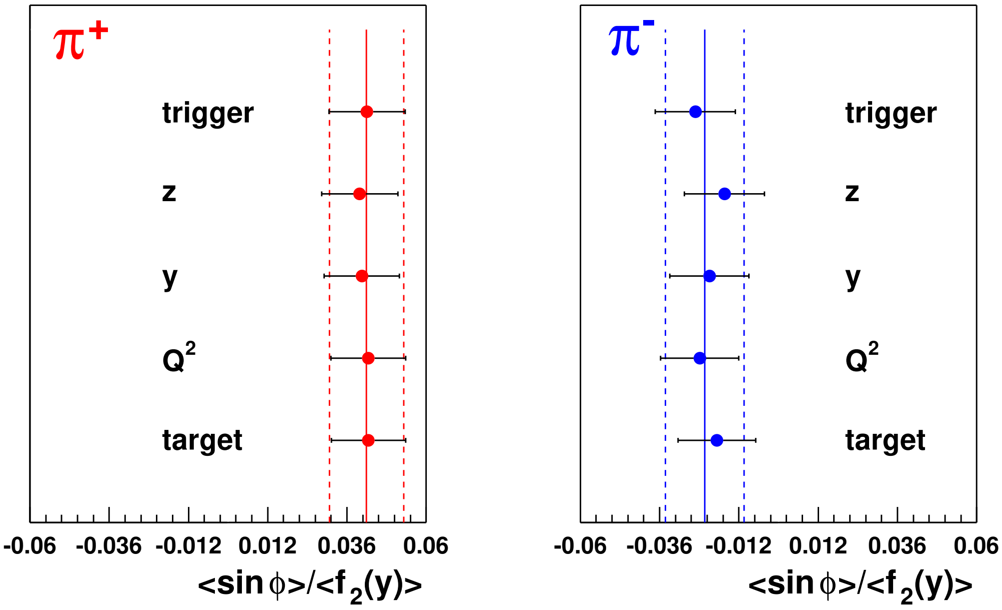

Figure A.2: The same as in Figure 4.29 (c.f. Pg. 65) for $\langle \sin\phi \rangle / \langle f_3(y) \rangle$

The dependencies of the result on the common kinematic variables are shown in Figures A.3 to A.5 (see Pg. 88 ff.). However, the interpretation of these results is very questionable since the influence of several systematic effects such as remaining contributions of the target polarisation can not be excluded, since no studies on these systematics have been performed. For this reason beam spin effects are usually extracted from more elaborated asymmetry measurements, where effects from other sources than the beam spin cancel out. Such measurements have been performed by HERMES [Air01] and more recently by CLAS [Ava03]. While HERMES observed a negative $A_{LU}^{\sin\phi} = \langle \sin\phi \rangle = -0.23 \pm 0.04 \pm 0.03$ (at $\langle x \rangle = 0.11$, $\langle Q^2 \rangle = 2.6\,\mathrm{GeV}^2/c^2$), the CLAS collaboration reports a positive average asymmetry of $0.038 \pm 0.005 \pm 0.003$ (at $1\,\mathrm{GeV}^2/c^2 < Q^2 < 3\,\mathrm{GeV}^2/c^2$, $0.5 < z < 0.8$).

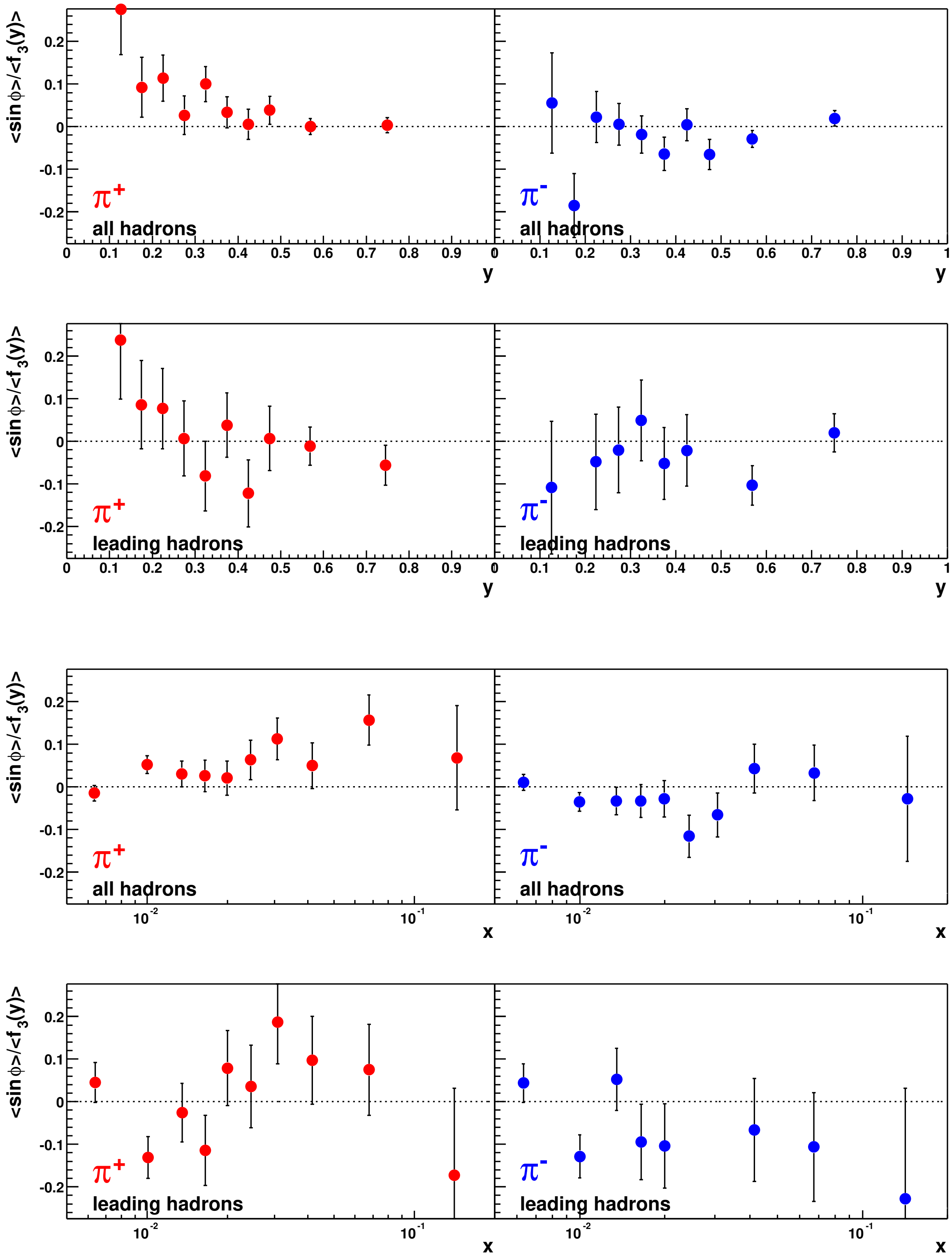

Figure A.3: Dependence of $\langle \sin\phi \rangle / \langle f_3(y) \rangle$ on y (top) and x (bottom).

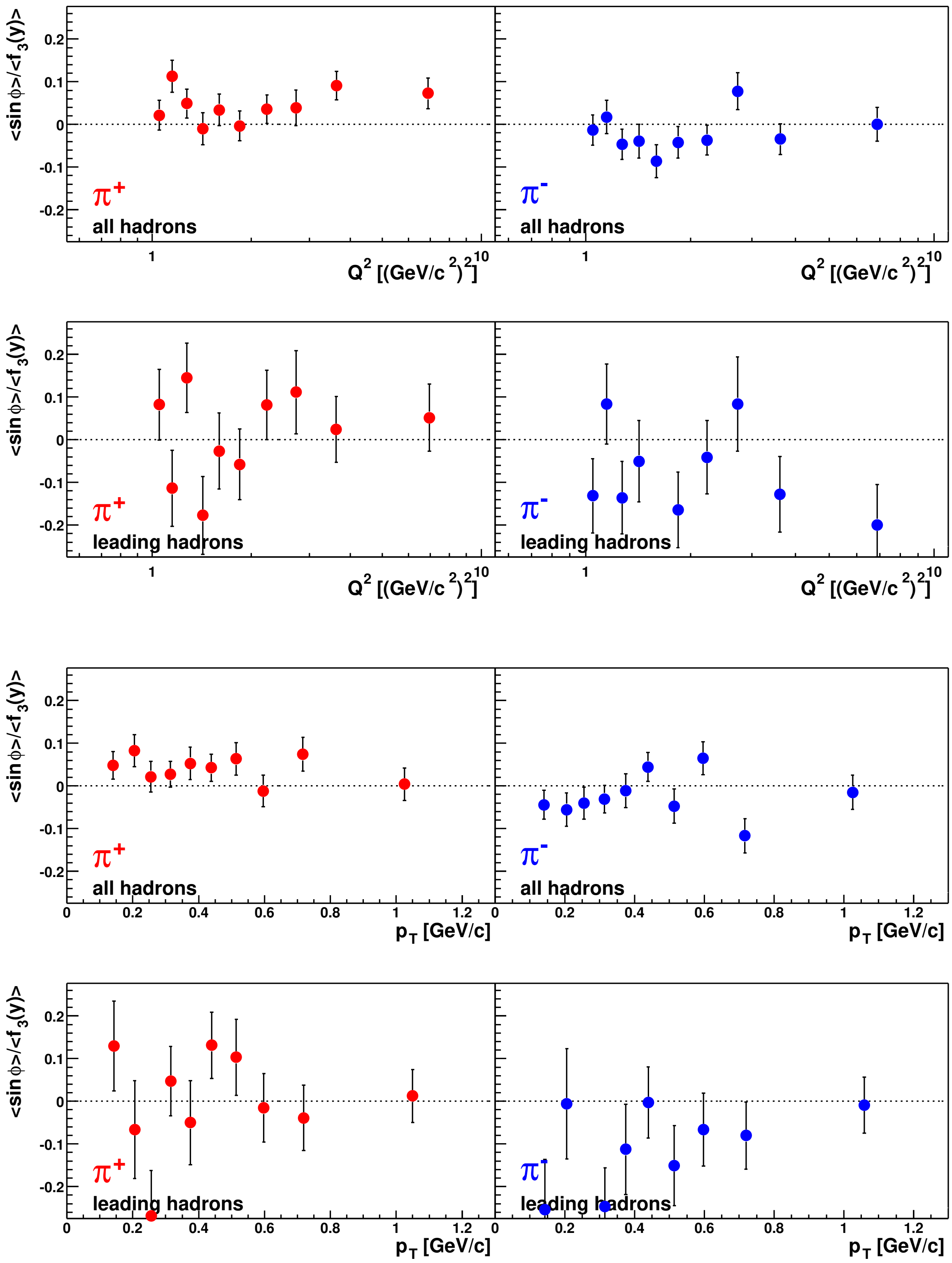

Figure A.4: Dependence of $\langle \sin \phi \rangle / \langle f_3(y) \rangle$ on Q^2 (top) and p_T (bottom).

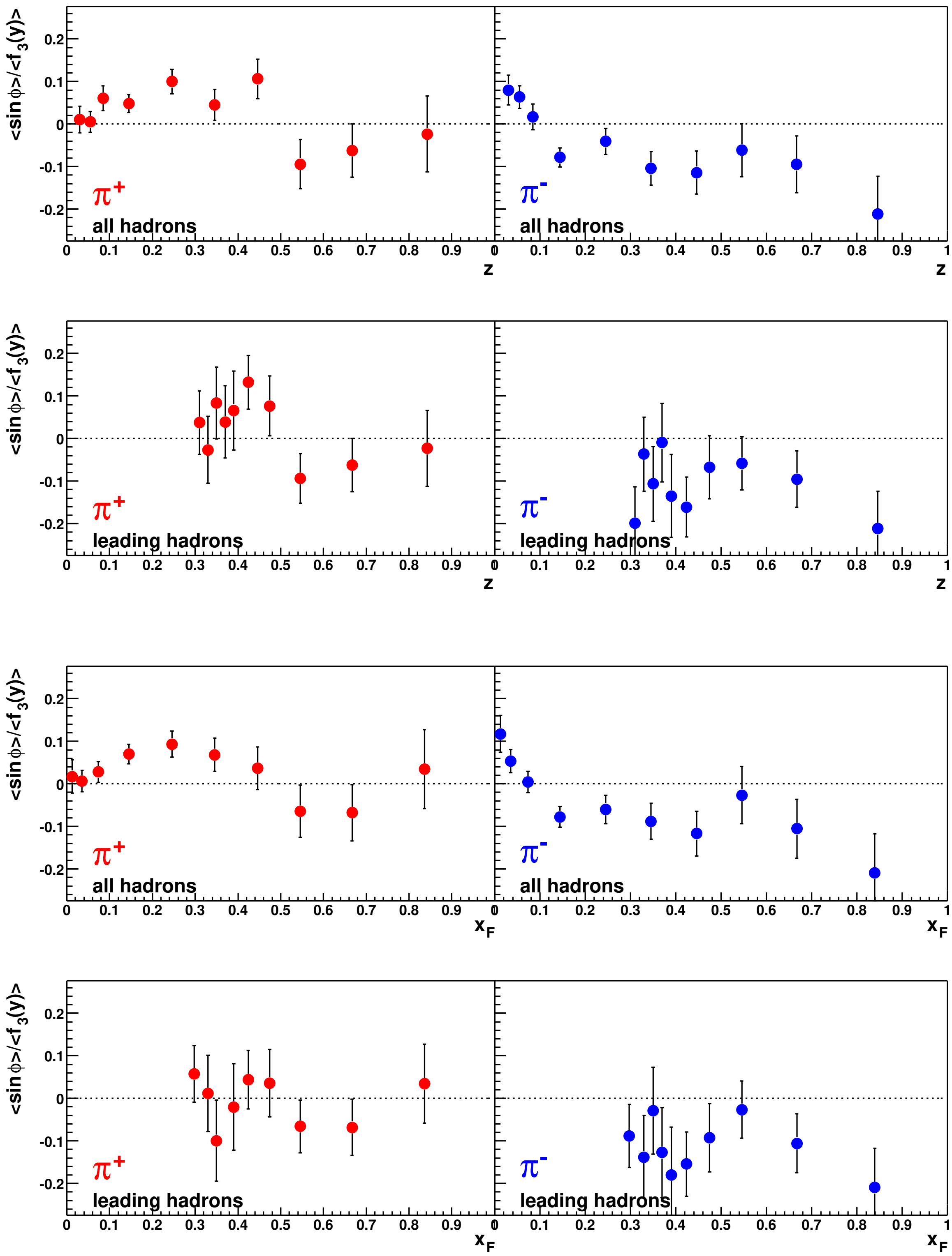

Figure A.5: Dependence of $\langle \sin\phi \rangle / \langle f_3(y) \rangle$ on z (top) and x_F (bottom).

Appendix B

Tables

B.1 Cut Statistics

B.1.1 Real Data

cut	**total #events**	**relative**	**relative**
no cut	140,785,481		
SIDIS candidate	48,193,312	34.2%	34.2%
$Q^2 > 1$	2,738,133	1.9%	5.7%
data quality	2,672,484	1.9%	97.6%
target	1,642,682	1.2%	61.5%
hodoscopes	1,489,639	1.0%	90.7%
beam $\chi_r^2 < 10$	1,478,159	1.0%	99.2%
μ' $\chi_r^2 < 10$	1,470,342	1.0%	99.5%
μ' $X/X_0 > 30$	1,421,344	1.0%	96.7%
μ' calorimeter	1,414,149	1.0%	99.5%
$W > 4\,\mathrm{GeV}/c^2$	1,368,481	1.0%	96.8%
$0.1 < y < 0.9$	1,256,406	0.9%	91.8%
cuts on hadron candidates	896,944	0.6%	71.4%
cuts on leading hadrons	296,775	0.2%	23.6%

Table B.1: Losses in event numbers due to the cuts listed in Section 4.1 (see Pg. 25 ff.). The relative values in the third column give the remaining fraction with respect to the number of events before all cuts. The values in the fourth column give the fractions with respect to the number of events without the cut in question. The reference "no cut" means the sample of mDST-events, i.e. events with at least on vertex. For the cuts referred to as "cuts on hadron candidates" and "cuts on leading hadrons" see Tables B.1.1 and B.1.1, respectively.

cut	**total #hadrons**	**relative**	**relative**
after all event cuts	3,226,951		
fringe field	2,988,909	92.6%	92.6%
$\chi_r^2 < 10$	2,864,627	88.8%	95.8%
$X/X_0 < 10$	2,771,863	85.9%	96.8%
calorimeter	1,580,908	49.0%	57.0%
$p_T > 0.1\,\mathrm{GeV}/c$	1,386,890	43.0%	87.7%
$z < 1.0$	1,386,007	43.0%	99.9%
$x_F > 0$	1,379,347	42.7%	99.5%

Table B.2: Losses in hadron numbers due to the cuts on the hadron candidates (c.f. Sec. 4.1, Pg. 28 ff.). The relative values in the third column give the remaining fraction with respect to the number of hadrons before all cuts on the hadron candidates. The values in the fourth column give the fractions with respect to the number of hadrons without the cut in question. The 3,226,951 hadrons "after all event cuts" stem from the 1,256,406 events after the cut on y in Tab. B.1.1, which means that the hadron multiplicity per event *without* the cuts on the hadron candidates is 2.6. After the cuts on the hadron candidates 1,379,347 hadrons remain in 896,944 events (see Tab. B.1.1), corresponding to a multiplicity of 1.5.

cut	**total #hadrons**	**relative**	**relative**
hadron candidates	1,580,908		
maximum z in event	964,582	61.0%	61.0%
"Dietrich" criterion	826,205	52.3%	85.7%
$p_T > 0.1\,\mathrm{GeV}/c$	775,787	49.1%	93.9%
$z > 0.25$	373,985	23.7%	48.2%
$z > 0.3$	296,775	18.8%	38.3%
$z > 0.4$	182,885	11.6%	23.6%
$z > 0.5$	111,609	7.1%	14.4%

Table B.3: Losses in leading hadron candidates due to the leading hadron selection algorithm described in Sec. 4.2.3 (Pg. 35 ff.). The relative values in the third column give the remaining fraction with respect to the number of hadrons before all cuts on the hadron candidates. The values in the fourth column give the fractions with respect to the number of hadrons without the cut in question. The term "Dietrich" criterion summarises the criteria for leading hadron candidates which are described in the said section. The cut on x_F has no impact on the hadron numbers since it is applied after the cut on z. The standard cut on z used in this analysis is $z > 0.3$, thus the 296,775 leading hadrons which pass this cut correspond to the same number of events which pass the "cuts on leading hadrons" mentioned in Tab. B.1.1.

B.1.2 Monte Carlo

cut	gen. tot.	relative	relative	rec. tot.	relative	relative
no cut	2,212,636			2,212,636		
SIDIS candidate	2,212,636	100.0%	100.0%	1,694,211	76.6%	76.7%
$Q^2 > 1$	967,523	43.7%	43.7%	716,006	32.4%	42.3%
target	682,932	30.9%	70.6%	496,770	22.5%	69.4%
beam $\chi^2_r < 10$				495,911	22.4%	99.8%
hodoscopes				464,085	21.0%	93.6%
μ' $\chi^2_r < 10$				463,964	21.0%	100.0%
μ' $X/X_0 > 30$				449,331	20.3%	97.0%
μ' calorimeter				446,797	20.2%	96.3%
$W > 4\,\mathrm{GeV}/c^2$	659,052	29.8%	96.5%	441,846	20.0%	98.9%
$0.1 < y < 0.9$	585,408	26.5%	88.8%	413,130	18.7%	93.5%
hadron cuts	560,031	25.3%	95.7%	270,145	12.2%	65.4%
$z > 0.3$	290,048	13.1%	51.8%	111,324	5.0%	41.2%

Table B.4: Losses in Monte Carlo event numbers due to the cuts listed in section 4.1 (see Pg. 25 ff.). The relative values in the third column give the remaining fraction with respect to the number of events before all cuts. The values in the fourth column give the fractions with respect to the number of events without the cut in question. The reference "no cut" means the sample of mDST-events, i.e. events with at least on vertex.

cut	tot. gen.	relative	relative	tot. rec.	relative	relative
after all event cuts	3,264,352			1,110,412		
hadron PID	3,203,150	98.1%	98.1%	748,542	67.4%	67.4%
fringe field				713,307	64.2%	95.3%
$\chi^2_r < 10$				712,216	64.1%	99.8%
$X/X_0 < 10$				696,039	62.7%	97.7%
calorimeter				410,634	37.0%	59.0%
$p_T > 0.1\,\mathrm{GeV}/c$	2,936,147	89.9%	91.7%	388,751	35.0%	94.7%
$z < 1.0$	2,936,001	89.9%	100.0%	388,574	35.0%	100.0%
$x_F > 0$	1,584,885	48.6%	49.5%	386,919	34.8%	99.6%
$z > 0.3$	314,530	9.6%	19.8%	114,819	10.3%	37.4%

Table B.5: Losses in hadron numbers in the Monte Carlo sample due to the cuts on the hadron candidates (see 4.1, Pg. 28 ff.). The relative values in the third column give the remaining fraction with respect to the number of hadrons before all cuts on the hadron candidates. The values in the fourth column give the fractions with respect to the number of hadrons without the cut in question. The number of hadrons after all event cuts refers to charged particles only.

	before all cuts	after all cuts
π^+	27.8 %	34.2 %
π^-	26.1 %	31.5 %
K^+	4.4 %	5.5 %
K^-	3.6 %	4.5 %
p	4.0 %	4.5 %
$\bar{p}$	1.5 %	2.1 %
e^+	7.6 %	3.9 %
e^-	7.8 %	4.1 %
μ^+	0.2 %	0.0 %
μ^-	0.2 %	0.0 %
ghost tracks	16.7 %	9.5 %

Table B.6: Particle type composition of the reconstructed Monte Carlo sample of hadron candidates before (left) and after (right) all cuts (*all hadron* sample), excluding the cut on the hadron PID.

	no cut on z	$z > 0.3$
π^+	41.5 %	40.3 %
π^-	38.3 %	35.1 %
K^+	6.7 %	9.0 %
K^-	5.5 %	6.9 %
p	5.4 %	5.3 %
$\bar{p}$	2.6 %	3.4 %

Table B.7: Particle type composition of the reconstructed Monte Carlo sample after all cuts. Left: as used for the correction of the *all hadron* sample (i.e. including the tracks with low z). Right: as used for the correction of the leading hadron sample (i.e. with a cut on $z > 0.3$).

B.2 Binning

B.2.1 Inclusive Variables

bin#		$\langle y \rangle$ all had. $\pi^+ \mid \pi^-$	$\langle y \rangle$ leading $\pi^+ \mid \pi^-$	# all had.	# leading
1	$0.10 \leq y < 0.15$	0.127 | 0.127	0.125 | 0.125	133,856	63,032
2	$0.15 \leq y < 0.20$	0.175 | 0.175	0.174 | 0.174	161,770	54,833
3	$0.20 \leq y < 0.25$	0.225 | 0.225	0.224 | 0.224	160,934	41,802
4	$0.25 \leq y < 0.30$	0.274 | 0.275	0.274 | 0.274	146,711	30,131
5	$0.30 \leq y < 0.35$	0.324 | 0.325	0.324 | 0.324	129,922	22,605
6	$0.35 \leq y < 0.40$	0.374 | 0.374	0.374 | 0.374	114,152	17,374
7	$0.40 \leq y < 0.45$	0.424 | 0.424	0.424 | 0.424	99,418	13,858
8	$0.45 \leq y < 0.50$	0.475 | 0.474	0.474 | 0.474	84,284	11,145
9	$0.50 \leq y < 0.65$	0.569 | 0.569	0.568 | 0.569	189,673	23,528
10	$0.65 \leq y < 0.90$	0.749 | 0.750	0.745 | 0.750	58,627	18,467
bin#		$\langle Q^2 \rangle$ **all had.** $\pi^+ \mid \pi^-$	$\langle Q^2 \rangle$ **leading** $\pi^+ \mid \pi^-$	**# all had.**	**# leading**
1	$1.00 \leq Q^2 < 1.10$	1.049 | 1.048	1.049 | 1.049	138,081	30,947
2	$1.10 \leq Q^2 < 1.20$	1.149 | 1.149	1.149 | 1.149	117,897	26,065
3	$1.20 \leq Q^2 < 1.35$	1.272 | 1.272	1.272 | 1.273	151,639	33,656
4	$1.35 \leq Q^2 < 1.50$	1.423 | 1.423	1.424 | 1.423	124,715	27,645
5	$1.50 \leq Q^2 < 1.70$	1.596 | 1.596	1.595 | 1.597	133,953	29,288
6	$1.70 \leq Q^2 < 2.00$	1.842 | 1.843	1.842 | 1.842	151,498	32,459
7	$2.00 \leq Q^2 < 2.50$	2.229 | 2.230	2.229 | 2.231	167,365	35,823
8	$2.50 \leq Q^2 < 3.00$	2.731 | 2.732	2.732 | 2.729	106,378	22,476
9	$3.00 \leq Q^2 < 4.50$	3.628 | 3.626	3.621 | 3.613	153,333	30,914
10	$4.50 \leq Q^2$	6.885 | 6.866	6.946 | 6.867	134,488	27,502
bin#		$\langle x \rangle$ **all had.** $\pi^+ \mid \pi^-$	$\langle x \rangle$ **leading** $\pi^+ \mid \pi^-$	**# all had.**	**# leading**
1	$0.000 \leq x < 0.008$	0.0063 | 0.0063	0.0064 | 0.0063	158,299	19,705
2	$0.008 \leq x < 0.012$	0.0100 | 0.0100	0.0101 | 0.0100	208,411	28,517
3	$0.012 \leq x < 0.015$	0.0135 | 0.0135	0.0135 | 0.0135	145,016	22,536
4	$0.015 \leq x < 0.018$	0.0165 | 0.0165	0.0165 | 0.0165	125,917	22,026
5	$0.018 \leq x < 0.022$	0.0199 | 0.0199	0.0200 | 0.0200	137,437	28,199
6	$0.022 \leq x < 0.027$	0.0244 | 0.0244	0.0245 | 0.0244	132,628	31,889
7	$0.027 \leq x < 0.035$	0.0307 | 0.0307	0.0308 | 0.0308	149,363	42,541
8	$0.035 \leq x < 0.050$	0.0414 | 0.0414	0.0415 | 0.0415	147,274	46,073
9	$0.050 \leq x < 0.100$	0.0676 | 0.0675	0.0677 | 0.0674	135,441	43,264
10	$0.100 \leq x < 1.000$	0.1445 | 0.1441	0.1413 | 0.1417	39,561	12,025

Table B.8: Ranges of the ten bins in y, Q^2 and x. The third and fourth columns contain the corresponding average value for all and leading hadrons, while the last two columns contain the number of entries in each bin for these two samples. The width of each bin is adapted to the requirements of comparable statistic in each bin on the one hand and reasonable spread over the full kinematic range on the other hand.

B.2.2 Semi-inclusive Variables

bin#		$\langle p_T \rangle$ **all had.** π^+ | π^-	$\langle p_T \rangle$ **leading** π^+ | π^-	**# hadrons**	**# leading**
1	$0.10 \le p_T < 0.16$	0.140 | 0.140	0.143 | 0.143	237,025	22,733
2	$0.16 \le p_T < 0.22$	0.205 | 0.205	0.206 | 0.206	150,691	19,035
3	$0.22 \le p_T < 0.28$	0.255 | 0.255	0.256 | 0.255	146,352	21,578
4	$0.28 \le p_T < 0.34$	0.314 | 0.314	0.315 | 0.315	188,618	32,792
5	$0.34 \le p_T < 0.40$	0.374 | 0.374	0.375 | 0.375	116,242	23,668
6	$0.40 \le p_T < 0.47$	0.438 | 0.438	0.439 | 0.439	152,860	35,173
7	$0.47 \le p_T < 0.55$	0.514 | 0.513	0.514 | 0.514	101,723	27,258
8	$0.55 \le p_T < 0.65$	0.596 | 0.597	0.598 | 0.598	103,616	32,653
9	$0.65 \le p_T < 0.80$	0.717 | 0.717	0.719 | 0.719	91,177	34,986
10	$0.80 \le p_T$	1.025 | 1.025	1.050 | 1.059	91,043	46,899

Table B.9: Ranges of the ten bins in p_T. The third and fourth columns contain the corresponding average value for all and leading hadrons, while the last two columns contain the number of entries in each bin for these two samples.

bin#		$\langle z \rangle$ **all had.** $\pi^+ \mid \pi^-$	**# hadrons**
1	$0.00 \leq z < 0.04$	$0.030 \mid 0.030$	95,800
2	$0.04 \leq z < 0.07$	$0.055 \mid 0.055$	194,149
3	$0.07 \leq z < 0.10$	$0.085 \mid 0.085$	176,008
4	$0.10 \leq z < 0.20$	$0.145 \mid 0.144$	389,986
5	$0.20 \leq z < 0.30$	$0.246 \mid 0.245$	213,782
6	$0.30 \leq z < 0.40$	$0.346 \mid 0.345$	124,026
7	$0.40 \leq z < 0.50$	$0.446 \mid 0.446$	73,884
8	$0.50 \leq z < 0.60$	$0.546 \mid 0.546$	45,754
9	$0.60 \leq z < 0.75$	$0.667 \mid 0.667$	38,533
10	$0.75 \leq z < 1.00$	$0.843 \mid 0.846$	27,425
bin#		$\langle z \rangle$ **leading** $\pi^+ \mid \pi^-$	**# leading**
1	$0.30 \leq z < 0.32$	$0.310 \mid 0.310$	26,765
2	$0.32 \leq z < 0.34$	$0.330 \mid 0.330$	24,860
3	$0.34 \leq z < 0.36$	$0.350 \mid 0.350$	22,577
4	$0.36 \leq z < 0.38$	$0.370 \mid 0.370$	20,746
5	$0.38 \leq z < 0.40$	$0.390 \mid 0.390$	18,942
6	$0.40 \leq z < 0.45$	$0.424 \mid 0.424$	39,889
7	$0.45 \leq z < 0.50$	$0.474 \mid 0.474$	31,387
8	$0.50 \leq z < 0.60$	$0.546 \mid 0.546$	45,659
9	$0.60 \leq z < 0.75$	$0.667 \mid 0.667$	38,528
10	$0.75 \leq z < 1.00$	$0.843 \mid 0.846$	27,422

Table B.10: Ranges of the ten bins in z. The third and fourth columns contain the corresponding average value for all and leading hadrons, while the last two columns contain the number of entries in each bin for these two samples. Different bins have to be chosen for the samples of all and leading hadrons because of the cut on $z > 0.3$ on the leading hadron sample.

bin#		$\langle x_F \rangle$ **all had.** $\pi^+ \mid \pi^-$	**# hadrons**
1	$0.00 \leq x_F < 0.02$	$0.013 \mid 0.013$	63,421
2	$0.02 \leq x_F < 0.05$	$0.036 \mid 0.036$	195,615
3	$0.05 \leq x_F < 0.10$	$0.074 \mid 0.074$	292,860
4	$0.10 \leq x_F < 0.20$	$0.145 \mid 0.144$	351,375
5	$0.20 \leq x_F < 0.30$	$0.246 \mid 0.245$	193,181
6	$0.30 \leq x_F < 0.40$	$0.346 \mid 0.345$	113,162
7	$0.40 \leq x_F < 0.50$	$0.446 \mid 0.446$	68,228
8	$0.50 \leq x_F < 0.60$	$0.546 \mid 0.546$	41,916
9	$0.75 \leq x_F < 0.75$	$0.667 \mid 0.667$	35,651
10	$0.75 \leq x_F$	$0.836 \mid 0.836$	23,938
bin#		$\langle x_F \rangle$ **leading** $\pi^+ \mid \pi^-$	**# leading**
1	$x_F < 0.32$	$0.298 \mid 0.298$	48,642
2	$0.32 \leq x_F < 0.34$	$0.330 \mid 0.330$	22,969
3	$0.34 \leq x_F < 0.36$	$0.350 \mid 0.350$	21,163
4	$0.36 \leq x_F < 0.38$	$0.370 \mid 0.370$	19,182
5	$0.38 \leq x_F < 0.40$	$0.390 \mid 0.390$	17,194
6	$0.40 \leq x_F < 0.45$	$0.424 \mid 0.424$	36,991
7	$0.45 \leq x_F < 0.50$	$0.474 \mid 0.474$	29,166
8	$0.50 \leq x_F < 0.60$	$0.546 \mid 0.546$	41,883
9	$0.75 \leq x_F < 0.75$	$0.667 \mid 0.667$	35,647
10	$0.75 \leq x_F$	$0.836 \mid 0.840$	23,938

Table B.11: Ranges of the ten bins in x_F. The third and fourth columns contain the corresponding average value for all and leading hadrons, while the last two columns contain the number of entries in each bin for these two samples. Because of the correlation of z and x_F the cut on z which is applied on the leading hadron sample has almost the same effect as a corresponding cut on $x_F > 0.3$. Hence different binnings are necessary for the two hadron samples.

B.3 Kinematic variables

	π^+ / up	π^+ / down	π^- / up	π^- / down
$\langle y \rangle$	0.38	0.36	0.39	0.37
$\langle Q^2 \rangle$	2.33	2.45	2.32	2.40
$\langle x \rangle$	0.026	0.030	0.026	0.029
$\langle p_T \rangle$	0.37	0.41	0.37	0.40
$\langle p_T^2 \rangle$	0.21	0.23	0.20	0.22
$\langle z \rangle$	0.22	0.21	0.20	0.20
$\langle x_F \rangle$	0.20	0.19	0.19	0.18

Table B.12: Average values of the kinematic variables y, Q^2, x, z, x_F, p_T and p_T^2 for the complete sample of all hadrons. Note that $\langle Q^2 \rangle$ is given in GeV$^2/c^2$ and $\langle p_T \rangle$ ($\langle p_T^2 \rangle$) in GeV/c (GeV$^2/c^2$).

	π^+ / up	π^+ / down	π^- / up	π^- / down
$\langle y \rangle$	0.30	0.28	0.31	0.30
$\langle Q^2 \rangle$	2.31	2.45	2.23	2.32
$\langle x \rangle$	0.033	0.038	0.031	0.035
$\langle p_T \rangle$	0.52	0.53	0.51	0.53
$\langle p_T^2 \rangle$	0.36	0.37	0.35	0.37
$\langle z \rangle$	0.49	0.49	0.49	0.49
$\langle x_F \rangle$	0.47	0.47	0.47	0.47

Table B.13: Average values of the kinematic variables y, Q^2, x, z, x_F, p_T and p_T^2 for the complete leading hadrons sample. Note that Q^2 is given in (GeV/c)^2 and p_T ($\langle p_T^2 \rangle$) in GeV/c (GeV$^2/c^2$).

B.4 Results

sample	**bin#**	$\langle\cos\phi\rangle/\langle f_1(y)\rangle$	$\langle f_1(y)\rangle$	$\langle\cos\phi\rangle/\langle f_1(y)\rangle$	$\langle f_1(y)\rangle$
all had.	1	-0.039 ± 0.007	0.993	$+0.002 \pm 0.008$	0.993
	2	-0.038 ± 0.006	0.986	$+0.012 \pm 0.006$	0.986
	3	-0.043 ± 0.006	0.976	-0.011 ± 0.006	0.976
	4	-0.040 ± 0.006	0.963	-0.022 ± 0.006	0.963
	5	-0.063 ± 0.006	0.945	-0.043 ± 0.007	0.945
	6	-0.048 ± 0.007	0.924	-0.056 ± 0.007	0.924
	7	-0.034 ± 0.007	0.898	-0.068 ± 0.008	0.898
	8	-0.026 ± 0.008	0.866	-0.076 ± 0.009	0.866
	9	-0.028 ± 0.006	0.790	-0.043 ± 0.006	0.790
	10	-0.009 ± 0.008	0.583	-0.023 ± 0.008	0.581
leading	1	-0.108 ± 0.008	0.993	-0.093 ± 0.010	0.993
	2	-0.139 ± 0.009	0.986	-0.121 ± 0.010	0.986
	3	-0.160 ± 0.009	0.976	-0.162 ± 0.011	0.976
	4	-0.161 ± 0.011	0.963	-0.170 ± 0.013	0.963
	5	-0.156 ± 0.013	0.946	-0.190 ± 0.015	0.946
	6	-0.137 ± 0.015	0.924	-0.193 ± 0.017	0.924
	7	-0.109 ± 0.016	0.898	-0.163 ± 0.019	0.898
	8	-0.083 ± 0.019	0.867	-0.096 ± 0.020	0.866
	9	-0.070 ± 0.014	0.791	-0.080 ± 0.015	0.790
	10	-0.107 ± 0.021	0.589	-0.042 ± 0.021	0.582

sample	**bin#**	$\langle\cos 2\phi\rangle/\langle f_2(y)\rangle$	$\langle f_2(y)\rangle$	$\langle\cos 2\phi\rangle/\langle f_2(y)\rangle$	$\langle f_2(y)\rangle$
all had.	1	$+0.026 \pm 0.012$	0.495	$+0.096 \pm 0.014$	0.495
	2	$+0.009 \pm 0.011$	0.491	$+0.059 \pm 0.012$	0.491
	3	$+0.008 \pm 0.011$	0.484	-0.001 ± 0.012	0.484
	4	$+0.015 \pm 0.012$	0.475	$+0.027 \pm 0.013$	0.475
	5	$+0.007 \pm 0.012$	0.464	-0.008 ± 0.013	0.464
	6	$+0.035 \pm 0.013$	0.449	$+0.026 \pm 0.014$	0.449
	7	$+0.005 \pm 0.015$	0.432	$+0.016 \pm 0.016$	0.432
	8	$+0.059 \pm 0.017$	0.412	$+0.039 \pm 0.018$	0.412
	9	$+0.061 \pm 0.012$	0.362	$+0.021 \pm 0.013$	0.362
	10	$+0.064 \pm 0.020$	0.233	$+0.038 \pm 0.021$	0.232
leading	1	-0.031 ± 0.015	0.495	$+0.038 \pm 0.018$	0.495
	2	-0.006 ± 0.016	0.491	$+0.014 \pm 0.019$	0.491
	3	-0.043 ± 0.018	0.484	-0.094 ± 0.021	0.484
	4	-0.022 ± 0.022	0.475	$+0.008 \pm 0.025$	0.475
	5	$+0.025 \pm 0.025$	0.464	$+0.016 \pm 0.028$	0.464
	6	$+0.113 \pm 0.028$	0.450	$+0.109 \pm 0.031$	0.450
	7	$+0.027 \pm 0.034$	0.432	$+0.067 \pm 0.037$	0.432
	8	$+0.048 \pm 0.037$	0.412	$+0.011 \pm 0.042$	0.412
	9	$+0.060 \pm 0.029$	0.363	$+0.078 \pm 0.032$	0.362
	10	-0.021 ± 0.053	0.237	$+0.104 \pm 0.051$	0.233

Table B.14: y-dependence of $\langle\cos\phi\rangle/\langle f_1(y)\rangle$ and $\langle\cos 2\phi\rangle/\langle f_2(y)\rangle$. Left: results for π^+; Right: results for π^-. The fourth and sixth columns give the values of $\langle f_1(y)\rangle$ and $\langle f_2(y)\rangle$ which are used to correct the raw moments for the y-dependence as it was predicted by Cahn. Only statistical errors are given.

sample	bin#	$\langle\cos\phi\rangle/\langle f_1(y)\rangle$	$\langle f_1(y)\rangle$	$\langle\cos\phi\rangle/\langle f_1(y)\rangle$	$\langle f_1(y)\rangle$
all had.	1	-0.032 ± 0.006	0.886	-0.023 ± 0.006	0.882
	2	-0.044 ± 0.007	0.886	-0.027 ± 0.007	0.883
	3	-0.023 ± 0.006	0.886	-0.034 ± 0.006	0.883
	4	-0.020 ± 0.007	0.888	-0.035 ± 0.007	0.884
	5	-0.025 ± 0.006	0.889	-0.020 ± 0.007	0.885
	6	-0.030 ± 0.006	0.886	-0.021 ± 0.007	0.882
	7	-0.027 ± 0.006	0.885	-0.015 ± 0.006	0.880
	8	-0.031 ± 0.008	0.883	-0.018 ± 0.008	0.878
	9	-0.039 ± 0.006	0.881	-0.035 ± 0.007	0.876
	10	-0.053 ± 0.006	0.908	-0.024 ± 0.007	0.905
leading	1	-0.125 ± 0.011	0.931	-0.135 ± 0.012	0.922
	2	-0.146 ± 0.012	0.932	-0.139 ± 0.014	0.924
	3	-0.133 ± 0.011	0.931	-0.143 ± 0.012	0.922
	4	-0.103 ± 0.012	0.934	-0.112 ± 0.013	0.926
	5	-0.110 ± 0.012	0.933	-0.133 ± 0.013	0.925
	6	-0.107 ± 0.011	0.932	-0.125 ± 0.012	0.922
	7	-0.110 ± 0.010	0.930	-0.110 ± 0.012	0.923
	8	-0.112 ± 0.014	0.927	-0.080 ± 0.016	0.921
	9	-0.108 ± 0.012	0.924	-0.116 ± 0.014	0.918
	10	-0.137 ± 0.011	0.936	-0.115 ± 0.014	0.934

sample	bin#	$\langle\cos 2\phi\rangle/\langle f_2(y)\rangle$	$\langle f_2(y)\rangle$	$\langle\cos 2\phi\rangle/\langle f_2(y)\rangle$	$\langle f_2(y)\rangle$
all had.	1	$+0.001 \pm 0.012$	0.425	$+0.033 \pm 0.013$	0.423
	2	$+0.020 \pm 0.013$	0.426	$+0.010 \pm 0.014$	0.424
	3	$+0.019 \pm 0.012$	0.426	$+0.013 \pm 0.013$	0.424
	4	$+0.040 \pm 0.014$	0.427	$+0.023 \pm 0.014$	0.425
	5	-0.001 ± 0.013	0.428	$+0.030 \pm 0.014$	0.425
	6	$+0.040 \pm 0.013$	0.426	$+0.009 \pm 0.014$	0.423
	7	$+0.005 \pm 0.012$	0.425	$+0.025 \pm 0.013$	0.422
	8	$+0.017 \pm 0.015$	0.424	$+0.043 \pm 0.017$	0.420
	9	$+0.058 \pm 0.013$	0.423	$+0.024 \pm 0.014$	0.419
	10	$+0.030 \pm 0.012$	0.440	$+0.035 \pm 0.014$	0.438
leading	1	$+0.006 \pm 0.022$	0.455	-0.008 ± 0.024	0.449
	2	$+0.009 \pm 0.024$	0.455	$+0.029 \pm 0.026$	0.450
	3	-0.005 ± 0.021	0.455	-0.019 ± 0.023	0.449
	4	-0.001 ± 0.024	0.457	$+0.024 \pm 0.026$	0.451
	5	-0.021 ± 0.023	0.456	$+0.028 \pm 0.025$	0.451
	6	-0.012 ± 0.022	0.455	-0.010 ± 0.025	0.449
	7	-0.068 ± 0.021	0.454	-0.011 ± 0.024	0.450
	8	-0.011 ± 0.027	0.452	-0.009 ± 0.031	0.449
	9	$+0.022 \pm 0.023$	0.450	$+0.011 \pm 0.026$	0.446
	10	-0.003 ± 0.021	0.458	$+0.033 \pm 0.027$	0.457

Table B.15: Q^2-dependence of $\langle\cos\phi\rangle/\langle f_1(y)\rangle$ and $\langle\cos 2\phi\rangle/\langle f_2(y)\rangle$. Left: results for π^+; Right: results for π^-. The fourth and sixth columns give the values of $\langle f_1(y)\rangle$ and $\langle f_2(y)\rangle$ which are used to correct the raw moments for the y-dependence as it was predicted by Cahn. Only statistical errors are given.

sample	**bin#**	$\langle\cos\phi\rangle/\langle f_1(y)\rangle$	$\langle f_1(y)\rangle$	$\langle\cos\phi\rangle/\langle f_1(y)\rangle$	$\langle f_1(y)\rangle$
all had.	1	-0.012 ± 0.007	0.671	-0.022 ± 0.007	0.669
	2	-0.028 ± 0.005	0.822	-0.047 ± 0.005	0.821
	3	-0.037 ± 0.006	0.875	-0.040 ± 0.007	0.875
	4	-0.044 ± 0.007	0.903	-0.045 ± 0.007	0.901
	5	-0.038 ± 0.006	0.923	-0.038 ± 0.007	0.921
	6	-0.041 ± 0.006	0.938	-0.041 ± 0.007	0.937
	7	-0.039 ± 0.006	0.951	-0.031 ± 0.007	0.951
	8	-0.038 ± 0.006	0.959	-0.022 ± 0.007	0.959
	9	-0.036 ± 0.006	0.967	$+0.019 \pm 0.007$	0.966
	10	-0.041 ± 0.012	0.977	$+0.071 \pm 0.014$	0.977
leading	1	-0.088 ± 0.017	0.672	-0.049 ± 0.018	0.669
	2	-0.085 ± 0.012	0.822	-0.109 ± 0.013	0.820
	3	-0.110 ± 0.013	0.877	-0.160 ± 0.015	0.876
	4	-0.154 ± 0.013	0.904	-0.174 ± 0.015	0.902
	5	-0.159 ± 0.012	0.923	-0.162 ± 0.013	0.921
	6	-0.143 ± 0.011	0.939	-0.161 ± 0.013	0.939
	7	-0.131 ± 0.010	0.953	-0.148 ± 0.011	0.952
	8	-0.132 ± 0.010	0.962	-0.129 ± 0.011	0.961
	9	-0.108 ± 0.010	0.969	-0.072 ± 0.012	0.968
	10	-0.073 ± 0.017	0.978	-0.010 ± 0.024	0.977

sample	**bin#**	$\langle\cos 2\phi\rangle/\langle f_2(y)\rangle$	$\langle f_2(y)\rangle$	$\langle\cos 2\phi\rangle/\langle f_2(y)\rangle$	$\langle f_2(y)\rangle$
all had.	1	$+0.045 \pm 0.016$	0.289	$+0.032 \pm 0.017$	0.288
	2	$+0.030 \pm 0.011$	0.384	$+0.010 \pm 0.012$	0.383
	3	$+0.026 \pm 0.013$	0.420	$+0.009 \pm 0.014$	0.419
	4	$+0.023 \pm 0.013$	0.437	$+0.036 \pm 0.014$	0.436
	5	$+0.022 \pm 0.013$	0.449	$+0.022 \pm 0.014$	0.448
	6	$+0.024 \pm 0.013$	0.460	$+0.039 \pm 0.014$	0.460
	7	$+0.042 \pm 0.012$	0.469	$+0.052 \pm 0.013$	0.469
	8	$+0.033 \pm 0.012$	0.475	$+0.035 \pm 0.013$	0.474
	9	$+0.026 \pm 0.012$	0.479	$+0.045 \pm 0.014$	0.479
	10	-0.010 ± 0.022	0.485	$+0.029 \pm 0.027$	0.485
leading	1	$+0.036 \pm 0.040$	0.298	$+0.052 \pm 0.040$	0.290
	2	$+0.028 \pm 0.025$	0.395	$+0.060 \pm 0.027$	0.389
	3	$+0.046 \pm 0.026$	0.432	$+0.068 \pm 0.029$	0.429
	4	$+0.002 \pm 0.026$	0.450	$+0.062 \pm 0.029$	0.449
	5	-0.008 ± 0.023	0.463	-0.007 ± 0.026	0.463
	6	-0.006 ± 0.022	0.473	$+0.000 \pm 0.024$	0.474
	7	$+0.010 \pm 0.019$	0.481	-0.042 ± 0.021	0.482
	8	-0.025 ± 0.018	0.484	-0.027 ± 0.021	0.484
	9	-0.040 ± 0.018	0.486	$+0.020 \pm 0.022$	0.486
	10	-0.065 ± 0.033	0.488	$+0.010 \pm 0.042$	0.488

Table B.16: x-dependence of $\langle\cos\phi\rangle/\langle f_1(y)\rangle$ and $\langle\cos 2\phi\rangle/\langle f_2(y)\rangle$. Left: results for π^+; Right: results for π^-. The fourth and sixth columns give the values of $\langle f_1(y)\rangle$ and $\langle f_2(y)\rangle$ which are used to correct the raw moments for the y-dependence as it was predicted by Cahn. Only statistical errors are given.

sample	bin#	$\langle\cos\phi\rangle/\langle f_1(y)\rangle$	$\langle f_1(y)\rangle$	$\langle\cos\phi\rangle/\langle f_1(y)\rangle$	$\langle f_1(y)\rangle$
all had.	1	$+0.023 \pm 0.006$	0.893	$+0.058 \pm 0.006$	0.893
	2	$+0.016 \pm 0.006$	0.893	$+0.037 \pm 0.007$	0.891
	3	-0.002 ± 0.006	0.892	$+0.012 \pm 0.007$	0.889
	4	-0.022 ± 0.005	0.890	-0.007 ± 0.006	0.887
	5	-0.042 ± 0.007	0.889	-0.036 ± 0.007	0.884
	6	-0.049 ± 0.006	0.887	-0.049 ± 0.006	0.880
	7	-0.049 ± 0.007	0.885	-0.056 ± 0.008	0.878
	8	-0.064 ± 0.007	0.885	-0.070 ± 0.007	0.876
	9	-0.063 ± 0.007	0.881	-0.079 ± 0.008	0.871
	10	-0.096 ± 0.008	0.867	-0.098 ± 0.008	0.859
leading	1	-0.070 ± 0.013	0.941	-0.059 ± 0.014	0.934
	2	-0.062 ± 0.014	0.942	-0.097 ± 0.016	0.935
	3	-0.124 ± 0.013	0.939	-0.105 ± 0.014	0.932
	4	-0.134 ± 0.011	0.936	-0.111 ± 0.012	0.930
	5	-0.147 ± 0.013	0.936	-0.122 ± 0.014	0.927
	6	-0.139 ± 0.011	0.935	-0.152 ± 0.012	0.926
	7	-0.132 ± 0.012	0.933	-0.142 ± 0.014	0.925
	8	-0.136 ± 0.011	0.931	-0.134 ± 0.012	0.923
	9	-0.107 ± 0.010	0.928	-0.143 ± 0.012	0.918
	10	-0.126 ± 0.010	0.910	-0.141 ± 0.011	0.905

sample	bin#	$\langle\cos 2\phi\rangle/\langle f_2(y)\rangle$	$\langle f_2(y)\rangle$	$\langle\cos 2\phi\rangle/\langle f_2(y)\rangle$	$\langle f_2(y)\rangle$
all had.	1	$+0.030 \pm 0.011$	0.430	$+0.039 \pm 0.012$	0.430
	2	$+0.017 \pm 0.013$	0.430	$+0.026 \pm 0.014$	0.429
	3	$+0.016 \pm 0.013$	0.429	$+0.025 \pm 0.014$	0.428
	4	$+0.034 \pm 0.011$	0.428	$+0.022 \pm 0.012$	0.426
	5	$+0.023 \pm 0.013$	0.427	$+0.033 \pm 0.015$	0.424
	6	$+0.034 \pm 0.012$	0.427	$+0.023 \pm 0.013$	0.422
	7	$+0.007 \pm 0.014$	0.425	$+0.010 \pm 0.015$	0.421
	8	$+0.031 \pm 0.014$	0.425	$+0.034 \pm 0.015$	0.419
	9	-0.001 ± 0.015	0.423	$+0.023 \pm 0.016$	0.416
	10	$+0.021 \pm 0.016$	0.414	$+0.020 \pm 0.017$	0.408
leading	1	$+0.005 \pm 0.025$	0.461	$+0.019 \pm 0.028$	0.457
	2	$+0.031 \pm 0.028$	0.462	-0.012 ± 0.031	0.458
	3	-0.001 ± 0.026	0.460	-0.045 ± 0.029	0.456
	4	$+0.051 \pm 0.021$	0.458	$+0.059 \pm 0.024$	0.454
	5	$+0.015 \pm 0.025$	0.458	-0.000 ± 0.028	0.452
	6	$+0.026 \pm 0.020$	0.458	$+0.012 \pm 0.023$	0.452
	7	-0.055 ± 0.023	0.456	$+0.004 \pm 0.027$	0.451
	8	-0.065 ± 0.021	0.455	-0.023 ± 0.024	0.450
	9	-0.052 ± 0.021	0.453	$+0.013 \pm 0.023$	0.447
	10	-0.036 ± 0.019	0.441	$+0.005 \pm 0.022$	0.438

Table B.17: p_T-dependence of $\langle\cos\phi\rangle/\langle f_1(y)\rangle$ and $\langle\cos 2\phi\rangle/\langle f_2(y)\rangle$. Left: results for π^+; Right: results for π^-. The fourth and sixth columns give the values of $\langle f_1(y)\rangle$ and $\langle f_2(y)\rangle$ which are used to correct the raw moments for the y-dependence as it was predicted by Cahn. Only statistical errors are given.

sample	bin#	$\langle\cos\phi\rangle/\langle f_1(y)\rangle$	$\langle f_1(y)\rangle$	$\langle\cos\phi\rangle/\langle f_1(y)\rangle$	$\langle f_1(y)\rangle$
all had.	1	-0.002 ± 0.010	0.731	$+0.012 \pm 0.011$	0.730
	2	-0.009 ± 0.006	0.827	$+0.022 \pm 0.006$	0.826
	3	$+0.005 \pm 0.005$	0.876	$+0.020 \pm 0.006$	0.875
	4	-0.012 ± 0.003	0.906	-0.021 ± 0.004	0.907
	5	-0.049 ± 0.004	0.918	-0.053 ± 0.005	0.919
	6	-0.086 ± 0.005	0.924	-0.075 ± 0.006	0.921
	7	-0.104 ± 0.006	0.930	-0.102 ± 0.007	0.923
	8	-0.125 ± 0.008	0.935	-0.138 ± 0.009	0.924
	9	-0.177 ± 0.008	0.939	-0.187 ± 0.010	0.927
	10	-0.144 ± 0.010	0.945	-0.198 ± 0.012	0.935
leading	1	-0.061 ± 0.011	0.923	-0.081 ± 0.012	0.919
	2	-0.083 ± 0.012	0.922	-0.088 ± 0.012	0.920
	3	-0.113 ± 0.012	0.924	-0.061 ± 0.013	0.920
	4	-0.105 ± 0.012	0.924	-0.114 ± 0.014	0.920
	5	-0.107 ± 0.013	0.926	-0.073 ± 0.014	0.922
	6	-0.109 ± 0.009	0.930	-0.098 ± 0.010	0.923
	7	-0.114 ± 0.010	0.931	-0.124 ± 0.011	0.923
	8	-0.126 ± 0.008	0.934	-0.139 ± 0.009	0.924
	9	-0.177 ± 0.008	0.939	-0.187 ± 0.010	0.927
	10	-0.144 ± 0.010	0.945	-0.198 ± 0.012	0.935
sample	**bin#**	$\langle\cos 2\phi\rangle/\langle f_2(y)\rangle$	$\langle f_2(y)\rangle$	$\langle\cos 2\phi\rangle/\langle f_2(y)\rangle$	$\langle f_2(y)\rangle$
all had.	1	$+0.042 \pm 0.022$	0.327	-0.009 ± 0.024	0.326
	2	$+0.008 \pm 0.012$	0.387	-0.010 ± 0.013	0.387
	3	$+0.017 \pm 0.011$	0.419	$+0.022 \pm 0.012$	0.419
	4	$+0.016 \pm 0.007$	0.439	$+0.012 \pm 0.007$	0.439
	5	$+0.001 \pm 0.009$	0.447	-0.009 ± 0.009	0.447
	6	-0.007 ± 0.010	0.450	-0.005 ± 0.011	0.449
	7	$+0.003 \pm 0.013$	0.454	$+0.003 \pm 0.014$	0.450
	8	$+0.022 \pm 0.015$	0.457	$+0.014 \pm 0.017$	0.451
	9	$+0.011 \pm 0.016$	0.460	$+0.058 \pm 0.018$	0.452
	10	-0.120 ± 0.020	0.464	$+0.052 \pm 0.024$	0.457
leading	1	$+0.009 \pm 0.022$	0.450	-0.063 ± 0.024	0.447
	2	$+0.011 \pm 0.024$	0.449	-0.029 ± 0.025	0.448
	3	-0.040 ± 0.024	0.450	$+0.026 \pm 0.026$	0.448
	4	-0.002 ± 0.024	0.451	$+0.005 \pm 0.028$	0.447
	5	-0.056 ± 0.026	0.452	$+0.029 \pm 0.029$	0.449
	6	-0.020 ± 0.017	0.454	-0.049 ± 0.019	0.450
	7	$+0.012 \pm 0.019$	0.455	$+0.032 \pm 0.021$	0.450
	8	$+0.021 \pm 0.015$	0.457	$+0.012 \pm 0.017$	0.449
	9	$+0.011 \pm 0.016$	0.460	$+0.058 \pm 0.018$	0.452
	10	-0.120 ± 0.020	0.464	$+0.051 \pm 0.024$	0.457

Table B.18: z-dependence of $\langle\cos\phi\rangle/\langle f_1(y)\rangle$ and $\langle\cos 2\phi\rangle/\langle f_2(y)\rangle$. Left: results for π^+; Right: results for π^-. The fourth and sixth columns give the values of $\langle f_1(y)\rangle$ and $\langle f_2(y)\rangle$ which are used to correct the raw moments for the y-dependence as it was predicted by Cahn. Only statistical errors are given.

sample	bin#	$\langle\cos\phi\rangle/\langle f_1(y)\rangle$	$\langle f_1(y)\rangle$	$\langle\cos\phi\rangle/\langle f_1(y)\rangle$	$\langle f_1(y)\rangle$
all had.	1	-0.023 ± 0.012	0.711	$+0.009 \pm 0.014$	0.710
	2	-0.012 ± 0.006	0.810	$+0.020 \pm 0.006$	0.808
	3	-0.002 ± 0.004	0.880	$+0.011 \pm 0.005$	0.879
	4	-0.016 ± 0.004	0.912	-0.028 ± 0.004	0.913
	5	-0.058 ± 0.005	0.918	-0.066 ± 0.005	0.919
	6	-0.099 ± 0.006	0.923	-0.087 ± 0.006	0.919
	7	-0.111 ± 0.007	0.929	-0.106 ± 0.008	0.920
	8	-0.130 ± 0.008	0.932	-0.142 ± 0.010	0.921
	9	-0.175 ± 0.009	0.937	-0.199 ± 0.011	0.925
	10	-0.155 ± 0.011	0.942	-0.195 ± 0.013	0.931
leading	1	-0.060 ± 0.009	0.935	-0.071 ± 0.010	0.932
	2	-0.105 ± 0.013	0.922	-0.092 ± 0.014	0.918
	3	-0.136 ± 0.013	0.922	-0.102 ± 0.015	0.919
	4	-0.111 ± 0.014	0.924	-0.082 ± 0.015	0.919
	5	-0.097 ± 0.014	0.926	-0.106 ± 0.016	0.922
	6	-0.126 ± 0.009	0.929	-0.107 ± 0.011	0.920
	7	-0.107 ± 0.010	0.930	-0.120 ± 0.012	0.922
	8	-0.131 ± 0.008	0.932	-0.142 ± 0.010	0.921
	9	-0.175 ± 0.009	0.937	-0.199 ± 0.011	0.925
	10	-0.155 ± 0.011	0.942	-0.195 ± 0.013	0.931

sample	bin#	$\langle\cos 2\phi\rangle/\langle f_2(y)\rangle$	$\langle f_2(y)\rangle$	$\langle\cos 2\phi\rangle/\langle f_2(y)\rangle$	$\langle f_2(y)\rangle$
all had.	1	-0.007 ± 0.028	0.314	$+0.002 \pm 0.030$	0.313
	2	$+0.031 \pm 0.013$	0.377	$+0.005 \pm 0.014$	0.376
	3	$+0.010 \pm 0.009$	0.421	$+0.010 \pm 0.010$	0.421
	4	$+0.021 \pm 0.007$	0.443	$+0.007 \pm 0.008$	0.443
	5	-0.017 ± 0.009	0.446	-0.018 ± 0.010	0.447
	6	-0.009 ± 0.011	0.449	-0.009 ± 0.012	0.447
	7	-0.001 ± 0.013	0.453	$+0.018 \pm 0.015$	0.448
	8	$+0.032 \pm 0.016$	0.456	-0.001 ± 0.019	0.448
	9	$+0.005 \pm 0.017$	0.459	$+0.066 \pm 0.020$	0.451
	10	-0.124 ± 0.022	0.462	$+0.052 \pm 0.026$	0.455
leading	1	$+0.022 \pm 0.018$	0.458	-0.034 ± 0.019	0.456
	2	-0.007 ± 0.026	0.449	$+0.008 \pm 0.028$	0.447
	3	-0.069 ± 0.026	0.449	-0.038 ± 0.029	0.447
	4	-0.021 ± 0.028	0.450	$+0.003 \pm 0.031$	0.447
	5	-0.018 ± 0.028	0.452	-0.000 ± 0.032	0.449
	6	-0.013 ± 0.018	0.453	-0.043 ± 0.022	0.448
	7	-0.015 ± 0.021	0.454	$+0.065 \pm 0.023$	0.449
	8	$+0.032 \pm 0.016$	0.456	-0.001 ± 0.019	0.448
	9	$+0.005 \pm 0.017$	0.459	$+0.066 \pm 0.020$	0.451
	10	-0.124 ± 0.022	0.462	$+0.052 \pm 0.026$	0.455

Table B.19: x_F-dependence of $\langle\cos\phi\rangle/\langle f_1(y)\rangle$ and $\langle\cos 2\phi\rangle/\langle f_2(y)\rangle$. Left: results for π^+; Right: results for π^-. The fourth and sixth columns give the values of $\langle f_1(y)\rangle$ and $\langle f_2(y)\rangle$ which are used to correct the raw moments for the y-dependence as it was predicted by Cahn. Only statistical errors are given.

Bibliography

[Ack99] K. Ackerstaff et al., Phys. Lett. **B464**, 123 (1999).

[Ada93] M. R. Adams et al., Phys. Rev. **D48**, 5057 (1993).

[Ada99] D. Adams et al., Nucl. Instrum. Meth. **A437**, 23 (1999).

[Air01] A. Airapetian et al., Phys. Rev. Lett. **87**, 182001 (2001).

[Ale] V. Alexakhin, *COMGEANT web page*, `http://valexakh.home.cern.ch/valexakh/wwwcomg/`.

[Ale03] V. Alexakhin, *LEPTO data sample*, `/castor/cern.ch/user/v/valexakh/lepto/muplus160/2002/mDST/new*/`, 2003.

[And83] Bo Andersson, G. Gustafson, G. Ingelman, and T. Sjostrand, Phys. Rept. **97**, 31 (1983).

[Arn87] M. Arneodo et al., Z. Phys. **C34**, 277 (1987).

[Aub83] J. J. Aubert et al., Phys. Lett. **B130**, 118 (1983).

[Ava03] H. Avakian et al., hep-ex/0301005.

[Bau96] G. Baum et al., CERN-SPSLC-96-14.

[BDR02] V. Barone, A. Drago, and P. G. Ratcliffe, Phys. Rept. **359**, 1 (2002).

[Ber80] Edmond L. Berger, Phys. Lett. **B89**, 241 (1980).

[Bis04] J. Bisplinghoff et al., *Collins Asymmetries from 2002 COMPASS Transversity Data*, February 2004, COMPASS Note.

[BKK95] J. Binnewies, Bernd A. Kniehl, and G. Kramer, Phys. Rev. **D52**, 4947 (1995).

[BR] R. Brun and F. Rademakers, *ROOT web page*, `http://root.cern.ch`.

[Cah78] R. N. Cahn, Phys. Lett. **B78**, 269 (1978).

[CES92] J. Chay, S. D. Ellis, and W. J. Stirling, Phys. Rev. **D45**, 46 (1992).

[Col93] J. C. Collins, Nucl. Phys. **B396**, 161 (1993).

[CSS85] J. C. Collins, D. E. Soper, and G. Sterman, Nucl. Phys. **B261**, 104 (1985).

[Dob94] N. Doble, L. Gatignon, G. von Holtey, and F. Novoskoltsev, Nucl. Instrum. Meth. **A343**, 351 (1994).

[Efr03] A. V. Efremov, *Spin Azimuthal Asymmetries in SIDIS*, DIS Petersburg, April 2003.

[EGS03] A. V. Efremov, K. Goeke, and P. Schweitzer, Eur. Phys. J. **C32**, 337 (2003).

[Fis02] H. Fischer et al., IEEE Trans. Nucl. Sci. **49**, 443 (2002).

[Ger] S. Gerassimov, *PHAST web page*, `http://ges.home.cern.ch/ges/phast/`.

[Ger04] S. Gerassimov, *PHAST.6.009*, `/afs/cern.ch/user/g/ges/www/phast/releases/Phast.tar.gz.6.009`, January 2004.

[GGO04] L. Gamberg, G. R. Goldstein, and K. A. Oganessyan, AIP Conf. Proc. **698**, 617 (2004).

[Gob] B. Gobbo, *CORAL web page*, `http://coral.web.cern.ch/coral/`.

[Gof03] J.-M. Le Goff, *COMPASS Analysis Meeting*, `/afs/cern.ch/user/h/horsti/public/analysis-meetings/analysis_meeting-28-08-03/jean-marc_28-08-03.pdf`, August 2003.

[GP78] H. Georgi and H. D. Politzer, Phys. Rev. Lett. **40**, 3 (1978).

[GP04] J.-M. Le Goff and J. Pretz, *Statistical errors and correlations for semi-inclusive asymmetries*, March 2004, COMPASS Note 2004-4.

[Gri87] D. J. Griffiths, *Introduction to Elementary Particles*, Wiley, 1987, New York, USA.

[Grü02] A. Grünemaier, *Eine universelle Ausleseschnittstelle für das COMPASS-Experiment*, Ph.D. thesis, Univ. Freiburg, October 2002.

[Hag02] K. Hagiwara et al., Phys. Rev. **D66**, 010001 (2002).

[HM55] R. Hofstadter and R. W. McAllister, Phys. Rev. **98**, 217 (1955).

[Hod02] M. Frhr. von Hodenberg, *A First Reconstruction of COMPASS Data*, diploma thesis, Univ. Freiburg, June 2002.

[Hof57] R. Hofstadter, Ann. Rev. Nucl. Sc. **7**, 231ff. (1957).

[IER97] G. Ingelman, A. Edin, and J. Rathsman, Comput. Phys. Commun. **101**, 108 (1997).

[JM90] R. L. Jaffe and A. Manohar, Nucl. Phys. **B337**, 509 (1990).

[KK82] A. König and P. Kroll, Z. Phys. **C16**, 89 (1982).

[Kor03a] A. Korzenev, *COMPASS Analysis Meeting*, `/afs/cern.ch/user/h/horsti/public/analysis-meetings/analysis_meeting-25-09-03/alexandre_25-09-03.pdf`, September 2003.

[Kor03b] A. Korzenev, *Quality checks*, `/afs/cern.ch/user/k/korzenev/public/badspill/`, 2003.

[Kot95] A. Kotzinian, Nucl. Phys. **B441**, 234 (1995).

[Kot03] A. Kotzinian, *COMPASS Analysis Meeting*, `/afs/cern.ch/user/h/horsti/public/analysis-meetings/analysis_meeting-30-06-03/aram_30-06-03.ps`, June 2003.

[Leb02] M. Leberig, *Das COMPASS-Triggersystem zur Messung des Gluonbeitrags* ΔG *zum Protonspin*, Ph.D. thesis, Univ. Mainz, Novenber 2002.

[log02] *COMPASS Run Logbook*, 2002.

[Man92] A. V. Manohar, hep-ph/9204208.

[MT96] P. J. Mulders and R. D. Tangerman, Nucl. Phys. **B461**, 197 (1996).

[Oga03] K. A. Oganessyan, L. S. Asilyan, M. Anselmino, and E. De Sanctis, Phys. Lett. **B564**, 60 (2003).

[Pre97] J. Pretz, *Messung der polarisierten Quarkverteilungen in semi-inklusiver Myon-Nukleon-Streuung*, Ph.D. thesis, Univ. Mainz, December 1997.

[Rit02] K. Rith, Prog. Part. Nucl. Phys. **49**, 245 (2002).

[Sch02] T. Schmidt, *A Common Readout Driver for the COMPASS Experiment*, Ph.D. thesis, Univ. Freiburg, May 2002.

[Sjo03] T. Sjostrand, L. Lonnblad, S. Mrenna, and P. Skands, hep-ph/0308153.

[Vet98] M. C. Vetterli, hep-ph/9812420.

Acknowledgements

This diploma thesis would not have been possible without the support and advice of many people. I would like to thank

- Prof. Kay Königsmann for giving me the opportunity to join the Freiburg group and to become part of the COMPASS collaboration.
- Horst Fischer and Fritz-Herbert Heinsius for a lot of fruitful discussions and many helpful and inspiring comments and suggestions.
- Jürgen Franz for the careful reading of the manuscript and many helpful comments.
- Christian Schill who more than once let me benefit from his experience with azimuthal asymmetries.
- Eric Weise for investing a lot of time and nerves in extended discussions and even more, for his friendship.
- Sonja Hedicke for patiently introducing me to the secrets of PHAST and ROOT, for lots of fruitful discussions on asymmetry calculation and data selection as well as for her constant helpfulness and friendliness.
- Martin Frhr. von Hodenberg for the very careful reading of this thesis, for the solutions to some of the major and minor problems with the analysis as well as for the encouragement in times when the things went not so well.
- all the members of the Freiburg group for the friendly and helpful atmosphere.
- the COMPASS collaboration for their support and constant interest in my work, especially Vadim Alexakhin, Sergei Gerassimov, Alexey Guskov, Alex Korzenev, Aram Kotzinian, Jörg Pretz and Richard Webb.
- Gerrit Handrich, Jakob Metzger and all those who invested their time in reading the manuscript for all the helpful comments and English lessons.
- Sebastian Schlicht, best physics teacher ever, without whom I would perhaps not have managed the first steps into physics.
- my family and friends for constantly supporting me and taking care of me.

Deutschsprachige Zusammenfassung

Das Ziel des Myon-Programms des COMPASS Experiments am CERN ist es, mit Hilfe von polarisierter Myon-Nukleon-Streuung die Spin-Struktur des Nukleons zu untersuchen. Zu diesem Zweck sind in der Strahlzeit 2002 Daten genommen worden, die bereits erste DIS-Analysen erlauben. Der Beitrag, den die vorliegende Arbeit zur Analyse dieser Daten leistet, besteht in der Untersuchung eines unpolarisierten Effekts, der in der semi-inklusiven tief inelastischen Streuung beobachtet werden kann: der entsprechende Wirkungsquerschnitt zeigt eine Modulation in der Verteilung des Azimutwinkels der produzierten Hadronen um die Richtung des virtuellen Photons, gemessen bezüglich der Myon-Streuebene. Dieses Verhalten hat drei wesentliche Ursachen:

- Der Cahn-Effekt, bei dem es sich um einen reinen QED-Effekt niedrigster Ordnung handelt. Ursache für die Asymmetrie in der Winkelverteilung des gestreuten Quarks ist dessen Impulskomponente transversal zur Bewegungsrichtung des Photon-Nukleon-Systems.
- QCD-Beiträge, die durch den Transversalimpuls zustande kommen, den das Quark durch den Rückstoß bei der Abstrahlung eines Gluons aufnimmt. Die Gluonabstrahlung ist nicht isotrop, daher resultiert eine Asymmetrie in der Verteilung der gestreuten Quarks.
- Abstrahlung von Photonen im Endzustand, die einen Untergrundprozess zu den beiden eigentlich interessierenden Prozessen darstellt.

Diese Effekte führen zu nichtverschwindenden $\cos\phi$- und $\cos 2\phi$-Momenten im unpolarisierten Wirkungsquerschnitt, welche im Zuge dieser Arbeit bestimmt wurden. Durch den polarisierten Strahl, mit dem bei COMPASS gemessen wird, tritt darüber hinaus ein $\sin\phi$-Moment im Wirkungsquerschnitt auf, welches ebenfalls gemessen wurde. Um die Abhängigkeit der beobachteten Modulation von der Kinematik des Streuereignisses zu untersuchen, wurden die Momente als Funktionen der inklusiven kinematischen Variablen y, x and Q^2, bzw. der Hadronvariablen z, x_F and p_T berechnet. Da der Cahn-Effekt das Verhalten desjenigen Hadrons festlegt, das aus dem getroffenen Quark entsteht, wurden für die Analyse die sogenannten "leading hadrons" ausgewählt, welche mit hoher Wahrscheinlichkeit das getroffene Quark enthalten. Die QCD-Effekte beeinflussen dagegen alle Hadronen aus der Stromfragmentation. Daher wurde die Analyse zusätzlich ohne leading hadron-Selektion durchgeführt.

Die größte Herausforderung bei der Analyse des Cahn-Effekts besteht in der Behandlung zusätzlicher Modulationen in der Verteilung des Azimutwinkels, die durch die geometrische Akzeptanz des Detektors verursacht werden. Um diese Effekte zu beseitigen, wurde eine Monte Carlo-Korrektur der Daten durchgeführt. Während das $\cos\phi$-Moment der Detektorakzeptanz kleiner als das aus den Daten extrahierte Moment ist, stellte sich heraus, dass das $\cos 2\phi$-Moment der Akzeptanz größer ist als das entsprechende Moment des Ergebnisses. Daher muss die Akzeptanz mit großer Genauigkeit bekannt sein, um verlässliche Ergebnisse zu bekommen. Die Schwierigkeit bei dieser Korrektur liegt darin, dass die momentan zur Verfügung stehenden Monte Carlo-Simulationen die Daten nicht mit ausreichender Genauigkeit beschreiben. Daher wurde ein Hauptaugenmerk darauf gerichtet, die systematischen Fehler abzuschätzen, die Folge dieser Abweichungen sind.

Trotzdem zeigen die Ergebnisse dieser Analyse ermutigende Übereinstimmung mit Messungen von EMC und E665. Daher wurde eine Interpretation der Daten versucht, die auf den Vorhersagen Cahns aufbaut und nur einen Beitrag der niedrigsten Ordnung QED annimmt. Dieses Modell erwies sich als nicht ausreichend, um die beobachtete Abhängigkeit der Momente von den kinematischen Variablen zu erklären. Folglich tragen wahrscheinlich alle drei oben genannten Prozesse signifikant zur Winkelabhängigkeit des Wirkungsquerschnitts bei. Die Größenordnung des Beitrags durch die Abstrahlung von Photonen wurde grob aus einer speziellen Monte Carlo-Simulation abgeschätzt. Es stellte sich heraus, dass dieser Effekt Momente von der Größe der bei der Analyse aller Hadronen bestimmten verursachen kann. Die deutlich größeren Effekte, welche bei der Analyse von leading hadrons allein beobachtet werden, lassen sich jedoch nicht ausschließlich durch diesen Effekt erklären. Genauere Monte Carlo-Untersuchungen dieser Strahlungsprozesse bieten eine Möglickeit, in zukünftigen Analysen die Ergebnisse um diesen Beitrag zu korrigieren.

Der interessanteste Aspekt bei der Analyse der Cahn-Asymmetrien ist der Zugang, den die gemessenen Momente zu den intrinsischen Transversalimpulsen der Quarks im Nukleon bieten. Es wurden verschiedene Ansätze versucht, um den mittleren quadratischen Transversalimpuls $\langle k_T^2 \rangle$ aus den gewonnenen Ergebnissen zu bestimmen. Diesen Ansätzen ist die vereinfachende Annahme gemeinsam, dass die beobachtete Modulation allein durch den Cahn-Effekt verursacht wird. Die Resultate unterscheiden sich voneinander, sind jedoch alle in der erwarteten Größenordnung. Verglichen mit den Werten von $\langle k_T^2 \rangle$, die bei EMC und E665 ermittelt wurden, sind sie jedoch etwa um einen Faktor zwei kleiner. Detailliertere Monte Carlo-Studien, bei denen die Beiträge von QCD und höhere Ordnungen QED berücksichtigt sind, werden notwendig sein, um eine verlässlichere Schätzung von $\langle k_T^2 \rangle$ zu erhalten.

Erklärung

Diese Arbeit ist von mir selbstständig verfasst worden, und ich habe keine anderen als die angegebenen Quellen und Hilfsmittel benutzt.

Inga Ludwig, Juli 2004